Organization of Tropical Convection

Julia Miriam Windmiller

München 2017

Organization of Tropical Convection

Julia Miriam Windmiller

Dissertation
an der Fakulät für Physik
der Ludwig–Maximilians–Universität
München

vorgelegt von
Julia Miriam Windmiller
aus München

München, 27.06.2017

Erstgutachter: Prof. Dr. George Craig
Zweitgutachter: Prof. Dr. Bernhard Mayer
Tag der mündlichen Prüfung: 06.10.2017

Contents

Zusammenfassung

Atmosphärische Feuchtkonvektion hat einen wichtigen Anteil an der Unsicherheit in der Vorhersage der zukünftigen Entwicklung des Klimas. Da Konvektion den Zustand der Atmosphäre beeinflusst aber die einzelnen konvektiven Zellen zu klein sind um von Klimamodellen explizit dargestellt werden zu können, muss der Effekt von Konvektion parametrisiert werden. Konvektionsparametrisierungen vernachlässigen in der Regel jegliche Korrelationen zwischen Wolken, obwohl bekannt ist dass Konvektion die Bildung weiterer Konvektion auslösen oder beeinflussen kann. Wo sich neue Konvektion bildet hängt insbesondere von der voran gegangenen Konvektion ab. Zum einen bilden sich neue Wolken bevorzugt an den Rändern von *Cold Pools*, den von vorheriger Konvektion erzeugten kalten Abwinden, und zum anderen können konvektiv bedingte Feuchtigkeitsstörungen in der freien Troposphäre dazu führen, dass sich Konvektion über viele Generationen hinweg, selbst organisiert, auch bekannt als *Self-Aggregation*. Obwohl sowohl über das Auslösen von Konvektion an den Rändern von Cold Pools, als auch über die Ursache und die Eigenschaften der konvektiv erzeugten Feuchtigkeitsstörungen viel bekannt ist, ist unklar wie diese Wechselwirkungen zur Bildung von großskaligen konvektiven Systemen beitragen und so den von Klimamodellen aufgelösten Zustand der Atmosphäre beeinflussen. In der vorliegenden Arbeit untersuchen wir diesen Zusammenhang mit Hilfe einfacher Modelle. Dazu stellen wir die lokalen Prozesse, insbesondere das Auslösen von Konvektion durch Cold Pools und die Auswirkungen von konvektiv erzeugten Feuchtigkeitsstörungen, vereinfacht dar und vergleichen die sich ergebenden Modelle mit Modellen aus der statistischen Physik.

Wir beginnen mit der Einführung eines Modells welches, auf Perkolation basierend, die beobachteten Größenverteilungen von flachen Kumuluswolken reproduzieren kann. Insbesondere zeigen wir, dass sich durch das Zusammenfügen einzelner Wolkenzellen zu größeren Wolken, Wolkengrößenverteilungen ergeben, die zumindest innerhalb eines limitierten Bereiches, einem Potenzgesetz folgen was qualitative, mit aus Satellitenbildern bestimmten Wolkengrößenverteilungen übereinstimmt. Erweiterung des Perkolationsmodells um die, Cold Pool bedingte, räumliche Anhäufung von Wolken führt zu quantitativer Übereinstimmung.

Im zweiten Modell stellen wir die Ausbreitung konvektiver Aktivität in einem 2D Gittermodell dar, welches auf gerichteter Perkolation basiert. Ausgehend von der Annahme, dass sich konvektive Aktivität durch Cold Pools ausbreitet, erörtern wir ob wiederholtes Auslösen von Konvektion durch vorangegangene Konvektion den beobachteten kontinuierlichen Phasenübergang in Niederschlagsintensität erklären kann. Als ersten Test für diese Hypothese zeigen wir, dass das von uns eingeführte Modell die Ausbreitung von Konvektion in einem Atmosphärenmodell reproduziert und erläutern wie diese Hypothese in einem Atmosphärenmodell weiter untersucht werden kann.

Das dritte Modell beschreibt die räumliche Entwicklung von Self-Aggregation, der großflä-

chigen und auf langen Zeitskalen stattfindenden Organisation von Konvektion. Wir zeigen zunächst, dass unter bestimmten Voraussetzungen, die konvektiv bedingten Feuchtigkeitsstörungen durch einen diffusiven Feuchtigkeitsaustausch dargestellt werden können und argumentieren, dass damit die Bildung zunehmend größerer, feuchter und trockener, Gebiete durch *Coarsening*, und damit als Phasentrennung, beschrieben werden kann. Der Vergleich mit früheren Studien zeigt, dass Coarsening zum einen erklären kann warum Self-Aggregation von der Größe und Form des simulierten Gebiets abhängt und zum anderen, zumindest anfänglich, die beobachtete Ausdehnung der feuchten und trockenen Gebieten korrekt beschreibt.

Dass die in dieser Arbeit verwendeten einfachen Modelle aus der statistischen Physik nicht nur zu einer qualitativen Beschreibung der entstehenden großskaligen Systeme sondern auch zu quantitativen Vorhersagen führen liegt daran, dass die Modelle einige universell gültige Eigenschaften besitzen.

Abstract

Atmospheric moist convection is an important source of uncertainty in current climate models. Compared to the resolved spatial scales, convective updrafts are small scale processes which, however, have an important influence on the atmospheric state. To determine their effect on the resolved scales, clouds are usually approximated as non-interacting despite their ability to trigger or favor new convection in their surrounding. In particular, convectively induced cold pools trigger new updrafts along their boundaries and thus induce correlations between successive generations of clouds, while convectively induced humidity perturbations accumulate over many generations and cause self-aggregation of convection on time scales much longer than the individual cloud life times. While the cold pool triggering and the instability of the atmosphere to humidity perturbations have been studied in detail, there is a lack of understanding of how these interactions affect the large scale properties of a convective field and thus impact the resolved scales. In this thesis we will introduce minimally simple models to represent the effects of cold pool triggering and convectively induced humidity perturbations and relate them to models known from statistical physics to determine how these processes lead to the formation of large scale structures.

We start by introducing a modified percolation model which can reproduce the observed size distributions of shallow cumulus clouds. Analyzing size distributions using satellite data, we argue that it is the merging of smaller subclouds to larger clouds which leads to power law size distributions over a range of scales which increase as the total cloud fraction approaches a critical value. Modifying the standard percolation model to include clustering leads to quantitative agreement.

The second model describes the spreading of convective activity using a 2D lattice model based on directed percolation. Motivated by the cold pool induced spreading of convective activity we argue that the ability of convection to trigger new convection can explain the observed continuous phase transition in precipitation strength. While we find that the model can reproduce the spreading of convection in an atmospheric model simulation, we also propose a more direct test for this hypothesis.

The third model addresses the spatial evolution of self-aggregation, which organizes convection on long space and time scales. We argue that the convectively induced humidity perturbations lead to a diffusive spatial interaction and conclude that the upscale growth of moist and dry regions can be described as a phase-separation process called coarsening. Comparison with previous studies shows that coarsening can explain the frequently noted domain shape and size dependence and, at least initially, the upscale growth of moist and dry regions.

Using models known from statistical physics we find that we are not only able to qualitatively describe the emergence of large scale properties but that, due to universal properties of these models, we are able to make quantitative predictions.

Acknowledgements

First of all, I thank my supervisor George Craig whose constant search for minimally simple ways to represent a system as (maximally) complex as the earth's atmosphere has greatly inspired me and without whose continual help, support and enthusiasm this work would certainly not have been possible. Thank you very much for everything!

Secondly, I thank all my colleagues, for making the last three years so enjoyable. In particular, I thank Fabian Jakub and Leonhard Scheck for answering my numerous questions about radiation parametrization schemes and Stephan Rasp, Lotte Bierdel and Tobias Selz, who have shared an office with me and who have each contributed to this thesis in different ways. Stephan, to whom I am very grateful for his time, interest and helpful comments on this manuscript. Lotte, whose dedication to her work has always inspired me and, last but not least, Tobi for his constant support in form of scientific advice and chocolate.

Finally, I thank my family. My parents, for encouraging and supporting me in doing what I want and who, I know, will be extremely proud if this turns out well. My three siblings - Ute, Tina and Ralf - for taking it in turns to look after me whenever I needed it and of course my husband Johannes, for always believing in me.

1. Introduction

1.1. The role of convection in the climate system

Cumulus clouds are manifestations of moist atmospheric convection: buoyant air rises and cools and, as soon as water condenses, this upward movement of air becomes visible as clouds. The horizontal and vertical extent of these clouds varies significantly. During a hot summers day in Munich, for example, the formation of shallow cumulus clouds, sometimes described as small and fluffy clouds, is often followed by the formation of deep precipitating cumulus clouds which extend high into the sky and frequently bring hail, thunder and lightning as well as heavy rain.

1.1.1. Clouds as tracers of large scale circulations

The appearance of atmospheric moist convection, to which we will refer as convection in the following, is strongly influenced by larger-scale circulations. This is particularly obvious in convection over the tropical oceans where the Hadley Cell is the dominant meridional circulation. As the solar heating of the surface is strongest near the equator, surface temperatures are highest there and decrease to the north and the south. Driven by this surface temperature gradient, the mean circulation of the Hadley Cell is described by ascending air above the highest surface temperatures which, as it cannot ascent farther than the tropopause (~17 km), flows polewards, descends in the subtropics and flows back in the direction of the equator, creating the trade winds.

The Intertropical Convergence Zone (ITCZ), where the equatorward flow from the northern hemisphere meets the equatorward flow from the southern hemisphere, is marked by so called deep convection, strongly precipitating clouds which extend up to the tropopause. Upon reaching the tropopause, the clouds spread horizontally, covering areas large enough to be seen from space, an example of which is shown in Fig. 1.1 where the ITCZ is marked by a band of very bright white clouds just north of the equator. In the regions of the trade winds, the tropical oceans are largely covered by shallow cumulus clouds, visible as much smaller and less brightly colored clouds to the north and south of the ITCZ in Fig. 1.1. Shallow cumulus clouds extend only up to about 2 km and are associated with, if at all, light precipitation.

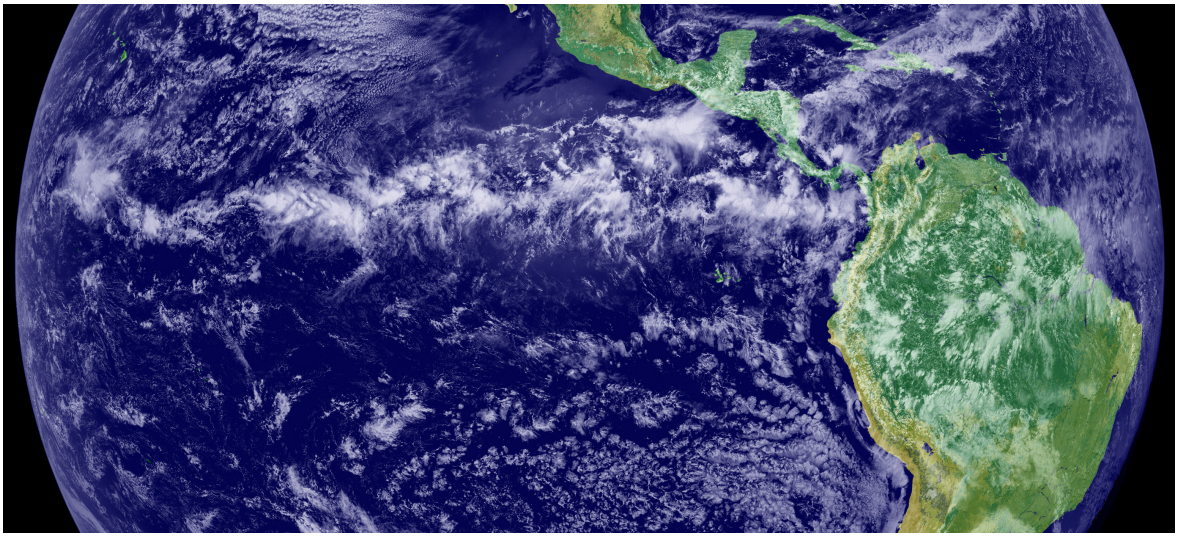

Fig. 1.1.: Satellite image of the eastern pacific part of the ITCZ which appears as a horizontal band of bright white clouds just north of the equator. The image is a combination of cloud data collected by the GOES-11 satellite and color land cover classification data.

1.1.2. Impact of convection on large scale circulations

Clouds, however, are more than mere markers of the large scale circulation as they strongly influence and shape the circulations in which they are embedded (*Bony et al.*, 2015). In particular, the presence of clouds affects the radiative properties of the atmosphere and the upward transport of moisture and heat caused by convection, the dominant source for clouds in the tropics, affects the atmospheric state.

Interaction with radiation

An important mechanism through which clouds feedback on the climate, though not the topic of this dissertation, is radiation. Clouds interact with radiation by reflecting the incoming shortwave radiation and, as cloud tops are generally colder than the surface, by emitting less longwave radiation than the surface.

As the cloud tops of shallow cumulus clouds are not significantly colder than the surface, shallow cumulus clouds primarily affect the reflectance of shortwave radiation, which has been shown to not only depend on cloud coverage fraction but also on the horizontal distribution of clouds (*Cahalan et al.*, 1994). Still, *Muller and Held* (2012) show that as shallow cumulus clouds lead to a vertical shift in the position of longwave cooling, they can induce a low level circulation where cooling at cloud tops induces a horizontal transport of humidity into regions with deep convection.

Deep convective clouds, which often span the depth of the troposphere (the portion of the atmosphere which reaches from the surface to the tropopause), have cloud tops which are significantly colder than the surface. A standard temperature threshold value for identifying deep convection, for example, is $-65\,^{\circ}\mathrm{C}$ (e.g. *Chen et al.*, 1996) which is about $90\,^{\circ}\mathrm{C}$ colder than the tropical mean sea-surface temperature. An increase in deep convective cloud amount has therefore two opposing effects on the temperature: while increased reflection leads to cooling, reduced emission leads to warming. Together, these feedbacks have been shown to have an important, but difficult to quantify, impact on the large scale circulation (e.g. *Slingo and Slingo*, 1988).

Effect of vertical transport

Atmospheric convection is essentially an upward transport process of mass, heat, moisture and momentum.

The upward transport of humidity caused by shallow clouds has been said to partly fuel the Hadley circulation (*Stevens*, 2005). Together with increased surface evaporation, the upward transport of humidity provides the trade winds with moist air which is then transported into the ITCZ where it has been shown to affect the width and intensity of the ITCZ (*Neggers et al.*, 2007).

While we have seen in Fig. 1.1 that the ascending branch of the Hadley cell is marked by deep convection it is important to note that in fact all the upward transport within the ITCZ is confined to the deep convective clouds, which cover only a few percent of the area. This leads to the seemingly paradox statement that most of the air in the ascent region is actually descending (*Stevens*, 2005). It would therefore be an understatement to say that the vertical transport of deep convection influences the Hadley Cell as it really is a central component of it.

1.1.3. Parametrization of the convective impacts

As convective clouds cannot be resolved by current climate models, which can only resolve processes on the order of 100 km, the effect of convection and cloud-radiation feedbacks on the larger scale circulations have to be parametrized.

Convection parameterization

The goal of convection parametrizations is to determine how the unresolved convective transport affects the resolved scale temperature and humidity content.

Convection parametrization is made possible by a scale separation between the large-scale disturbances, which drive convection, and the convective scales. On the one hand, there is a *spatial* scale separation which allows the use of an ensemble approach (*Arakawa and Schubert*, 1974): each column in a climate model is small enough to cover only a fraction of the large scale disturbance but large enough to contain a number of convective clouds. On the other hand, there is also a *temporal* scale separation as convection has been shown to adjust to changes in the forcing much faster than the forcing usually changes (e.g. *Cohen and Craig*, 2004).

Together, these two scale separations allow the assumption that the convective ensemble tends to relax the mean atmospheric state to an equilibrium state on a characteristic time scale. While it has indeed been found that the effect of convection on the temperature can be well approximated by a relaxation towards an empirically determined reference state this is not true for the change in the humidity content (see section 1.4). Most current parametrization schemes, therefore, use a so called mass-flux approximation where the effect of the convective ensemble on the large scale humidity state is determined from the amount of convective updraft and the in-cloud excess of humidity with respect to the mean humidity content.

If, as is commonly done, the convective ensemble is a deterministic function of the resolved conditions it has been shown that this approach is missing important fluctuations resulting from finite domain sizes (*Craig and Cohen*, 2006) and spatial and temporal correlations between convective events (*Majda and Khouider*, 2002). Understanding the physical origin and determining the impact of these correlations forms the main subject of this thesis.

Radiation parametrization

To parametrize the effect of clouds on radiation one starts by approximating the properties of the unresolved clouds from the resolved conditions. First, the fraction of each grid-cell covered by clouds, the so called cloud fraction, is determined from the relative humidity content using an empirical function (e.g. *Quaas*, 2012). Then, the optical properties of the clouds are parameterized. To this end one needs to estimate the properties of liquid water and ice content and the effective size and shape of the respective particles. Finally, as the result of radiative transfer will also strongly depend on the vertical overlap of the subgrid clouds, further assumptions have to be made about the horizontal distribution of the cloud fraction.

Once having estimated the radiative properties of the subgrid scale cloud field, the radiative fluxes are calculated by solving the radiative transfer equation, which accounts for absorption, emission and scattering. As fully solving the radiative transfer equation is computationally not feasible, several approximations have been introduced. The most commonly used approximation is the so called independent column approximation. As the name suggests,

each column in an atmospheric model is assumed independent of all other columns and the radiative fluxes are calculated by solving the radiative transfer equation for each column separately.

Missing representation of convective correlations

Even though it is well known that there exist strong correlations between clouds which impact the atmospheric mean state (as we will discuss in detail in the next section), both of the parametrization schemes introduced above rely on the assumption that individual clouds are independent of each other. This assumption enters into convection parametrizations when assuming that the convective ensemble is solely determined by the large scale conditions and thus independent of the position of other convection and into the radiation scheme via the assumptions about the horizontal distribution.

Cloud feedbacks have been identified as a major source of uncertainty in climate models and determining the importance of convective organization or, likewise, correlations in convective fields has been proposed as a central research question for improving climate prediction (*Bony et al.*, 2015). In this thesis we will investigate the basic mechanisms by which convective clouds organize and explore potential impacts of the arising large scale structures.

1.2. Organization of convection

1.2.1. Definition of organization

Before we can discuss properties and impact of convective organization we first need to define what we mean by organization. Even though organization has advanced to become a research focus in climate science, the term is often used very vaguely. *Mapes and Neale* (2011) for example summarize organization as "non-randomness in meteorological fields in convecting regions ".

In this thesis, we say that convection is organized if it is spatially or temporally correlated to other convection and if it is convection itself which induces these correlations. While convection can also be organized by external mechanisms, a classic example being a low pressure system where convection is spatially correlated with the position of the cold front, we are here interested in organization which arises despite homogeneous boundary conditions and forcing.

To make this description of organization more clear it is best to compare it to the alternative, unorganized case. As we will discuss in more detail later, the average amount of convection is in general determined by the large scale forcing. Assuming that the total amount of

convection is split onto a number of clouds, the unorganized and the organized case according to our description differ in the following way. If convection is unorganized, the clouds should be randomly distributed in space and their properties (like size and lifetime) should be independent draws from the same probability density function. If convection is organized, however, the different clouds depend on each other. In particular, if they are spatially correlated their position is no longer random but might be clustered or regular and if they are temporally correlated they will depend on previous convection.

1.2.2. Different types of organization

In the following we will shortly review three types of organization which have been found in observations and atmospheric model simulations.

Clusters of shallow cumulus clouds

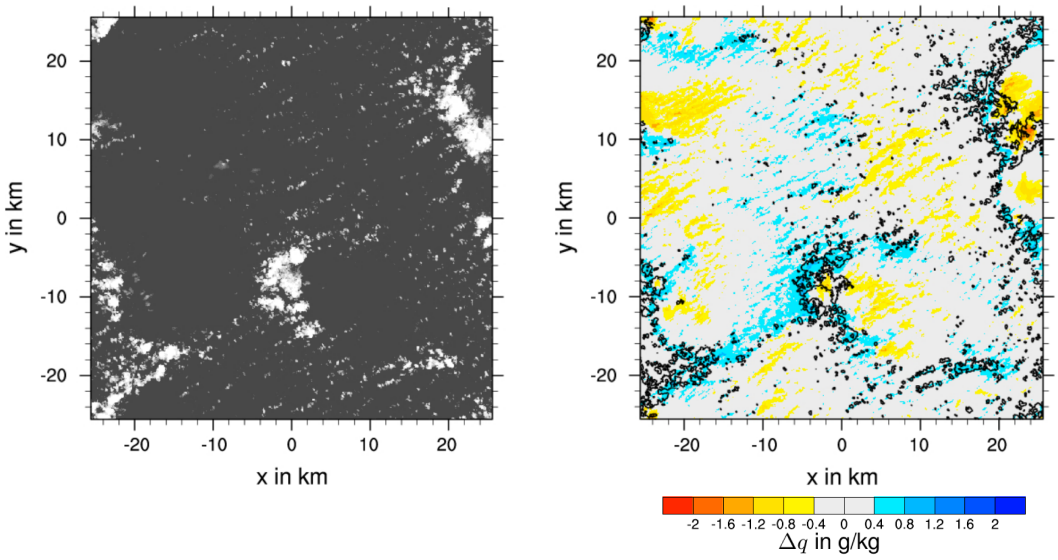

(a) (b)

Fig. 1.2.: Snapshots of a shallow cumulus cloud field in an atmospheric model simulation, showing (a) the synthetic cloud albedo and (b) the moisture deviation in the sub-cloud layer (color) and cloud contours (black lines; $0.001\,\mathrm{g\,m^{-2}}$ and $1.0\,\mathrm{g\,m^{-2}}$ isolines of liquid water path) (*Seifert and Heus*, 2013).

A number of observational studies suggest that shallow cumulus clouds over the ocean tend to cluster. On investigating shallow cumulus clouds over the tropical ocean, *Plank* (1969)

noted that their spatial distribution appeared to be random in the morning but became clustered later in the day. *Sengupta et al.* (1990) found the average nearest neighbor distance to be significantly smaller than expected from a random distribution. Clustering was also found by *Nair et al.* (1998), who note that small clouds cluster around large clouds, and by *Zhao and Di Girolamo* (2007), who show that 75% of the clouds have nearest neighbors within a distance less than ten times their radius.

Clustering of shallow cumulus clouds has also been observed in high resolution numerical simulations. An example, taken from the study conducted by *Seifert and Heus* (2013), is shown in Fig. 1.2. While most of the observational studies described above are based on reflectance fields, as emulated by Fig. 1.2(a), numerical studies allow the examination of additional fields. In particular, *Seifert and Heus* (2013) show that clouds appear on top of positive perturbations in the boundary layer moisture content, see Fig. 1.2(b). These perturbations are caused by previous convection via *cold pools* which we will discuss in more detail later.

Clusters of deep convection

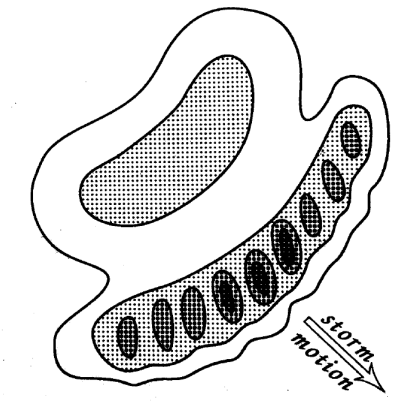

Fig. 1.3.: Schematic radar echo of a squall line. A line of deep convective cells with high radar reflectivity, marked by the dark gray or black cells at the leading edge of the squall line, with trailing stratiform precipitation with weaker radar reflectivity, marked by the light gray region (*Houze Jr*, 1993).

Deep convection frequently organizes into so called mesoscale convective systems (MCSs). MCSs are an important type of weather system as they contribute a large fraction of the rain falling within the tropics and the warmer midlatitudes. Usually defined in terms of large scale precipitation clusters, which extend at least 100 km in one direction, they consist of deep convecting clouds with strong precipitation contained within regions of stratiform high

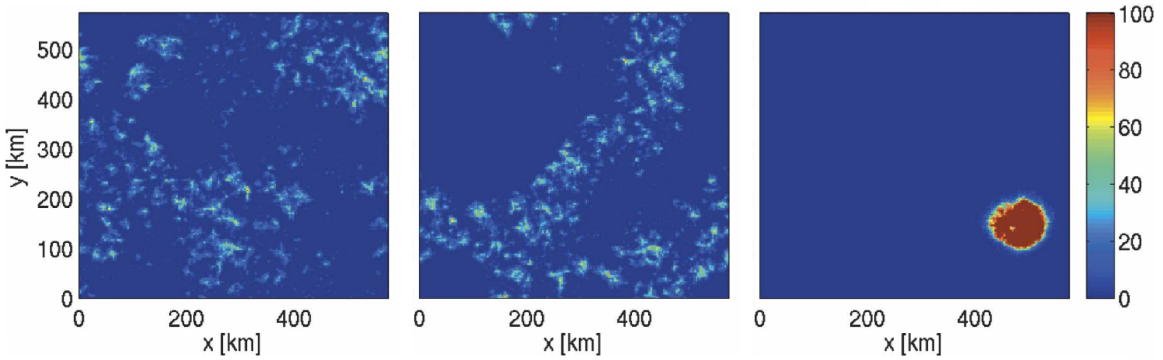

Fig. 1.4.: Daily accumulated precipitation amount $[\mathrm{mm\,d^{-1}}]$ in a cloud resolving model at day 10, day 20 and day 50 (left to right) (*Bretherton et al.*, 2005).

level clouds and weaker precipitation (f.e. *Emanuel et al.*, 1994; *Houze Jr*, 2004). They can live for up to one day and extend up to several hundreds of kilometers.

Depending on the large scale environment, these systems can take different shapes. The most distinct type of a MCS is perhaps the squall line: a propagating line of deep convective cells followed by a region of high clouds, the typical radar echo of which is shown schematically in Fig. 1.3. In addition to the spatial organization along a line, the propagation of squall lines can be described by the successive formation of new cells at the leading front of the MCS. New cells are triggered ahead of the, now heavily precipitating, previous generation of cells schematically shown by the dark gray or black cells in Fig. 1.3, while the older cells merge to form the trailing stratiform rain, the trailing light gray region in Fig. 1.3.

Self-aggregation of convection

A very different type of organization of deep convection is observed in idealized simulations of the tropical atmosphere. Despite homogeneous initial conditions, spontaneous organization of convection develops on timescales of days to weeks, i.e. on significantly longer time scales than the lifetime of MCSs. Starting from convection which initially is approximately randomly distributed, simulations exhibit the formation of convecting and non-convecting regions which grow upscale with time. This phenomena is known as self-aggregation (SA) of convection. An example of this is shown in Fig. 1.4, where convective active regions are indicated by precipitation. This transition from an initially randomly distributed to a spatially organized state of convection was first pointed out by *Held et al.* (1993). Starting from a state of homogeneous humidity and randomly distributed convection, the domain eventually separated into moist and dry regions with convection confined to the moist regions. These regions grow upscale until eventually a steady state is reached with a single moist, convecting region surrounded by a dry subsiding region. Since then, self-aggregation

of convection, following the evolution described above, has been observed in a large number of simulations, though a steady state is not always reached in very large domains or for short simulation times (*Tompkins and Craig*, 1998; *Bretherton et al.*, 2005; *Muller and Held*, 2012; *Kempf*, 2013; *Jeevanjee and Romps*, 2013; *Wing and Emanuel*, 2014; *Muller and Bony*, 2015; *Holloway and Woolnough*, 2016; *Hohenegger and Stevens*, 2016; *Tompkins*, 2001a; *Posselt et al.*, 2012; *Wing and Cronin*, 2016). Because in reality the large scale conditions are neither homogeneous nor constant long enough, the real atmosphere is not expected to show full self-aggregation as observed in the idealized simulations. However, self-aggregation has been proposed to explain the mechanisms leading to the so called Madden-Julian Oscillation of rainfall patterns in the tropical Pacific and to influence the width and intensity of the ITCZ (e.g. *Bony et al.*, 2015).

1.2.3. Impact of organization on size distributions

As we have seen for mesoscale convective systems in the previous section, the successive triggering of new convective cells can lead to the formation of convective structures which have significantly larger spatial dimensions and longer lifetimes than the individual cells of which they are made up. Determining the impact of spatial and temporal correlations on size distributions is one of the key points of this thesis.

If the external forcing determines the amount of convective mass-flux, the question remains how the mass-flux is divided onto the different clouds. How many clouds will there be? What sizes will these clouds have? How long do they live? One way to address these questions is to determine the size and the event size distribution of convective clouds.

Size distributions, which give the average number of clouds of a given size per unit area, can be determined using snapshots of cloud fields. Size distributions of shallow cumulus clouds, for example, have been estimated, initially using photographs from high altitude aircraft (e.g. *Plank*, 1969) and later high resolution satellite images, using either reflectance fields determined from visible or near-infrared channels (e.g. *Wielicki and Welch*, 1986) or brightness temperatures fields from infrared channels (e.g. *Kuo et al.*, 1993), and numerical simulations of cloud fields (e.g. *Neggers et al.*, 2003). Shallow cumulus clouds are then identified using a threshold value for reflectance, brightness temperature and liquid water content, respectively. Size distributions of deep convection have also been analyzed using satellite data (microwave channel) with precipitation as indicator for deep convection (*Peters et al.*, 2009).

Convective *event* size distributions are generally determined as the number of events with a given amount of rain. The total amount of rain which falls during rain events has been obtained from observations by *Peters et al.* (2001) and *Peters et al.* (2010) using vertically pointing Doppler radar and optical rain gauge data respectively.

A particular aspect of the observed size and event size distributions, which has both fascinated and puzzled atmospheric scientists for decades, is that they often exhibit power-law scaling.

Power-laws in shallow cumulus size distributions

Analyses of shallow cumulus clouds in satellite data have shown that the smallest observed cloud sizes are most probable. While early studies have suggested exponential (*Plank*, 1969; *Hozumi et al.*, 1982; *Wielicki and Welch*, 1986) or lognormal (*López*, 1977; *LeMone and Zipser*, 1980) decay of the size distributions, recent studies suggest a power-law decay, although often only over a restricted range of scales, with clouds larger than a scale break less common than expected (*Cahalan and Joseph*, 1989; *Sengupta et al.*, 1990; *Machado and Rossow*, 1993; *Kuo et al.*, 1993; *Nair et al.*, 1998; *Benner and Curry*, 1998; *Zhao and Di Girolamo*, 2007). Similar results have been found in numerical simulations (*Neggers et al.*, 2003; *Dawe and Austin*, 2012; *Heus and Seifert*, 2013). While none of the papers which find power-law scaling in the size distributions suggest a mechanism which leads to this type of scaling, a number of studies note that most of the larger clouds consist of multiple cells (*Hozumi et al.*, 1982; *Wielicki and Welch*, 1986; *Cahalan and Joseph*, 1989; *Kuo et al.*, 1993).

Power-law rain cluster and event size distributions

Power-law like scaling has also been observed for rain events (*Peters et al.*, 2001; *Andrade et al.*, 1998; *Peters et al.*, 2010) and cluster size distributions of deep convection (*Peters et al.*, 2009), though in the latter case only within a limited range of humidity values.

Peters and Neelin (2006), *Peters et al.* (2009) and *Peters et al.* (2010) suggest that the power-law scaling of cluster and event size distributions of deep convection is related to diverging spatial and temporal correlation lengths. In particular, they show that the atmosphere appears to be close to the critical point of a continuous phase transition. The importance of criticality for deep convection was first suggested by *Peters and Neelin* (2006), who used satellite data to determine the relationship between column integrated water vapor and precipitation rate over the major tropical ocean basins. They found that the transition to strong precipitation can be described in terms of a nonequilibrium continuous phase transition. In particular, they found that the precipitation strength increased like a power-law above a critical water vapor content, that the variance in precipitation strength peaked at the critical value and long range (power-law) spatial correlations. This in good agreement with the properties of continuous phase transitions where an order parameter (here precipitation) increases as a power-law when the tuning parameter (water vapor) crosses the critical value, the fluctuations of the

order parameter diverge at the critical value and the spatial decay of correlations between order-parameter fluctuations becomes scale-free.

Peters and Neelin (2006) suggest that the spatial correlations stem from mesoscale convective systems and relate them to critical clusters found in other systems with nonequilibrium continuous phase transition. As size distributions of critical clusters follow power-laws this agrees well with the findings by *Peters et al.* (2009) and *Peters et al.* (2010) who show that, in the vicinity of the critical humidity value, size distributions and rain-fall event size distributions follow power-law scaling.

Power-law size distributions arising at the critical point of continuous phase transitions will play an important role throughout the thesis.

1.2.4. Effect of organization on large scale state

In the previous section we have reviewed three types of observed organization of convection (clustering of shallow cumulus clouds, mesoscale convective systems, self-aggregation) and discussed the impact of organization on size distributions. In the following we will discuss how the respective size distributions affect the large scale state.

The size distributions of shallow cumulus clouds have been found to have an important effect on the earth's radiation budget due to the impact on the albedo, i.e. the fraction of incoming shortwave radiation that is reflected instead of being absorbed (*Cahalan et al.*, 1994). In particular, they showed that it is not enough to consider a field of horizontally homogeneous clouds of a given size but that one needs to account for size distribution and spatial structure to obtain realistic values for the albedo. They even find that, in their setup, the horizontal variance in the cloud water field is more important for the estimated average albedo than the cloud fraction.

While size distributions of shallow cumulus clouds will affect the radiation budget, the observed critical properties of deep convection have important implications for the variability in convection parameterization. As we have seen in section 1.1.3, traditional parameterization schemes of deep convection, based on the assumption that the amount of convection is solely determined by the mean state, cannot represent the observed variability. In particular, close to the critical humidity value, the emergence of large scale clusters and the peak in variability can lead to very different amounts of convection despite the same mean atmospheric state.

Finally, self-aggregation has received much interest in recent years due to its potential negative feedback on climate change by opposing rising sea-surface temperatures. This feedback on rising sea-surface temperatures is caused by three factors. Firstly, self-aggregation has been found to only occur above a critical sea-surface temperature, close to the warmest observed sea-surface temperatures in the current climate (e.g. *Khairoutdinov and Emanuel*,

2010). Secondly, studies of self-aggregation show that with increasing degree of organization the free troposphere becomes increasingly dry (e.g. *Bretherton et al.*, 2005). Thirdly, a decrease in mean humidity results in a significant increase in the outgoing longwave radiation and thus cooling of the sea-surface temperature (e.g. *Hohenegger and Stevens*, 2016). While simulations agree on the increase of radiative cooling with increased self-aggregation, observational studies suggest that the negative feedback due to longwave radiation is largely balanced by a positive feedback due to shortwave radiation, which results from a reduced cloud fraction and thus a reduced albedo with increasing self-aggregation (*Tobin et al.*, 2012, 2013).

1.3. Basic properties of atmospheric convection

The aim of this thesis is to understand the reason and consequences of moist convective organization. To understand how convection can induce spatial and temporal correlations we first need to review some basic properties of convection.

Atmospheric convection indicates the presence of an unstable mass distribution and is associated with the upward transfer of mass by buoyant air. Note that in atmospheric science the term convection usually refers to fluid motion that results from an instability along the direction of the gravitational field thus excluding motion resulting from horizontal density differences or forced convection (*Emanuel et al.*, 1994) .

There are two fundamentally different types of convection: dry and moist convection. The main difference between moist and dry air is that if moist air rises and cools adiabatically it can fall below the critical temperature for condensation and gain extra buoyancy from the release of latent heat. It is this extra supply of buoyancy stored in the water vapor content which makes conditional instability, which we will discuss below, possible. While dry convection is important for example for forming the atmospheric boundary layer, we will focus on moist convection for the remainder of this thesis.

1.3.1. Large scale forcing

The atmosphere is rendered unstable to convection by radiation and surface fluxes. As the atmosphere is nearly transparent to the incoming shortwave radiation, radiation warms the earth's surface more strongly than the atmosphere. By warming the air close to the surface through sensible and latent heat fluxes, this results in an unstable density distribution.

The importance of convection for the atmospheric mean state becomes apparent when regarding the radiation budget. While the surface absorbs more energy than it emits, the atmosphere emits more energy than it absorbs. Unopposed by any other process this would

induce warming of the surface and cooling of the atmosphere until a radiative equilibrium is reached. The most important process preventing a purely radiative equilibrium is moist convection, which transports energy into the free atmosphere by latent heating.

1.3.2. Parcel view of convection

One can determine whether the current state of the atmosphere is stable or unstable to convection by evaluating whether air parcels become buoyant if lifted pseudo adiabatically, i.e. accounting for adiabatic expansion and, in case of moist convection, condensation. Displacing a parcel upward the expansion of air will lead to cooling and, in case the air becomes saturated, condensation will lead to latent heat release partially offsetting the cooling. If, after this hypothetical lifting, the air is colder than the surrounding air, the parcel will be forced back down and can be considered stable. If it is lighter, however, the air parcel is unstable and will keep rising.

There are two types of instability in the atmosphere: a parcel can be unstable to infinitely small lifting or it can be unstable only if being lifted a finite distance. The latter type of instability, often called conditional instability, is only possible because air can become saturated by lifting and the subsequent latent heat release can allow a saturated parcel to remain buoyant where an unsaturated parcel would be stable.

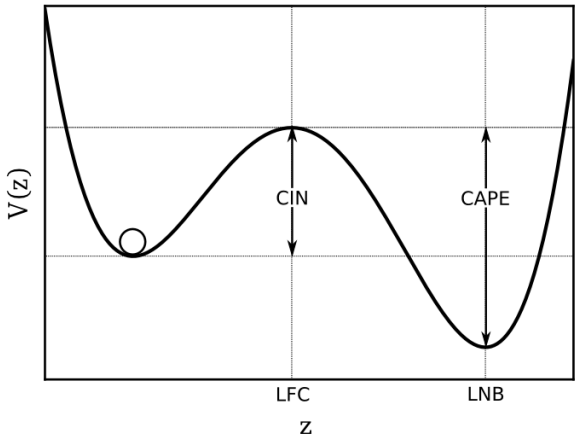

Fig. 1.5.: Schematic representation of conditional instability. An air parcel in the lower minimum needs to be lifted to its level of free convection (LFC) before it can release its buoyant instability and ascent to its level of neutral buoyancy (LNB). The energy necessary to lift the air parcel to its LFC is given by the convective inhibition (CIN) while the amount of energy the air parcel can release is called the convective available potential energy (CAPE).

Conditional instability is the most common form of instability in the atmosphere. One can think of a conditionally unstable parcel as a particle moving in a potential with two minima as shown schematically in Fig. 1.5. As the particle is stable to infinitely small perturbations it is trapped in one of the two minima, typically the one which is energetically less favorable. Lifting the particle to height z it first becomes unstable at the level of free convection (LFC) from which it rises and remains unstable until reaching the level of neutral buoyancy (LNB) and where, due to friction, it eventually comes to rest. The energy necessary to lift the parcel to its LFC is called convective inhibition (CIN) and the energy which is released by the parcel on its way from the LFC to the LNB is called convective available potential energy (CAPE).

The level of neutral buoyancy determines the maximum height convection can reach and is usually just above a layer of sudden increase in atmospheric stability. For example the maximum height convection can reach anywhere on the planet is limited by the tropopause, above which the ozone layer heats the air by increased absorption of the incoming sunlight.

1.3.3. Life cycle of a convective cloud

In the following we will shortly describe the typical life cycle of a single convective cloud. Besides the properties arising from the parcel view discussed above, clouds are strongly affected by turbulent mixing and microphysical processes like the formation of rain, snow and ice.

Byers and Braham (1949) describe the life cycle of a single deep convective cell in three stages: cumulus, mature and dissipating, shown schematically in Fig.1.6. In summarizing the properties of the three stages below, we will also discuss how shallow convection differs from this view.

The cumulus stage is characterized by updrafts throughout the cloud and convergence in the surface wind field. As conditional instability is released, intense updrafts transport heat, moisture and also momentum from the surface into the free troposphere. The updrafts are turbulent, with typical wind speeds of five to ten meters per second, which induces strong mixing with the environmental air at the cloud top and boundary. This mixing, also called entraining, of comparatively drier and colder air reduces the buoyancy. As the air rises and cools, the continued formation of liquid cloud droplets and, below $0\,^{\circ}\mathrm{C}$, ice crystals leads to a continuous release of latent heat. Note that as supercooled droplets can exist up to temperatures as low as $-40\,^{\circ}\mathrm{C}$, there are still liquid cloud droplets above the freezing level in Fig. 1.6. At the end of this stage, these water droplets and ice crystals become large enough to fall as rain. This stage is very similar for shallow and deep convection though the updrafts in deep convection are often stronger and shallow clouds do not rise high enough for the formation of ice particles, both of which leads to weaker precipitation in shallow cumulus clouds than in deep convection.

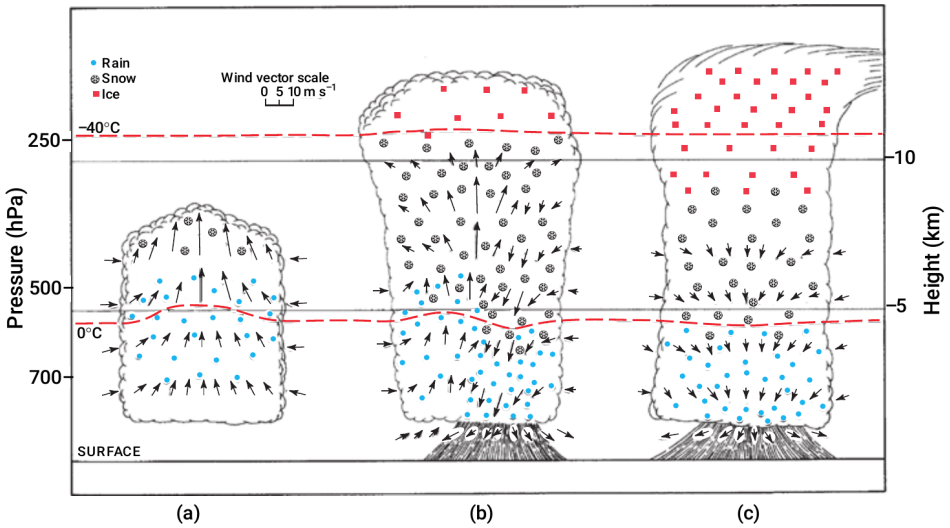

Fig. 1.6.: Schematic of the three stages of the life cycle of a deep convective cloud according to *Byers and Braham* (1949): cumulus state (a), mature stage (b) and dissipating stage (c). The lower red line indicates the $0\,^{\circ}\mathrm{C}$ and the upper red line indicates the $-40\,^{\circ}\mathrm{C}$ isotherm. Note that the horizontal scale is compressed by about 30% relative to the vertical scale [Figure from *Wallace and Hobbs* (2006)].

The transition to the mature stage is defined by rain first reaching the surface. While updrafts still prevail in the upper part of the cloud, precipitation leads to the formation of strong downdrafts in the lower part of the cloud. The downdrafts result from the partial reevaporation of precipitation which cools the air and makes it negatively buoyant and the drag precipitation induces on the ascending air. Once the comparatively cool and dry air from the middle troposphere hits the surface, it is forced to spread horizontally causing a gust front associated with a strong drop in temperature. This phenomena, usually referred to as a spreading cold pool, has probably been observed by everyone during the approach of a thunderstorm.

The Rain in Cumulus over the Ocean experiment (*Rauber et al.*, 2007) has shown that trade wind cumulus clouds frequently precipitate and, while precipitation rates are significantly lower than in deep convection, *Seifert and Heus* (2013) have highlighted the importance of the precipitation induced cold pools for shallow cumulus clouds. This suggests that there is a mature stage of precipitating shallow cumulus clouds, more similar to the mature stage of deep convection than has long been believed.

The dissipating stage is characterized by weak downdrafts prevailing throughout the cell. When the air in the upper level updraft becomes neutrally buoyant, cloud water and ice is detrained which leads to moistening and, through reevaporation, cooling of the surrounding air. When downdrafts extend cover the entire lower cloud boundary, the cumulus cloud is

effectively cut off the buoyant updrafts that feeds it. *Wallace and Hobbs* (2006) call this a "self-destruct mechanism".

1.4. Interaction of convective clouds

In the previous chapter we focused on the properties of a single cloud, given a conditionally unstable atmosphere. To understand how convective clouds can induce organization, it is important to understand how clouds affect the formation of other clouds.

Clouds influence the formation of further convection by perturbing the atmosphere in their surrounding. In particular, they induce perturbations in the free troposphere, by advecting moist and warm air from the boundary layer, and in the boundary layer, where the convectively induced cold pools lead to temperature, moisture and velocity perturbations. In the following we will shortly summarize the properties of these perturbations and their role in organizing convection in the following order:

1. Convection induced temperature perturbations in the free troposphere
2. Cold pool induced perturbations in the boundary layer
3. Convection induced humidity perturbations in the free troposphere

We have sorted them according to the time scales on which the perturbations act, as the way in which they influence the formation of new clouds in the surrounding not only depends on the strength of the perturbations but also on how long they are present. As the cold pool induced perturbations act on the same time scale we treat them together.

1.4.1. Temperature perturbations in the free troposphere

Convection leads to temperature and thus buoyancy perturbations by latent heat release, the net amount of which is given by the amount of precipitation reaching the surface. While latent heat is released throughout the troposphere it is horizontally localized to the cloud area, which in most cases only covers a few percent.

If the atmosphere is locally stable, these perturbations are quickly dispersed by gravity waves. Gravity waves occur between stable layers of fluids of different density, as for example the interface of a pool of water and the atmosphere, if one of the fluids is locally perturbed, for example by dropping a stone into the pool. When the force of gravity acts to restore the equilibrium it causes a local oscillation which propagates as waves, visible as spreading ripples in the water surface.

As indicated by the horizontal lines in Fig. 1.7, one can think of a locally stable atmosphere as consisting of a number of stable layers where gravity waves can spread along the interfaces

of these layers. *Bretherton and Smolarkiewicz* (1989) showed how the buoyancy differences caused by the latent heat release of a (idealized) deep convective cloud is quickly spread by gravity waves. Approximating the local buoyancy perturbation as completely localized horizontally and varying sinusoidally in the vertical, they compared an atmospheric model simulation with theoretical calculations to show that the resulting adjustment of the atmosphere is induced by an outward traveling discontinuous jump from a state of increased buoyancy to the background state. This adjustment process is shown schematically in Fig. 1.7 where the region of increased buoyancy is shown by the light gray area and the discontinuous jump to the white background state propagates with the spreading gravity wave.

The speed with which the adjustment propagates is given by the gravity wave speed, which depends only on the wave number of the vertical perturbation and the stratification, i.e. the stability, of the atmosphere. For real convection, the heating source comprises a superposition of many vertical sine waves, which will induce adjustments traveling at different speeds, reaching maximum speeds of about $50\,\mathrm{m\,s^{-1}}$ for deep convection in the tropics. Calculating the associated velocity field, as indicated by the small black arrows in Fig. 1.7, shows that the adjustment process results from an outflow at the top, an inflow at the bottom and subsidence at the edge. As subsidence leads to adiabatic compression this leads to a warming and thus stabilization of the atmosphere.

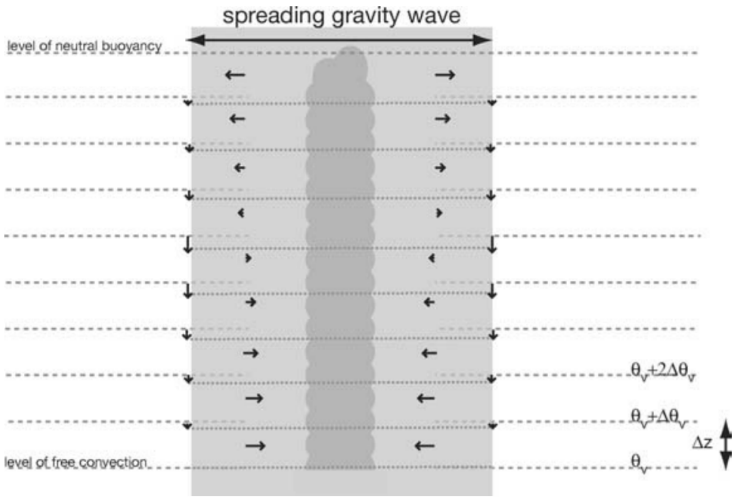

Fig. 1.7.: Schematic of adjustment of the buoyancy field (equivalent to the virtual potential temperature Θ_v) due to cumulus heating following *Bretherton and Smolarkiewicz* (1989). The transient adjustment is accomplished by a spreading gravity wave front. As the subsidence wave moves away from the region of convection, it induces adiabatic compression (*Stevens*, 2005).

In an atmosphere which contains a number of convective cells, gravity waves quickly dis-

perse temperature perturbations, leading to a horizontally almost homogeneous temperature field, and, on average, induce domain wide subsidence, stabilizing the atmosphere. As the resulting stabilization acts almost homogeneously within the entire domain gravity waves mainly affect the amount of further convection.

While convection stabilizes the large scale environment on time scales given by the gravity wave speed, the large scale forcing acts on much slower timescales. In particular, while the large scale forcing changes on time scales of about a day or longer (*Arakawa and Schubert*, 1974), *Cohen and Craig* (2004) used an atmospheric model simulation to show that convection adjusts to a change in the forcing within approximately one hour. This time-scale separation has led to the so called quasi-equilibrium hypothesis, introduced by *Arakawa and Schubert* (1974), which suggests that convection is in statistical equilibrium with the forcing. As the large scale forcing renders the atmosphere unstable to convection at a given rate, convection stabilizes the atmosphere at the same rate. In case of a constant external forcing, this would not be surprising, but that it is a valid approximation despite continually changing external forcing is due to the timescale separation between convective adjustment and the time scale on which the large scale forcing changes. We have already mentioned in section 1.1.3, that this hypothesis is a key ingredient of convection parametrization schemes as it allows the estimation of the convective mass flux from the large scale conditions.

So far we have discussed how the combined effect of gravity waves, induced by convective cells, results in large scale stabilization and thus affects the amount, rather than the spatial distribution, of convection. For completeness, we note however that some studies have suggested that, as gravity waves spread, they may play a role in the triggering or intensification of convection (e.g. *Mapes*, 1993; *Stephan et al.*, 2016). On comparing an atmospheric model simulation with observations *Stephan et al.* (2016), for example, investigated the spreading of gravity waves from two independent convective regions, separated by about 700 kilometers. They found that the arrival of a gravity-wave-related, low level, positive vertical velocity perturbation caused by one of the convective cells coincided with a significant increase in convective activity at the second convective cell, potentially indicating a gravity wave induced intensification of convection. As the relevance of the impact of gravity wave induced triggering and intensification of new convection is still uncertain we will not consider this mechanism in this thesis.

1.4.2. Boundary layer perturbations

Cold pool induced boundary layer perturbations have been found important for the triggering and thus spatial distribution of new convection.

Cold pools have a distinct signature in temperature, moisture and vertical velocity (e.g. *Tompkins*, 2001b; *Schlemmer and Hohenegger*, 2014; *Torri et al.*, 2015) which enables air at the cold pool boundaries to locally overcome CIN. The velocity perturbations stem from

the horizontal spreading of cold air after hitting the surface which pushes the surrounding air upwards. As this leads to strong positive vertical velocity perturbations along the cold pool boundary, this can lead to lifting of air above the convective inhibition layer (e.g. *Purdom*, 1976). While the center of the cold pool is marked by dry and cool air, imported from above the boundary layer and unfavorable for convection, cold pool boundaries are mainly marked by positive humidity perturbations. These moisture perturbations lead to a local decrease of CIN and increase of CAPE (*Tompkins*, 2001b) which allows even small vertical velocity perturbations to trigger convection. A recent study by *Torri et al.* (2015) shows that the humidity and the velocity perturbations are important at different stages of the triggering process.

Note that cold pools, which have on average life times on the order of two or three hours and extend within that time to radii of about ten kilometers (e.g. *Tompkins*, 2001b), propagate significantly slower than the gravity waves discussed in the previous section. Thus convection on the one hand induces large scale subsidence which stabilizes the atmosphere while on the other hand increases the probability for the formation of new convection within its vicinity.

The central role of cold pools in triggering new convection has strong implications for the spatial and temporal distribution of updrafts. In particular, it affects the observed size distribution and the propagation of convective activity.

That clustering is likely to affect the observed size distributions can be seen in Fig. 1.2, taken from a study conducted by *Seifert and Heus* (2013). In their study they use a high-resolution simulation to investigate the organization of shallow cumulus clouds and the role of cold pools therein. As they find that the cold pools are best seen in the humidity field, in particular during the later stages of their evolution, Fig. 1.2(b) shows the deviation of the vertically averaged sub-cloud layer moisture from the horizontal mean. The increase of humidity in ring like structures marks the position of the cold pool boundaries. In addition, clouds are indicated in Fig. 1.2(b) by contours of the cloud liquid water path. It is obvious that most clouds are clustered on top of the cold pool induced regions of increased humidity. This clustering makes merging of individual clouds to cloud clusters or equivalently clouds containing multiple cloud cells, as previously observed by *Hozumi et al.* (1982), *Wielicki and Welch* (1986), *Cahalan and Joseph* (1989) and *Kuo et al.* (1993), likely. Many of the isolines indicating cloud boundaries close to (-20 km,-20 km) in Fig. 1.2(b) for example, are so close to each other that it is difficult to distinguish whether they indicate single or multiple clouds. In chapter 2 of this thesis we will investigate how size distributions are affected if cloud size distributions are really size distributions of cloud clusters, i.e. of clouds forming too close to each other to be distinguished.

Triggering of new convection not only affects the spatial distribution of updrafts but also leads to the spreading of convective activity. *Tompkins* (2001b) analyzed snapshots of successive boundary layer temperature fields and showed that most of the convective events

occur on the cold pool edges of previous convective events, see Fig. 1.8. A full discussion is given in *Tompkins* (2001b) but the induced spreading of convection can be exemplified by focusing on convective activity spreading from a preexisting cold pool which must have originated from convection situated somewhere near A. At time zero, three events (B, C, D) have been triggered by this cold pool. One and a half hours later, the cold pool stemming from convection close to A is no longer discernible, while the cold pools resulting from the events at B,C and D have grown substantially. *Tompkins* (2001b) note that the outflow of events C and D trigger two new events, M and N, where they meet the outflow of a convective event at L. Thus, convection has spread within the domain: originally located close to A, it triggered new convection at C and D which in turn triggered convection at M and N.

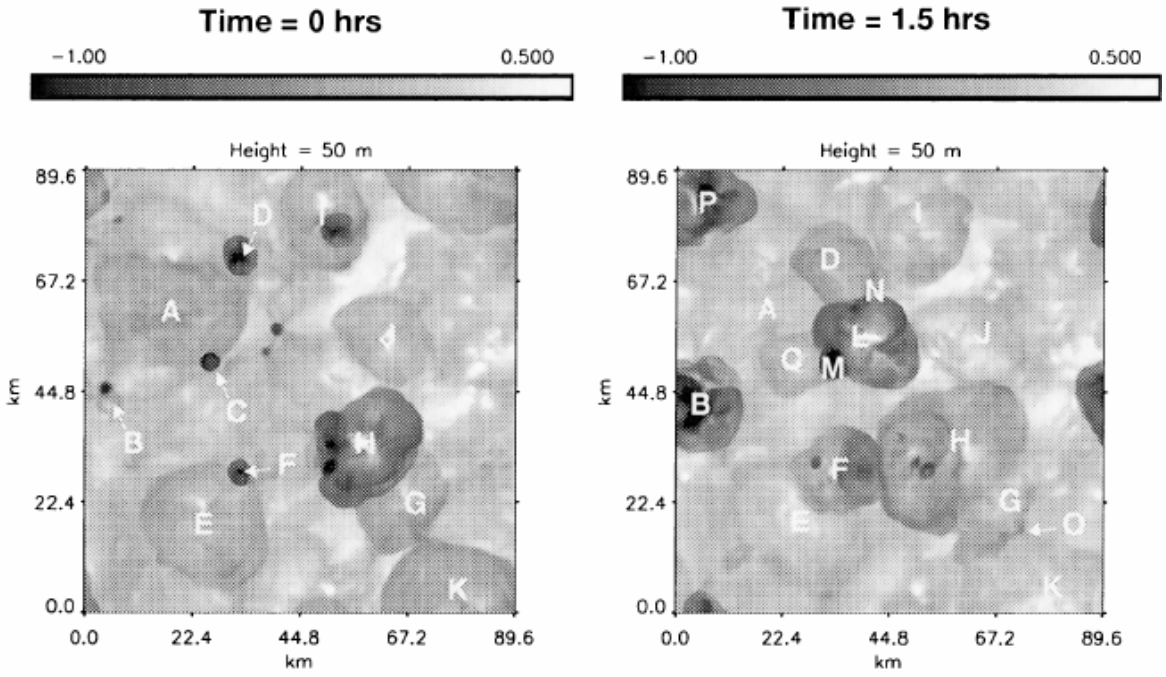

Fig. 1.8.: Two successive snapshots of temperature perturbations [K] at a height of 50 m in an atmospheric model simulation of deep convection performed by *Tompkins* (2001b). The right snapshot is taken 90 minutes after the left snapshot.

1.4.3. Humidity perturbations in the free troposphere

On transporting moist boundary layer air into the free troposphere, convection induces local humidity perturbations. While some part of upward transported humidity will fall out as precipitation, and induce the formation of cold pools as discussed above. The remaining part of the upward transported humidity, however, will lead to a local moistening of the free

troposphere. *Bretherton and Smolarkiewicz* (1989) showed that these moisture perturbations are spread by turbulent mixing and detrainment on a much longer time-scale than buoyancy differences and *Tompkins and Craig* (1998) found that it took about 30 days in their simulation to remove humidity perturbations as they have to be vertically advected through the free troposphere by large scale subsidence. Thus, while the horizontal temperature field in the tropics is almost homogeneous, the moisture distribution is found to be only locally correlated.

The longevity of humidity perturbations is important as the horizontal distribution of humidity affects the spatial distribution of convection. In particular, *Parsons et al.* (2000) and *Redelsperger et al.* (2002) showed that anomalously dry air suppresses the formation of deep convection. Using observational and modeling data respectively, they showed that the intrusion of dry air into a domain with active deep convection strongly decreased the likelihood for the formation of further deep convection. Testing the sensitivity to the vertical distribution of humidity distribution suggests that deep convection is most sensitive to the free tropospheric humidity content (*Derbyshire et al.*, 2004; *Holloway and Neelin*, 2009; *Bretherton et al.*, 2004). *Derbyshire et al.* (2004), using different single column and cloud resolving model simulations, found that deep convection was predominant only for high midtropospheric humidity. *Holloway and Neelin* (2009) and *Bretherton et al.* (2004) evaluated observational data which also showed that high free tropospheric moisture content is favorable for deep convection, and thus high precipitation rates, while boundary layer moisture had no significant influence on convection.

This dependence of convection on humidity is important as idealized simulations of the tropical atmosphere, based on the so called radiative-convective equilibrium (RCE) approximation, show self-amplification of humidity perturbations. In RCE simulations, the tropical atmosphere is represented neglecting dynamical forcing, rotational effects, temporal variations resulting from the diurnal cycle and, in addition, the lower boundary is assumed to be an ocean surface of fixed temperature. If started from slightly perturbed, homogeneous, initial conditions, humidity perturbations in RCE simulations, in contrast to temperature and cold pool perturbations, have been found to amplify and grow. Once started, the simulations often reach a new equilibrium state, with a single, moist and convecting region surrounded by a dry, subsiding region. To reach this new equilibrium takes days or weeks, however, which is significantly longer than the life time of a single deep convective event.

Instability of the tropical atmosphere to humidity perturbations is also found in weak-temperature gradient (WTG) simulations. Simulating a small subdomain within a large tropical region, the response of the atmosphere to a temperature perturbation can be expressed as a relaxation of the temperature to a reference profile, as any perturbations in a large domain would be quickly removed by a compensating vertical velocity. Compared to temperature perturbations, humidity perturbations are long-lived and thus the humidity profile cannot simply be relaxed to a reference profile. In fact, besides the resolved humidity perturbations caused by convection, humidity in a large domain would also be affected by the compensating ver-

tical velocity. Determining a, hypothetical, vertical velocity necessary for the temperature adjustment, mass continuity allows to determine the amount of inflow, outflow and vertical transport of humidity. If there is any inflow from the outside, a reference humidity profile is used.

Introduced by *Sobel et al.* (2007), the stability of humidity perturbations in WTG simulations can be tested with the two following steps. First, an equilibrium humidity profile is determined by using a small domain RCE simulation[1]. Second, the stability of the atmosphere is tested by reducing or increasing the humidity content. Depending on setup details like sea-surface temperature and strength of surface fluxes, the atmosphere responds in two different ways. It either returns to a humidity profile similar to the unperturbed profile, showing that the atmosphere is stable to the perturbation, or the initial humidity perturbation amplifies until a new, dry or moist, equilibrium state is reached. While deep convection persists in the moist state, no convection occurs in the dry state. As the results obtained by *Sessions et al.* (2010) suggest that the final dry or moist state does not depend on the amplitude of the perturbation this indicates that the atmosphere is bistable. An atmosphere that supports a stable moist and a stable dry state is generally referred to as an atmosphere with *multiple equilibria*. Multiple equilibria have been observed in a number of subsequent studies (*Sessions et al.*, 2015, 2016; *Emanuel et al.*, 2014).

1.5. Idealized models of convection

In the main chapters of this thesis we will address the question of how the properties of convection, reviewed above, lead to the observed power-law size distributions and self-aggregation. To this end we will represent the respective mechanisms using minimally simple models. As a number of conceptual models, fulfilling different aspects of this objective, have already been introduced, we will now give a short review of these models. In particular we categorize the models according to their original purpose and, after shortly describing the formulation of each model, discuss the relation to the objective outlined above.

1.5.1. Models for convection parameterization

As already summarized in section 1.1.3, one of the main reasons for introducing simple models of convection is the need to represent convection in atmospheric models whose resolution is too coarse to resolve convection explicitly. The focus of these models is to describe the convective response triggered by the large scale state of the atmosphere and to determine how

[1] As self-aggregation only occurs for large domain sizes with a minimal horizontal domain length of about 200-300 km (e.g. *Bretherton et al.*, 2005), it does not affect the equilibrium profiles.

the resulting convection feeds back onto the larger scales. As we have noted above, common parameterization schemes do not account for spatial or temporal correlations between different convective cells.

To remedy this shortcoming, a number of studies have used two dimensional lattice models to represent sub-grid scale convection in global circulation models (*Majda and Khouider*, 2002; *Khouider et al.*, 2010; *Bengtsson et al.*, 2011; *Dorrestijn et al.*, 2013). Each site of the lattice is in one of a small set of states, for example clear sky and cloudy. As grid-cells represent single clouds, they have length scales on the order of one kilometer. By specifying the transition rules, lattice models provide an easy way to include spatial and temporal correlations between convective events.

Majda and Khouider (2002) were the first to describe convection in this way, using two possible states: *convection inhibited* and *potential for deep convection*. Randomly choosing a site, this site flips with a certain probability. While the probability for a site with potential for deep convection to flip to the convection inhibited state is fixed, the probability for a site to flip in the opposite direction depends on the large scale state and on the neighboring sites. In particular it is more likely to switch form a convection inhibiting state into a convection permitting state if the large scale forcing favors convection and the site is surrounded by other convection permitting sites. One time step is given by having, on average, chosen each grid site once. These rules are defined in an ad hoc manner.

In contrast to *Majda and Khouider* (2002), in the models introduced by *Khouider et al.* (2010), *Bengtsson et al.* (2011) and *Dorrestijn et al.* (2013) all sites are updated at the same time with the transition probabilities depending on the model state of the previous time step but not on any state before that. Note that the transition rates may still depend on large scale variables supplied by the atmospheric model or on neighboring states.

Khouider et al. (2010) use a set of four possible states (clear sky, congestus cloud, deep cloud, stratiform cloud) with transition rates which depend on the state at the previous time step and the environment but not on the states of the neighboring sites. The different states allow the model to mimic the natural life-cycle of a cloud and the dependence of cloud type on the mean atmospheric condition, in particular CAPE and relative humidity content of the middle troposphere. Again the transition rates are motivated by physical intuition.

Bengtsson et al. (2011) used a cellular automaton (CA) to include interaction with neighboring sites but limited the set of states to two (clear sky and cloud). The transition rules are based on the rules of the famous *game of life* cellular automata model (see *Chopard and Droz* (1998) for an introduction to cellular automata and a description of the game of life CA): a cloudy site will remain unchanged if, at the last time step, it had two or three cloudy neighbors, while a non-cloudy site becomes cloudy if it is surrounded by exactly three neighboring cloudy sites. As their aim is to represent the formation of convective clouds triggered by quickly traveling gravity waves, they use a short time-step of only two minutes. To correctly represent cloud life times, which are on the order of hours, each cloudy site survives

exactly 30 time steps in unfavorable conditions (i.e. other than two or three cloudy neighbors).

In contrast to the previously described models, *Dorrestijn et al.* (2013) determine the transition rates from an atmospheric model simulation. They discretize the model domain and define five different states, one clear sky and four cloud type states, according to rain rate and cloud height. Comparison of successive time steps allows them to estimate the transition rates. In addition to simple averages over all time-steps, they condition the transition rates on external conditions and on nearest neighbor states. Comparison of the resulting models with and without nearest neighbor interaction shows that spatial coupling is necessary to obtain realistic variability in the coverage fractions of the different cloud types.

While validation of these schemes has focused on whether the lattice models lead to an improved representation of variability and cloud fraction, they have, to the best of our knowledge, not considered the resulting size distributions. The simple way in which these lattice models include interaction between different convective clouds will however serve us as a starting point for introducing a model that describes spreading of convective activity in chapter 3. In contrast to the ad hoc way in which the transition rules are defined above, we will motivate our transition rules by a detailed examination of the cold pool triggering process.

1.5.2. Model of cold pool interaction

Instead of defining ad hoc transition rules to represent spatial and temporal correlations as in the previously reviewed lattice models, *Böing* (2016) introduced a coupled two layer lattice model which includes some of the key dynamical features of precipitating convection, in particular cold pools. The aim of the model is to assess what determines the spatial pattern of shallow cumulus clouds.

Each lattice site contains particles which, in the lower layer, represent air parcels that are becoming unstable to moist convection and in the upper layer, air parcels undergoing moist convection. Radiative cooling is modeled by randomly adding particles to the lower layer. Convection starts when the particle number in a lower layer site exceeds a threshold and is modeled by transporting all the particles of that site to the corresponding upper layer site. After a given delay time, upper layer particles turn into precipitation particles, which disappear after a fixed length of time. Rainy clusters are defined as connected sites which precipitate. Particles in the lower layer are blown away under rainy clusters to mimic the effect of cold pools. As the velocity is chosen to be largest below the center of the rainy cluster and decreases with increasing distance, cold pools can lead to a local increase of particle density and thus the triggering of new convection.

While visual comparison with simulations and observations shows realistic looking cloud fields, the model introduced by *Böing* (2016) is still comparatively complicated and relies on

the specification of a large number of free parameters. We will argue in chapters 2 and 3 of this thesis that an even more basic representation of cold pool clustering and triggering can explain the emergence of power-law scaling.

1.5.3. Models to explain power-law scaling and self-aggregation

Power-law scaling

The two models for convection investigated by *Muller et al.* (2009) and *Stechmann and Neelin* (2014) were introduced with the aim to explain the observed power-law pick up of precipitation above a critical humidity content and the peak in variance at the critical value, as observed by *Peters and Neelin* (2006), and the power-law distribution of precipitation events (*Peters et al.*, 2001). The models contain no spatial information but represent the mean humidity content and precipitation strength on scales of about 20 km.

The model introduced by *Muller et al.* (2009) has three basic properties. First, it assumes that the humidity content of the boundary layer and the free troposphere are uncorrelated and each drawn from a Gaussian distribution with the same mean and standard deviation. Second, convection only occurs if the boundary layer humidity content crosses a given humidity threshold. Third, the height of the resulting convection and therefore the amount of precipitation is a linear function of the sum of the two humidity values. Based on only these three properties, they find that repeated drawings can roughly reproduce the functional dependence of precipitation rate and variance on humidity but not the power-law scaling.

Also based on a precipitation onset above a critical humidity content, *Stechmann and Neelin* (2014) introduce a time evolution equation for the humidity content, which evolves according to a stochastic differential equation. In the absence of convection, the humidity content increases, representing evaporation at the surface, while in the presence of convection humidity decreases, as water condenses and falls out as precipitation. Convection and precipitation rate are, similar to the lattice models introduced above, characterized by two (or three) states: no convection and deep convection (and stratiform convection). In case of two possible states, the state of deep convection is first entered when the humidity content crosses a critical threshold and left when it falls below a second threshold, lower than the first threshold. During the state of deep convection a constant precipitation rate is assumed. Analytic calculation shows that the event size distributions follow a power-law with an exponent of -1.5, above a lower and below an upper cut-off. While the functional form compares well with the observational data the exponent is larger than the observed power-law exponents.

While both models are thus able to approximately reproduce at least some of the observations we want to explain in this thesis we note two draw-backs. First, neither of the models considers spatial interactions though these seem to be intimately related to the other observations (*Peters et al.*, 2009). Second, both models simply assume a critical humidity value

without explaining its origin, even though the existence of the critical value is one of the most interesting observations.

Self-aggregation

While the models discussed so far consider the properties of interactions of single convective events, the models introduced by *Bretherton et al.* (2005), *Craig and Mack* (2013) and *Emanuel et al.* (2014) show how enhanced or decreased convective activity can contribute to a positive feedback loop which allows moist or dry perturbations to grow and thus leads to self-aggregation.

Bretherton et al. (2005) use a semi-empirical model to determine the processes which lead to the origin of bistability in the humidity content. They show that while convection is increased in moist regions, increased convection leads to a positive feedback from radiation, surface fluxes and horizontal advection.

The feedback of convection on humidity perturbations in the model proposed by *Craig and Mack* (2013) is motivated by the process of detrainment. Convection, occurring preferentially in regions with a moist free troposphere, will transport humidity out of the boundary layer into the free troposphere, as increased surface fluxes quickly remoisten the boundary layer this induces a net increase in the humidity content. Again this positive feedback leads to bistability in the humidity content. They show in addition that, assuming that the horizontal exchange of humidity can be described as diffusive, self-aggregation can be described by a process called coarsening.

Emanuel et al. (2014) showed that positive (negative) perturbations in the tropospheric humidity content can lead to reduced (increased) radiative cooling. These temperature perturbations are quickly removed by gravity waves which induce increased subsidence in the cool regions and thus a decrease in convective mass flux which, in turn, leads to a decrease in moistening, yielding a third possible explanation of the bistability of the atmosphere.

Our objective in chapter 4 of this thesis is to describe the spatial evolution of self-aggregation. So far, only the model introduced by *Craig and Mack* (2013) can describe the spatial evolution which has however two important limitations. First, analysis of simulations showing self-aggregation suggest that the relevant feedback mechanism might be different from the feedback proposed in *Craig and Mack* (2013) and second, their assumption of a diffusive interaction term lacks physical motivation.

1.6. Outline

The aim of this thesis is to introduce physically motivated but maximally simple models to give quantitative predictions of the following observed phenomena (reviewed in section 1.2.2):

P1 Size distribution of shallow cumulus clouds and the impact of cold pool induced clustering

P2 Spreading of convective activity, the role of cold pool triggering and its relation to the continuous phase transition of precipitation

P3 Spatial evolution of self-aggregation

The three phenomena are different manifestations of convective organization. We have selected them due to their important feed backs on the larger scales, in particular their impact on the radiative properties of the atmosphere, the expected variance in convective activity and the mean humidity content of the atmosphere (1.2.4).

We base these models on the properties of convection reviewed above (1.4), from which we infer the following simplified view on convectively induced spatial and temporal correlations: while the average amount of convection is determined by the large scale forcing, the spatial and temporal evolution of convective cells on short time scales is determined by cold pools while on larger time-scales it is determined by free tropospheric moisture perturbations to which convection itself contributes by an upward transport of humidity.

Comparison of our objective with the theoretical models introduced in section 1.5 shows that different models already address parts of these questions. On the one hand, temporal and spatial correlations between convective events have been represented in lattice models, though with either intuitively chosen or complicated transition rules. On the other hand, models which have attempted to explain power-law scaling in size distributions and self-aggregation generally lack spatial interactions, with one noted exception (*Craig and Mack*, 2013). The models we introduce in this thesis will therefore, at least partly, build on some of these models.

The outline of the thesis is as follows: we dedicate one chapter to each of the observed phenomena with the order of chapter given by the listing above. For better readability we will begin each chapter with a short literature review on the observed properties and the properties of the associated simple model.

To address P1 in chapter 2 we start by assuming that size distributions result from merging of randomly distributed cloud cells. We test the resulting implications on a large satellite data set from which we deduce that we need to account for clustering. To determine the effect of clustering we introduce a simple model which reproduces the spatial distribution of clouds observed in the satellite scenes.

At the beginning of chapter 3, in which we address P2, we review results from *Peters and Neelin* (2006) and some aspects of non-equilibrium phase transitions and self-organized criticality. This prompts us to introduce a 2D lattice model which represents spreading of convection caused by cold pool triggering and which shows an underlying phase transition of convective activity as a function of trigger probability. We then introduce methods to determine the free parameters from an atmospheric model simulation and compare the spreading observed in the atmospheric model with spreading observed in the lattice model.

Based on the results of the previously introduced models of self-aggregation (1.5.3), we address P3 in chapter 4 by determining under what conditions the spatial evolution is indeed described by coarsening (*Craig and Mack*, 2013). To this end, we review the proposed positive feedbacks and introduce a physical explanation for the horizontal interaction term. Using these results we compare properties of three modified versions of the original self-aggregation model introduced by *Craig and Mack* (2013) to properties frequently observed in radiative-convective equilibrium simulations.

Finally we summarize our main conclusions and discuss the relation between the three different models in the first part of chapter 5. In the second part, we discuss some additional tests necessary to verify the simple models and also how one could proceed to use the here introduced models for an improved representation of convection in climate models and to increase our physical understanding of how organization can impact large scale circulations.

2. Size distribution of shallow cumulus clouds

2.1. Introduction

Size distributions of shallow cumulus clouds have been frequently shown to exhibit power-law scaling, although often only over a restricted range of scales (see section 1.2.3). In this chapter, we investigate the relation of the observed power-law scaling to the geometrical phase transition of percolation. Percolation has already been shown to, at least partly, explain observed properties of size distributions in deep convection (*Peters et al.*, 2009). We start by a short review on percolation, which we base on the books by *Stauffer and Aharony* (1994) and *Gould et al.* (2005).

2.1.1. Percolation

Percolation, which discusses the properties of randomly distributed objects and the clusters they form through overlapping, is a geometric problem rather than a physical one. While its rules are readily explained in a few sentences, the arising behavior is far from trivial and only few analytic solutions are known in dimensions higher than one.

Imagine an infinitely large square lattice, where each site is either occupied with probability p or not occupied with probability $1 - p$. As p has the same value for all lattice sites, the lattice sites are completely independent of each other and the total fraction of occupied sites, which we call the coverage fraction, is also given by p. An example for a small square lattice with $p = 0.30$ is shown in Fig. 2.1, where the black sites correspond to occupied sites.

All occupied sites which are connected via nearest neighbors correspond to a *cluster*, indicated by the red circles in Fig. 2.1. The properties of these clusters play a central role in percolation theory. It can be readily believed that the size of the formed clusters tends to increase with increasing coverage fraction. In an infinite domain, the first appearance of an infinitely large cluster (also called percolating cluster) is marked by a phase transition at $p = p_c$. Below the critical coverage fraction p_c, also called the percolation threshold, the probability for an infinite cluster is zero, while the probability is one above the critical

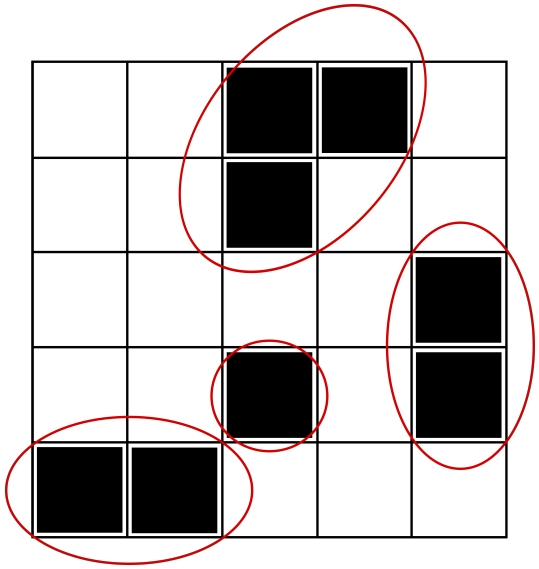

Fig. 2.1.: Random realization of a small square lattice with occupation probability $p = 30\%$. Occupied sites are shown in black and the resulting clusters of occupied sites are encircled in red.

coverage fraction. In a finite domain, the phase transition is marked by a sharp increase in the probability for a cluster which spans the entire domain. The value of the percolation threshold for the square lattice model introduced above is not known analytically but has been estimated to be approximately $p_c \approx 0.59$.

Phase transitions in general are described by a control parameter and an order parameter. As the control parameter is increased, in case of percolation the control parameter is the coverage fraction, an order parameter, which describes the macroscopic state of the system, changes abruptly. A common choice for the order parameter in percolation is the strength of the percolating cluster P_s, which is given by the fraction of occupied sites which belong to the infinite cluster. Below p_c there is no infinite cluster and thus $P_s = 0$. It has been found that P_s is still zero at the percolation threshold but increases as a power-law above:

$$P_s(p) \sim (p - p_c)^\beta \tag{2.1}$$

where β is one of the critical exponents of the phase transition and $\beta = 5/36$ for 2D percolation. The phase transition is called a *continuous phase transition* because, as the control parameter passes through the critical probability, it shows a singular albeit continuous behavior.

Apart from a power-law increase of the order parameter, the percolation threshold is also marked by a power-law decay in the cluster size distribution. In the square lattice model, the size of a cluster s is given by the number of occupied sites which make up the cluster and

the cluster size distribution n_s is defined as the number of clusters with size s per lattice site. At criticality

$$n_s(p_c) \sim s^{-\tau} \tag{2.2}$$

where τ is an other critical exponent with $\tau = 187/91$ in two dimensions.

The applicability of percolation to physical systems is largely due to the *universality* of many of the properties listed above. Universality refers to the insensitivity of certain quantities of continuous phase transitions, foremost critical exponents like β and τ, to details of the setup. For example, while we have above introduced percolation on a 2D square lattice, the functional dependence and the values of the critical exponents in the scaling relations given in Eqs. 2.1 and 2.2 are the same for different lattice structures (triangular, hexagonal, etc.) or for the continuum case where, instead of sites in a lattice, objects (e.g. disks) are randomly distributed within a domain until a given fraction of the domain is covered. Note however that the percolation threshold is non-universal and that the critical exponents depend on dimensionality. All models which have the same universal behavior are said to belong to a *universality class* and it is commonly assumed that all continuous phase transitions belong to a finite set of universality classes (e.g. *Hinrichsen*, 2006).

For the following discussion of shallow cumulus size distributions in the context of continuum disk percolation, we also note that the universal properties of percolation have been suggested to remain unchanged if the individual disks are drawn from a power-law distribution, at least as long as the power-law drops fast enough, (*Sasidevan*, 2013) and if the disks are not randomly distributed in space but attract each other (*Duckers and Ross*, 1974; *Cooper et al.*, 1989; *Martin et al.*, 1987) though in the latter case, results have been found to be inconclusive.

As cloud fractions in shallow cumulus cloud situations are in general much smaller than the 2D percolation threshold of continuum disk percolation (approximately 68%; e.g. *Mertens and Moore*, 2012), we suggest that subcritical percolation is more appropriate for the description of cloud fields. While universal behavior is usually confined to the behavior near criticality, *Ding et al.* (2014) found some degree of universality in a numerical analysis of the cluster size distributions for coverage fractions smaller than the critical coverage fraction.

In particular, on comparing cluster size distributions for different lattice types and different coverage fractions they find that all size distributions are described by

$$\log n_s(p) = as - b \log s + c. \tag{2.3}$$

Rewriting (2.3) as

$$n_s(p) = \exp(as) s^{-b} \exp(c)$$

shows that, as in the critical case, the cluster size distribution $n_s(p)$ scales with cluster size s as a power-law, with an exponential cutoff (note that a is expected to be negative). The parameters a, b and c depend on coverage fraction such that on approaching the critical

fraction, the power-law regime steepens and extends to larger cluster sizes. *Ding et al.* (2014) moreover show that the dependence of the parameters on coverage fraction shows some universal properties, for example the functional dependence of a on coverage fraction is independent of lattice type.

In this chapter, we first investigate the hypothesis that size distributions of shallow cumulus clouds are described by subcritical percolation by testing whether the properties predicted by subcritical percolation are observed in cloud size distributions obtained from a large set of satellite images. We find agreement in the shape of the distribution and its sensitivity to coverage fraction. Using a modified percolation model that includes an underlying exponential distribution of convective cell size and a simple representation of cell clustering, we obtain quantitative predictions of the power law slope and the position of the scale break.

2.2. Data

2.2.1. Satellite Data Set

Using satellite data we now test whether observations of shallow cumulus cloud fields yield cloud size distributions with a functional dependence as predicted by subcritical percolation including the sensitivity to coverage fraction. To determine size distributions from satellite scenes, a reflectivity threshold is chosen for each scene, dividing the domain into cloudy (high reflectivity) and background (low reflectivity) pixels and then defining clouds as groups of nearest neighboring cloudy pixels. The 152 satellite scenes chosen for this study were previously used by *Zhao and Di Girolamo* (2007) for a comprehensive study of trade wind cumulus clouds over the tropical southwestern Atlantic ocean [1] The data was taken by a multispectral imager, the Advanced Spaceborne Thermal Emission Reflection Radiometer, on-board the EOS Terra spacecraft. All scenes use the 3N near infrared channel ($0.78\,\mu\mathrm{m}$ to $0.86\,\mu\mathrm{m}$), have a spatial resolution of 15 m and cover an area of approximately $60\,\mathrm{km} \times 60\,\mathrm{km}$, but are divided into four equal subregions for our analysis to improve sample size. The same thresholds as in the preceding study are used and an example of a $10\,\mathrm{km} \times 10\,\mathrm{km}$ subsection of an image after thresholding is shown in the inset in Fig. 2.2, with cloudy pixels in white and background pixels in black.

2.2.2. Cloud Size Distributions

The cloud coverage in the analyzed satellite images varies from 0.1% up to nearly 40% so to test the hypotheses that the cloud size distributions are sensitive to coverage fraction and that,

[1] The complete list of filenames and thresholds can be found in the study by *Zhao and Di Girolamo* (2007).

for a given coverage fraction, the size distribution fits Eq. 2.3, we divide the satellite scenes into subgroups according to cloud fraction. To this end we first sort the scenes by cloud fraction and then divide them into 15 subgroups, each with the same number of scenes. The size distributions n_s of four of these subgroups are shown in Fig. 2.2, together with best fit curves following Eq. 2.3. Here, n_s is the number of clouds with areas in the interval $[s, s + \Delta s)$ per domain area and divided by Δs. All size distributions are calculated using exponentially increasing bin-widths. We only consider bins for which the number of clouds is larger than the number of satellite scenes in each subgroup and note that among the thus neglected clouds are clouds with areas significantly larger than expected from Eq. 2.3.

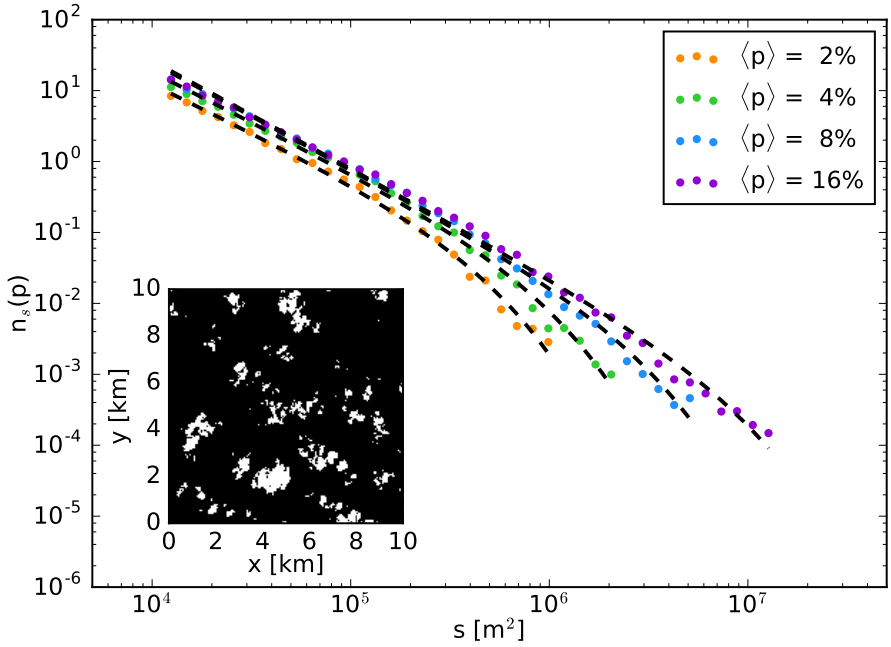

Fig. 2.2.: Cloud size distributions determined from satellite scenes most similar in cloud fraction (colored lines) and best fit curves following Eq. 2.3 (dashed black line) with the average coverage fraction given in the legend. The inset shows a section of a sample satellite scene.

Inspection of Fig. 2.2 shows that for each subgroup the size distribution can be fitted by Eq. 2.3, as predicted by subcritical percolation theory (*Ding et al.*, 2014). The dependence of the fitted parameters a, b and c on cloud fraction is shown in Fig. 2.3. According to Eq. 2.3 parameter a determines the position of the exponential drop-off, in particular as a decreases the range of power-law scaling extends to larger clusters, while an increase in parameter b corresponds to a steeper power-law decay and an increase in parameter c is related to an increase in the total number of clusters. Figure 2.3 therefore shows that the size distribution changes with increasing coverage fraction in a systematic way: the power-law scaling extends to larger clusters and the power-law exponent increases. While this is

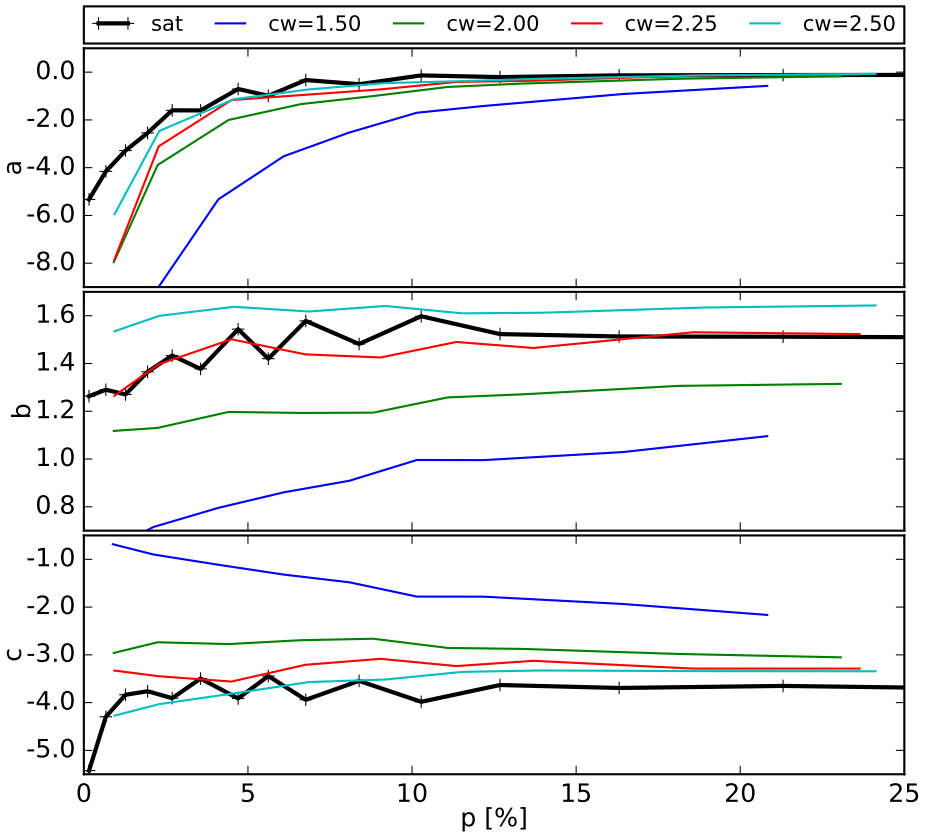

Fig. 2.3.: Dependence of the size distribution parameters in the satellite data (black lines) and in the modified subcritical percolation model (colored lines) on coverage fraction p, where different colors correspond to different clustering widths cw.

in qualitative agreement with lattice percolation (*Ding et al.*, 2014), power-law scaling is already apparent at lower cloud fractions than expected from standard percolation theory.

In percolation, power law size distributions are associated with the presence of large objects that occur when the density is great enough that merging of the randomly distributed elements becomes frequent. An obvious hypothesis why merging could be more common is the observed clustering of clouds (*Sengupta et al.*, 1990; *Nair et al.*, 1998; *Zhao and Di Girolamo*, 2007; *Seifert and Heus*, 2013). As we have reviewed in section 1.4.2, convective updrafts are organized by boundary layer circulations, particularly those created by previous generations of clouds via cold pools. This motivates us to construct a percolation model that favors the presence of clouds near existing cells.

2.3. Model

2.3.1. Modified Continuum Percolation Model

To evaluate the hypothesis that clustering will lead to power law scaling at smaller coverage fractions, we introduce a modified version of the standard continuum percolation model with a simple representation of cloud clustering. We will not attempt to model the shapes of individual convective cells, which will be represented by circular disks, and will focus the analysis on larger clouds that consist of overlapping disks. A potentially complicating factor is that individual cells are not of uniform size, but appear to follow a size distribution closer to exponential (*Kuo et al.*, 1993). An exponential distribution of cell size is also predicted by theory and numerical simulations for deep convection (*Craig and Cohen*, 2006; *Cohen and Craig*, 2006; *Scheufele*, 2014). Rather than distributing identically sized disks, disk sizes are therefore drawn from an exponential distribution with expected value $\langle s^d \rangle = s_m^d$. Clustering is included by increasing the probability for the appearance of a new cell center in the vicinity of existing clouds. Two parameters will be introduced to describe the clustering: the clustering strength cs, which determines how much the probability is increased, and the clustering width cw, which determines the area of increased probability.

The model successively distributes N cloud disks within a square domain of length L. To estimate N we use the results from *Chandrasekhar* (1943) and *Shante and Kirkpatrick* (1971), who show that the fraction of area covered by N randomly distributed disks with area s_m^d within a domain of size L^2 is given by

$$p = 1 - \exp(-\frac{N s_m^d}{L^2}) \tag{2.4}$$

in the limit of a infinite domain and a finite but nonzero density of disks. Solving for N we can estimate the number of disks necessary to cover a fraction p of the domain.

The area of the individual cells s_i^d with i in $\{1, ..., N\}$ are drawn from the exponential distribution with expected value $\langle s^d \rangle = s_m^d$ and the corresponding radius r_i^d is computed from the area. To avoid larger clouds completely overlapping smaller clouds, we sort them in descending order before distributing them successively.

Clustering is included by increasing the probability for the appearance of a new disk center in the vicinity of existing disks. To this end, the cloud centers $\boldsymbol{x}_i = (x_i, y_i)$ are no longer distributed independently but are drawn from a two-dimensional probability density function (PDF) $f_i^{PDF}(x, y)$, with x and y in $[0, L]$, which is constructed from disks $\{1, ..., i-1\}$ through the following steps:

1. $f_i^{PDF}(x, y) = 1$ within the entire domain, i.e. $\forall x, y$, to have a constant background probability

2. $f_i^{PDF}(x,y) = cs$ within the surrounding of all previously distributed disk centers, in particular $\forall x, y$ for which $|\boldsymbol{x} - \boldsymbol{x_j}| \leq cw \cdot r_j^d$ for j in $\{1, ..., i-1\}$, to induce clustering
3. $f_i^{PDF}(x,y) = 0$ within the area covered by the previously distributed disks, i.e. $\forall x, y$ for which $|\boldsymbol{x} - \boldsymbol{x_j}| \leq r_j^d$ with j in $\{1, ..., i-1\}$, to avoid new cloud centers to fall within other clouds
4. $f_i^{PDF}(x,y)$ is normalized using $\iint f_i^{PDF}(x,y)\mathrm{d}x\mathrm{d}y = 1$ to obtain a PDF

Thus the center of the first disk is drawn from a uniform distribution, as in the standard percolation model, but the distribution of all further disks is modified by the previously distributed disks.

Note that we use Eq. 2.4 only to estimate the number of clouds, the actual coverage fraction is determined from the final model realizations. This is important as we observe increasing deviations from Eq. 2.4 for large coverage fractions in consequence of clustering.

The resulting model is completely determined by the global coverage fraction p and three parameters that are assumed to be local properties of the cells and independent of the overall cloud fraction: the mean area of the individual convective cells s_m^d and the cluster width factor cw which gives the maximum distance to the cloud center where the probability is increased by cluster strength factor cs. We will refer to these three parameters as the *local parameters* in the following.

2.3.2. Estimation of the Local Parameters

Estimates for the three local model parameters are deduced from the satellite data as follows. We first estimate the average cell size s_m^d by assuming that for satellite scenes with very low cloud fractions the vast majority of clouds consist of a single, non-overlapping cell. In this case, s_m^d is simply the total cloud area A divided by the number of clouds N. Figure 2.4 shows N versus A for all satellite scenes. As expected, the number of clouds increases rapidly with covered area for small cloud fractions, while for larger cloud fractions the formation of clusters becomes important and the number of clouds increases more slowly. The mean cell size s_m^d is estimated from a linear fit for the smallest cloud fractions, indicated in Fig. 2.4, which gives a mean radius of approximately $r_m^d = 60$ m (corresponding to $s_m^d = 11.3 \times 10^3$ m^2).

To estimate the clustering parameters we find values that approximately reproduce the radial distribution functions (RDFs) calculated from the satellite data. RDFs have previously been used to study the spatial distribution of clouds (e.g. *Cohen and Craig*, 2006) and describe how the number of cloud centers varies as a function of distance from a reference cloud center. It is rescaled such that a completely random distribution of clouds would give a value of one for all distances. RDFs of all satellite scenes with cloud fractions between 4% and

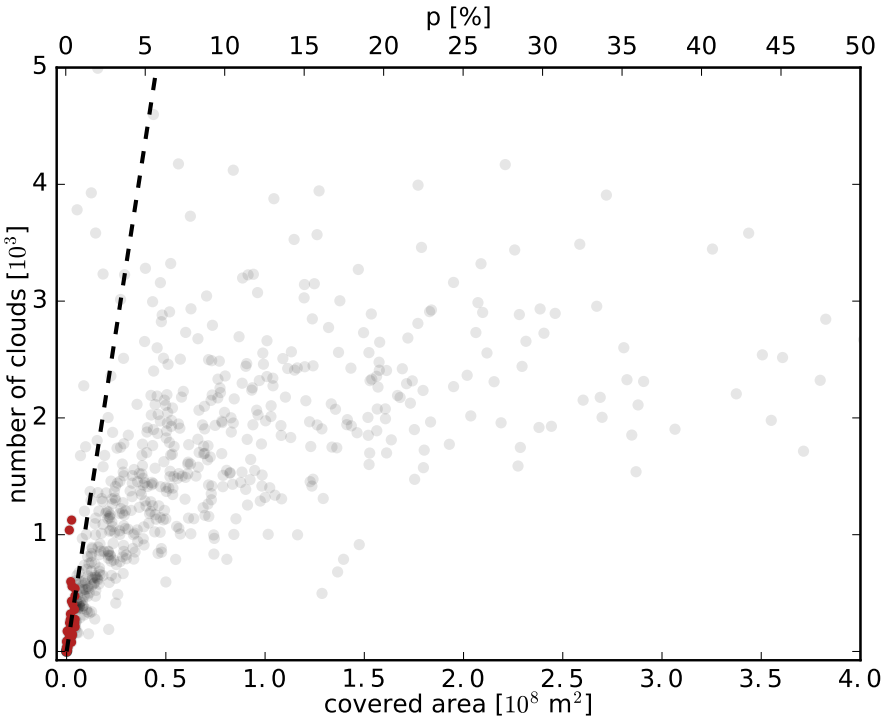

Fig. 2.4.: Number of clouds and area covered by the clouds for each satellite image (gray dots). Satellite scenes chosen for the linear fit (dashed line) to determine the average cell size are highlighted in red.

6% are shown in Fig. 2.5. Within a certain distance of the origin we find, for all scenes, that RDF(r) is significantly larger than one, indicating a clustering of cloud centers.

We now identify the parameter pair cw and cs that leads to the best correspondence with the satellite RDFs at small radii, where the sensitivity is largest. In addition to the satellite data, Fig. 2.5 shows the RDFs calculated from model output with $cw = 2.25$ and four different values for the clustering strength cs with the coverage fraction set to $p = 5\%$. The shape of the model and observed RDFs are qualitatively similar.

We find however that the RDF depends not only on the distance r but also on the cloud fraction. If, as assumed, the clustering parameters are local cloud properties that do not depend on total cloud fraction, the same values of cw and cs should apply to the entire data set. As we find that the RDF for $r < 200$ m is very sensitive to computation details, we compare satellite and model RDFs at $r = 265$ m to estimate our parameters (inset of Fig. 2.5). We find that $cs = 300$ provides a good fit across the range of cloud fractions. A more precise determination is impossible as we find only weak dependence of the RDF on cs, despite varying the cluster strength by almost one order of magnitude. A similar

analysis was performed for different values of cluster width cw, and values of $cs = 300$ and $cw = 2.25$ were found to give a reasonable approximation to the observed RDF for all scenes.

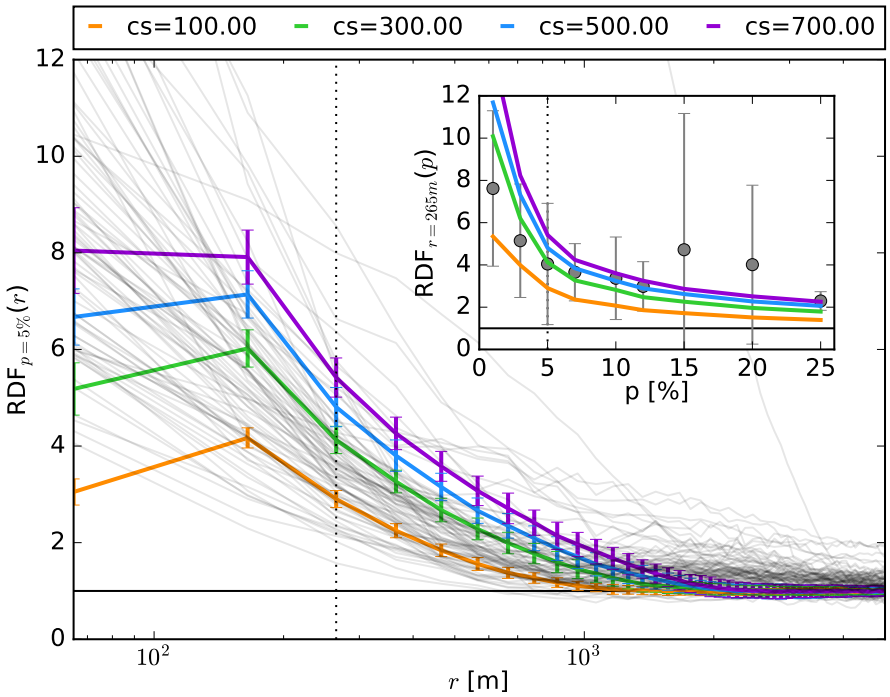

Fig. 2.5.: RDF of model output with four different clustering strengths and coverage fraction set to $p = 5\%$ (colored lines) is shown together with the RDF of all satellite scenes with coverage fraction in $4\% \leq p \leq 6\%$ (gray lines), the black line shows the uncorrelated limit. The inset shows a comparison of the RDF of the model (colored lines) and the mean and standard deviation of RDF of the satellite scenes (gray error-bars) at $r = 265$ m as a function of cloud coverage. The dotted lines indicate the value of the radius (percentage) at which the RDF is evaluated in the inset (main figure).

To summarize, the estimated values for the local model parameters are $s_m^d = 11.3 \times 10^3$ m^2, $cs = 300$ and $cw = 2.25$. The sensitivity of the results to variations of each parameter about its reference value is explored below. A qualitative impression of the cloud fields produced using the reference parameters can be seen from the example sub-region shown in the inset in Fig. 2.6.

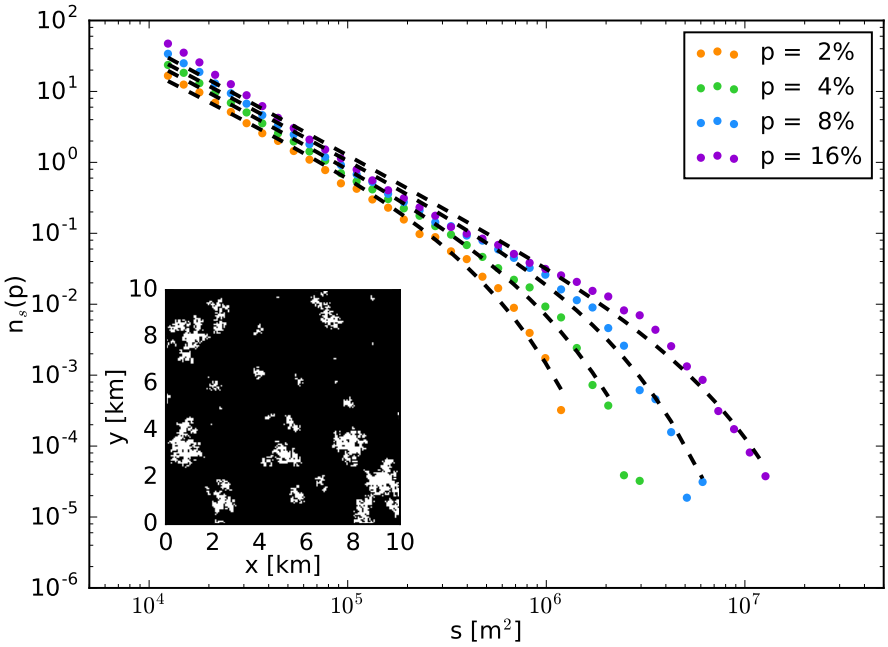

Fig. 2.6.: Cluster size distributions determined from modified subcritical percolation model for different coverage fractions (colored lines) and best fit curves following Eq. 2.3 (dashed black line). The inset shows a section of a sample model output.

2.3.3. Sensitivity to Cloud Fraction

For comparison with classical percolation and with satellite data we test the sensitivity of the size distributions of our model to cloud fraction. The comparison with observations will be confined to scales larger than the mean cell area of the exponential distribution since, even at large coverage fraction, smaller clouds are mainly single disks whose shape is not comparable with real clouds.

To determine cluster size distributions in our model, we simply determine the areas of the clusters formed by cloudy pixels. Sample cloud size distributions are shown in Fig. 2.6, which also shows the corresponding fit of Eq. 2.3. We find that the modified percolation model leads to cloud size distributions which, while still described by Eq. 2.3, now show a power-law scaling range for low cloud fractions in agreement with the observations. Close examination of the curves for the largest coverage fractions shows a slight excess of large clouds in comparison to the distribution given by Eq. 2.3. This deviation resembles the distributions produced in percolation systems of finite size (*Hoshen et al.*, 1979), and may result from the model approaching the percolation threshold only in local regions due to the induced clustering.

For a quantitative comparison of the model with observations, Fig. 2.3 shows the variation of

the three fitting parameters (a, b, c) with coverage fraction for the model- and the satellite size distributions. The model parameters s_m^d and cs are set to their reference values and results are shown for four different values of cw, including its reference value. While the largest differences occur for the smallest cloud fractions, which are more likely to be influenced by the details of the underlying exponential distribution of circular cells, the overall agreement between the reference model set-up and satellite parameters is good.

2.3.4. Sensitivity to local parameters

In the following we will briefly discuss the sensitivity to the clustering parameters and the cell size distribution.

Clustering Parameters

Changing either clustering width (Fig. 2.3) or clustering strength (Fig. 2.8) has an effect on the scaling properties comparable with an increase in coverage fraction as we find fewer but larger cloud clusters at a given overall cloud fraction. This similarity in the sensitivity of the two clustering parameters is consistent with the hypothesis that the induced clustering allows cloud merging to occur at smaller coverage fractions.

Cell size distribution

Size distributions for different average cell sizes can be seen in Fig. 2.7(a). Under the assumption that the horizontal resolution is small enough and the size of the domain is large enough not to influence the size distribution, the only relevant length scale is given by the mean radius of disks, r_m^d. The size distributions for different average cell sizes should therefore be rescalable by the corresponding area s_m^d. To rescale the size distributions for a given average cell size s_m^d to the size distribution of a reference average cell size $s_m^{d,ref}$, we need to rescale all areas s by a factor $f_{scale} = s_m^{d,ref}/s_m^d$. We therefore have to rescale the abscissa by f_{scale}. As the number of clusters of a given size s per area, i.e. the ordinate, is inversely depended on the area it also has to be rescaled by a factor f_{scale}^{-1}. The effect of rescaling the size distributions in Fig. 2.7(a) to $s_m^{d,ref} = 60\,\mathrm{m}$ is shown in Fig. 2.7(b) which confirms that the size distributions for different average cell sizes are identical apart from a scaling factor f_{scale}.

Testing the sensitivity of our results to the type of underlying size distribution, we repeat the comparison with observations performed above using uniform instead of exponential size distributions. We find the results to be qualitatively similar, but that the exponential distribution is required for quantitative agreement (not shown).

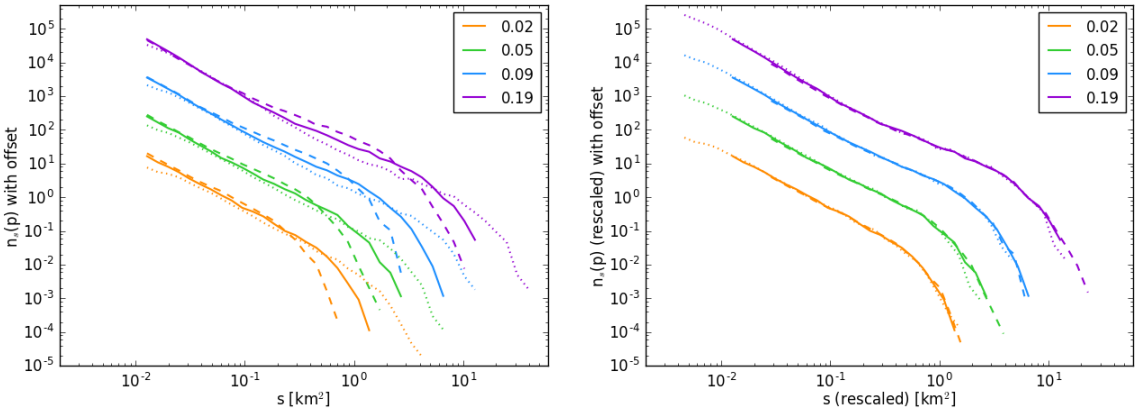

(a) (b)

Fig. 2.7.: Cluster size distribution calculated from the modified subcritical percolation model for different cloud fractions (different colors) with all parameters set to their reference values excepting the average cell size, for which three different values are tested: the dashed line shows $s_m^d = 0.50 \times 10^4\,\mathrm{m}^2$ ($r_m^d = 40\,\mathrm{m}$), the solid line shows the reference value $s_m^d = 1.13 \times 10^4\,\mathrm{m}^2$ ($r_m^d = 60\,\mathrm{m}$) and the dotted line shows $s_m^d = 3.14 \times 10^4\,\mathrm{m}^2$ ($r_m^d = 100\,\mathrm{m}$). The unmodified size distributions are shown in (a) and the corresponding rescaled size distributions to $r_m^d = 60\,\mathrm{m}$ are shown in (b). For better distinction, size distributions corresponding to different cloud fractions are shown with an offset.

2.4. Conclusions

In this chapter we have addressed the question whether the frequently observed power law scaling and scale break in size distributions of shallow cumulus clouds can be explained by subcritical percolation theory.

In section 2.2, we show that the sensitivity of the size distributions to cloud-fraction and the functional dependence is in agreement with results from subcritical percolation. With increasing cloud fraction, the power-law scaling region steepens and extends to larger clouds. In contrast to lattice percolation, power-law scaling is already apparent at lower cloud fractions than expected.

This difference is explained in section 2.3 by the clustering of cloud cells. Modifying the standard continuum percolation model by including a clustering tendency and an underlying exponential size distribution of cloud cells, we find that, for a given coverage fraction, the range of power law scaling increases with increasing clustering. Estimating the parameters of this model from the satellite data set results in accurate quantitative predictions of the power-law exponent and the position of the scale break.

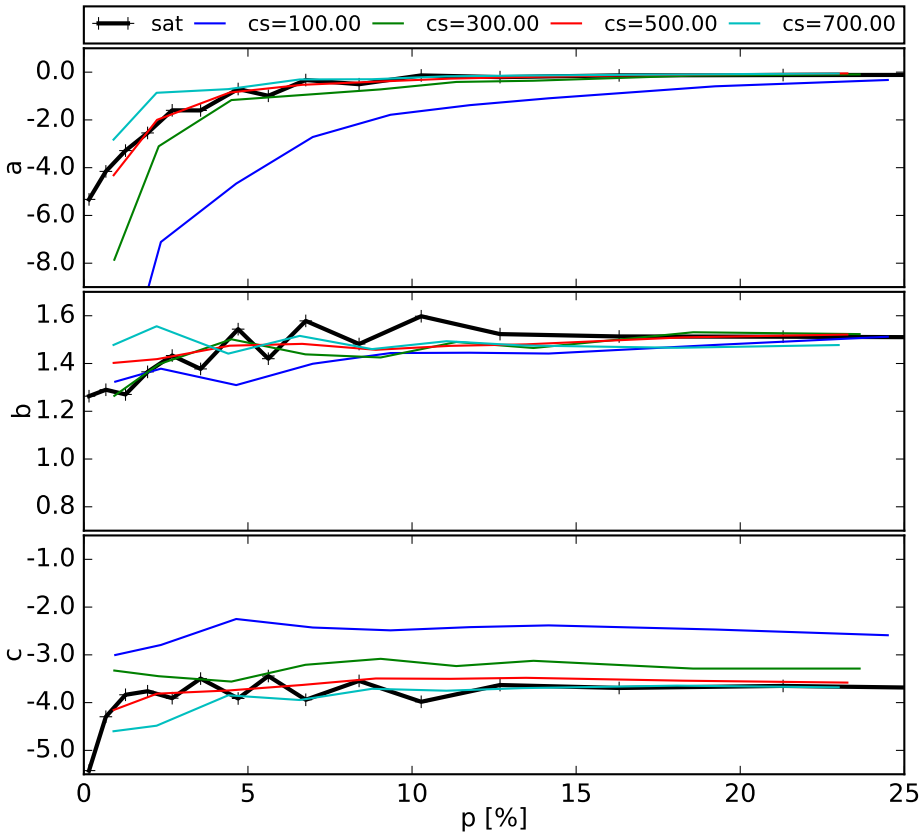

Fig. 2.8.: As in Fig. 2.3 but for varying cluster strengths.

While these results show the importance of the clustering tendency to the observed size distributions, we have not attempted to construct a detailed physical model for the clustering mechanism. Such a model has been proposed for example by *Böing* (2016), but the result is rather complex, and the details of the mechanism are unimportant for the resulting size distribution, as long as the observed cluster strength and width are reproduced.

The emergence of power law size distributions over a limited range of scales as a generic result of local clustering suggests that a similar process may occur for deep convection, where power laws are also seen in the size distribution of precipitation regions (*Peters et al.*, 2009). Indeed the appearance of a power law distribution of deep convective clouds emerging from an underlying exponential distribution has been seen in numerical simulations (*Scheufele*, 2014).

3. Spreading of convective activity

3.1. Introduction

While we focused on the local clustering of updrafts, caused by cold pools, in the previous chapter we will now explore how cold pools induce spreading of convective activity. In particular, we will introduce a lattice model, based on directed percolation, to reproduce the spreading of convective activity via cold pools and investigate its relation to the continuous phase transition in convective activity observed by *Peters and Neelin* (2006).

3.1.1. Cold Pool Triggering

Updrafts preferentially occur on top of cold pool boundaries as cold pool boundaries act as an important trigger for convection. The mechanisms by which cold pools can trigger convection have been discussed in section 1.4.2, where we have also discussed how the subsequent formation of convection and cold pools can lead to the spreading of convective activity (*Tompkins*, 2001b). We will now use a RCE simulation for a more detailed illustration of the space and time scales on which convection, via the expansion of cold pools, induces further convection. The simulation was conducted by *Scheufele* (2014) on a $128\,\mathrm{km} \times 128\,\mathrm{km}$ domain with a horizontal resolution of 250 m and a constant forcing of $-8\,\mathrm{K\,d^{-1}}$.

Figure 3.1 shows a snapshot of the boundary layer vertical velocity and temperature perturbations. To better distinguish the different features of interest, only a subsection of the domain is shown. Cold pools appear as regions of downdraft with negative temperature perturbations surrounded by narrow regions of positive vertical velocities. To show the position of convection in relation to the cold pool boundaries, regions of convective updrafts are superimposed on the fields.

In this chapter we define convective updrafts using the vertical velocity field in 2.4 km height. Using the standard velocity threshold for updraft cores of $1\,\mathrm{m\,s^{-1}}$ (e.g. *LeMone and Zipser*, 1980), velocities larger or equal than $1\,\mathrm{m\,s^{-1}}$ correspond to convecting sites and velocities smaller than $1\,\mathrm{m\,s^{-1}}$ to non-convecting sites.

The position of convective updrafts is, as expected, strongly linked to the cold pools. In particular we find that convection occurs either on top of the cold pool boundaries, as we

have seen for shallow cumulus clouds in the previous chapter or in the center of a newly forming small but intense cold pool as remnant of the cloud which originally caused the cold pool. An example of the first is shown by the ring of updrafts marked as A and for the latter by the cold pool marked by B.

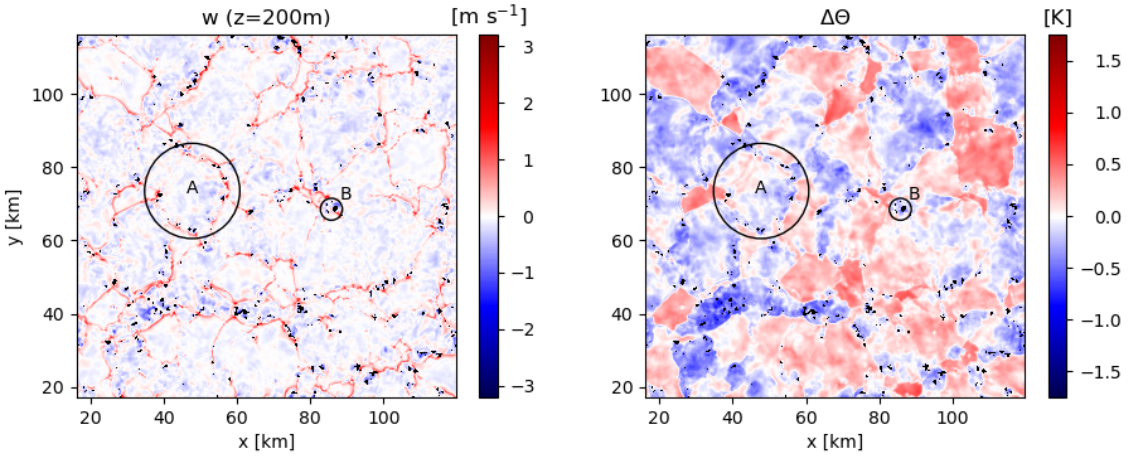

Fig. 3.1.: Subsection of vertical velocity in 200 m height (left) and boundary layer temperature perturbations (right) snapshots of RCE simulation performed by *Scheufele* (2014). Masked in black are regions with updrafts larger than $1\,\mathrm{m\,s^{-1}}$ in 2400 m height. A and B mark two cold pools discussed in the text.

To illustrate the ability of cold pools to trigger new convection as they expand, we now focus on convection forming during the expansion of cold pool B. Figure 3.2, shows snapshots of the temperature perturbation, the vertical velocity and the vertically integrated cloud water content, within a small region around cold pool B. For each field, five successive snapshots, separated by 30 min, are shown. Initially, the cold pool is marked by a region of strong downdraft and weak temperature perturbation, with the cloud which led to the formation of the cold pool still visible as updraft region and in the cloud water content. These signs of the initial convection disappear, while new clouds form on top the expanding cold pool boundary. This appears to be particularly strong after one and after one and a half hours, where updrafts and cloud water appear in a circular region around the cold pool center. After two hours, the temperature perturbation and the vertical velocity at the boundary weaken as do the fields indicating convection. In fact, we already see the development of a new cold pool forming due to convection previously triggered at the left boundary of the cold pool.

While the probability for new convection is enhanced at the cold pool boundary, we find that no convection is triggered within the cold downdraft regions.

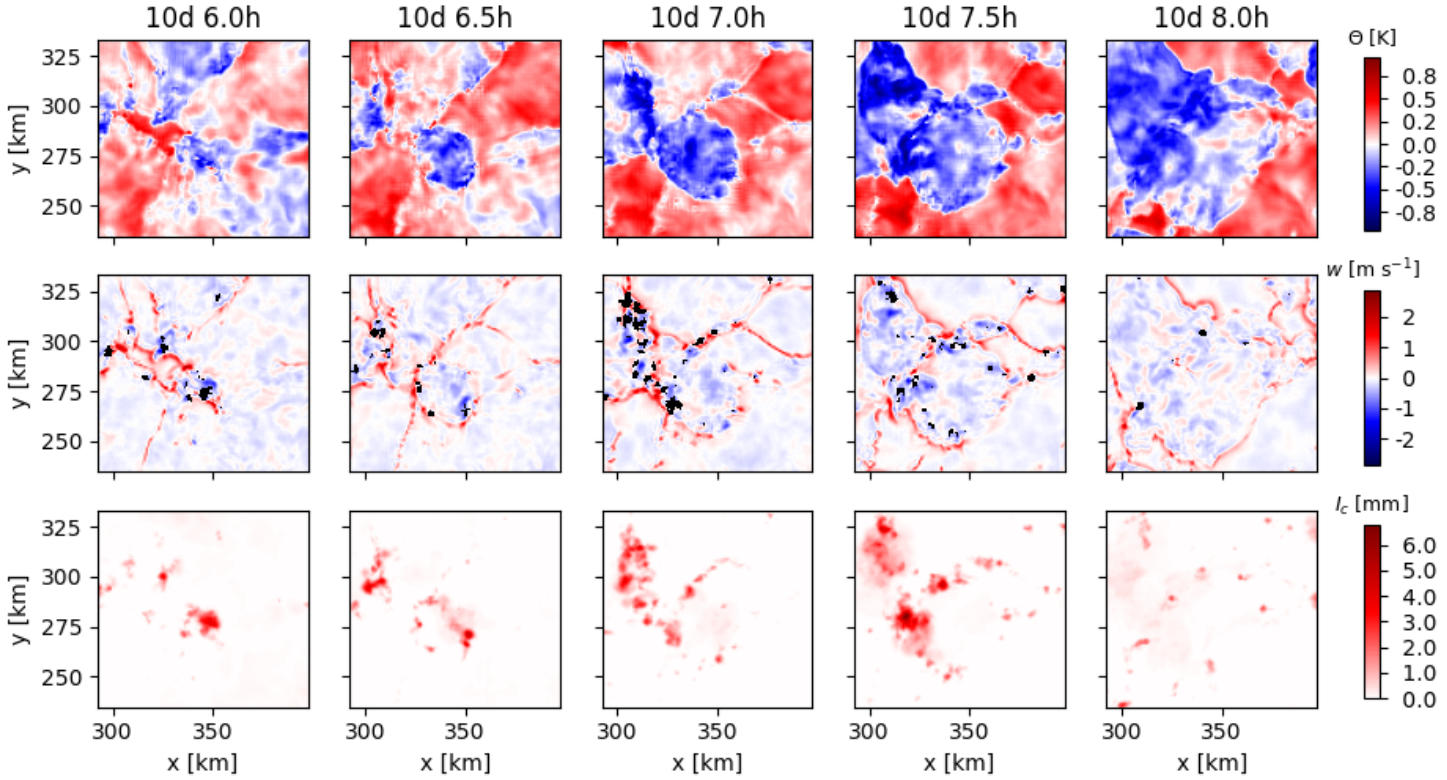

Fig. 3.2.: Successive snapshots of the boundary layer temperature perturbation (top row), the vertical velocity in 200 m height with updrafts larger than $1\,\mathrm{m\,s^{-1}}$ in 2400 m height masked in black (middle row) and the vertically integrated cloud water content (bottom row) within a small region around cold pool B. The first column corresponding to the time step shown in Fig. 3.1.

3.1.2. Continuous phase transition in convective activity

The process of convection triggering new convection via cold pools reviewed above has been investigated in a large number of studies. While most studies focus on the mechanism by which cold pools trigger new convection, we are here interested in how convective activity spreads from one generation to the next. In particular, we ask whether cold pool triggering can explain the continuous phase transition in convective activity observed by *Peters and Neelin* (2006).

Before we can introduce a model which explains how the dependence of convective activity on cold pool triggering can lead to a phase transition, we will need to review the results of *Peters and Neelin* (2006) and discuss their relation to known properties of non-equilibrium phase transitions.

We start in section 3.1.2.1 by describing how the ability of the atmosphere to self-organize to a critical state, as observed by *Peters and Neelin* (2006), is produced by the interaction of two independent processes:

1. a process whose dependence on the mean atmospheric state leads to a phase transition between a convectively active and a convectively inactive state
2. a process which drives the atmosphere into the critical state of the phase transition

Peters and Neelin (2006) themselves suggest that the atmosphere is driven towards the critical state by the combination of radiative forcing and compensating subsidence, in short by the mechanisms by which convection is driven or feeds back onto the mean atmospheric state.

As the two processes listed above need to be independent to result in self-organized criticality, we will discuss how convective activity depends on cold pool triggering in the absence of radiative forcing and compensating subsidence. We will moreover show how the assumption that convective activity depends entirely on previous convective activity suggests that the observed phase transition is in the universality class of directed percolation, whose key properties we introduce in section 3.1.2.2.

In section 3.1.2.4 we finally introduce a model based on the properties of cold pool triggering which describes the spreading of convective activity and belongs to the universality class of directed percolation.

3.1.2.1. Self-organized criticality in observations

Peters and Neelin (2006) were the first to suggest that the atmosphere is in a self-organized critical state. In particular, they suggest that the atmosphere self-tunes towards the critical point of an underlying continuous phase transition in convective activity.

As indications for the phase transition they show that convective activity, i.e. the order parameter, given in terms of precipitation P shows a power-law increase above a critical value of the column integrated water vapor, the control parameter, w_c:

$$P(w) \sim (w - w_c)^{\beta} \text{ with } \beta \approx 0.215. \tag{3.1}$$

In addition, they find a peak in variance of the precipitation strength at the critical value as well as long range spatial correlations, as expected for a continuous phase transition.

As they find that the atmospheric humidity content is predominantly close to the critical value w_c, they suggest that the critical state of the atmosphere is attractive. This can be explained by the so called absorbing state (AS) mechanism, illustrated in Fig. 3.3 (e.g. *Pruessner*, 2012). Instead of manually tuning the control parameter, in this case tropospheric humidity, to the critical value of the underlying phase transition, a coupling between the control and order parameter drives the control parameter close to the critical value, resulting in a delta distribution peaking at the critical value in the limit of an infinitely large domain size.

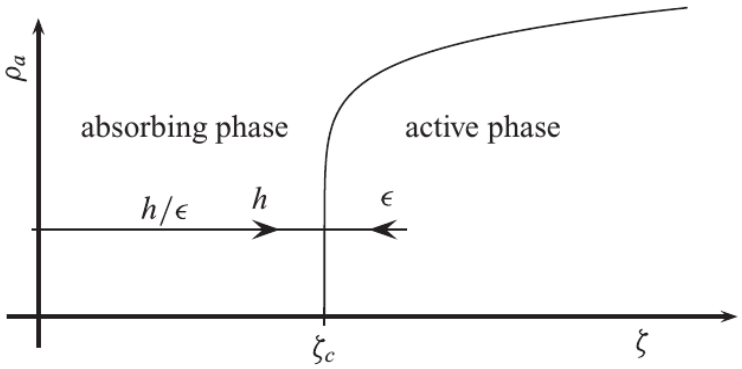

Fig. 3.3.: The order parameter ρ_a (activity) as a function of the control parameter ζ (particle density) in an AS transition. In the AS mechanism, the particle density is increased by the external driving, h, and reduced by dissipation, ϵ, (bold arrows). (*Pruessner*, 2012)

The control parameter is driven towards the critical point by two opposing processes. On the one hand, an external drive constantly increases the energy i.e. the control parameter of the system, while, on the other hand, energy is dissipated, the control parameter reduced, as long as the system is active which is equivalent to its being above the critical value.

The two corresponding processes in the atmosphere are radiative cooling, constantly driving the atmosphere into an increasingly unstable state, and latent heat release, quickly spread over large regions by gravity waves and stabilizing the atmosphere. For these processes to effectively pin the control parameter to its critical state, there has to be a clear time scale separation between the time scale on which activity spreads, i.e. the time scale on which convection triggers new convection, the time scale on which energy is dissipated and the

time scale on which energy is increased by the driving process. The necessary conditions can be expressed as a double limit on the driving h and the dissipating rate ϵ (*Dickman et al.*, 2000): $\epsilon \to 0$ and $h/\epsilon \to 0$. The double time scale separation ensures that the spreading of activity, and thus the size of the convective event, is not affected by dissipation and that the forcing acts slow compared to dissipation.

While the proposed physical processes driving the system towards the critical point are the same processes which lead to the quasi-equilibrium assumption, the underlying phase transition, i.e. the phase transition of convective activity in the absence of a feedback between convection and large scale forcing, has not been explained so far but "begs for a simple model of the atmospheric dynamics"(*Peters and Neelin*, 2006).

In this chapter we explore whether the underlying phase transition in convection can be explained in terms of cold pool induced spreading of convective activity. In particular, we suggest that the atmospheric state will not only determine the strength of convection and the resulting cold pool, it will also determine the average amount of new convection triggered by each convective cell. Depending on the mean state of the atmosphere, convection will either continue to spread or cease if the atmospheric state does or does not support the formation of enough new convection.

The subcritical phase in Fig. 3.3 contains only one state, namely the state without convection because we assume here that convective activity depends entirely on previous convective activity. The non-convecting state is the only state which cannot be left again if once entered into and thus corresponds to a single absorbing state in the parlance of non-equilibrium phase transitions. There is strong evidence in the literature that all non-equilibrium phase-transitions with a single absorbing state belong to the universality class of directed percolation (e.g. *Dickman et al.*, 2000) and we therefore expect from our hypothesis that the phase transition observed by *Peters and Neelin* (2006) is in the universality class of directed percolation.

3.1.2.2. Directed Percolation

As directed percolation will play an important role in this chapter, we here give a short summary of its key properties based on *Hinrichsen* (2006). In contrast to isotropic percolation[1], which we considered in the last chapter, directed percolation is a dynamical process where activity can spread to surrounding sites with time. The rules of directed percolation are illustrated in Fig. 3.4. As the name implies, directed percolation can only spread along a preferred direction, usually interpreted as time. In the setup shown in Fig. 3.4, one can think of directed percolation as water, percolating through a porous medium. At each time step,

[1]Note that we have so far omitted the word *isotropic* as percolation by itself generally refers to isotropic percolation.

activity (water) can spread to its two nearest neighbors in the preferred direction if the bond to this neighbor is open. The percolation probability p for a bond to be open is fixed.

Arguably the most important property of directed percolation is that it shows, at the critical percolation probability p_c, a continuous phase transition from a fluctuating into an absorbing, non-fluctuating state. Starting multiple experiments with an initially equal density of active sites but different percolation probabilities p, all activity eventually ceases in the case of $p < p_c$, the absorbing non-fluctuating state, while activity never dies for $p \geq p_c$, the fluctuating state. Note however that these results are only exactly true if the domain size and the experiment duration were infinite. In accordance with the properties of a continuous phase transition the spatial and temporal correlation length diverge at the critical point p_c and, which is most relevant for the discussion here, the density of active sites at $t = \infty$ picks up as a power-law according to

$$\rho_a(t = \infty) \sim (p - p_c)^\beta \tag{3.2}$$

with the universal critical exponent β. As there are virtually no analytic results for directed percolation, the critical exponents have been determined numerically with $\beta \approx 0.58$ in two dimensions (*Hinrichsen*, 2006).

While comparison of β with the exponent of the power-law pickup of precipitation in observations, $\beta \approx 0.215$, yields no agreement, we note that the exponent β strongly depends on the choice of order and control parameter. For example *Peters and Neelin* (2006) themselves find $\beta \approx 0.13$ when they use cloud water instead of precipitation as an indicator of convective activity.

We now address the question whether we can find a model in the directed percolation universality class which can reproduce the spreading of convective activity observed in atmospheric models.

3.1.2.3. Population model with global control

While we have argued that large scale forcing and compensating subsidence cannot explain the continuous phase transition but drive the atmosphere to the critical point, we will have to account for their effect when trying to reproduce convective spreading in a RCE simulation. In particular, while cold pools determine the position where new convection can be triggered, the amount of convection triggered during each time step should be approximately constant in the case of constant forcing.

Broeker and Grassberger (1999) introduce a control-switched version of directed percolation, a slightly modified version of a plant population model first introduced by *Wallinga* (1995). Given in terms of a lattice model, activity can only spread to nearest neighbors of active sites while the total number of active sites is kept constant with time.

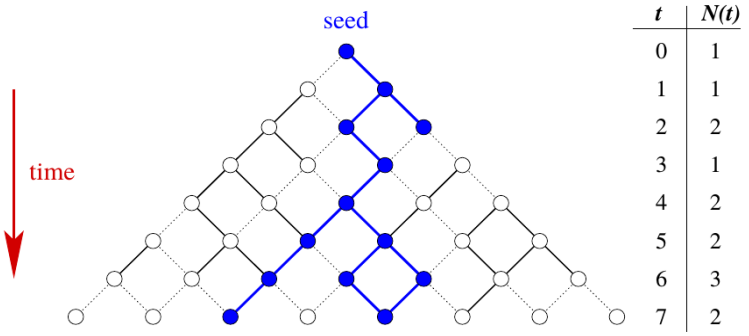

t	N(t)
0	1
1	1
2	2
3	1
4	2
5	2
6	3
7	2

Fig. 3.4.: Starting with a single active site at the origin, activity spreads at each time step from an active site to its two nearest neighbors in the preferred direction if the respective bonds are open. The preferred direction is here indicated by the time arrow and an open bond is represented by a solid rather than dotted connecting line. The probability for a bond to be open corresponds to the percolation probability p. The total number of active sites at any time t is given by $N(t)$ (Figure taken from *Hinrichsen*, 2006).

The model was originally designed to describe the dynamics and the spatial patterns emerging in a weed population. The underlying idea is that within a field, N_f weed plants grow. Each year, the plants drop seeds within their vicinity and die. In spring new plants grow in the surrounding of the old plants. Not all of these new plants are allowed to grow and distribute seeds however, the farmer of the field only tolerates exactly N_f weed plants and removes all excessive plants in a completely random fashion. They formalized this spreading mechanism of weed in terms of a population model on a two-dimensional square lattice of size L^2 with periodic boundary conditions and the following rules:

1. Initially N_f sites of the lattice are randomly chosen to contain a plant seed
2. At each time t_i all plants drop four seeds, one onto each of their four nearest neighbors, and die, while the number of sites which have received at least one seed, M, is strictly larger then N_f
3. The population size at t_{i+1} is kept constant by randomly choosing exactly N_f of the M sites to grow into a new plant or, equivalently, by randomly removing $M - N_f$ plants, with the fraction of surviving plants given by $\tilde{p} = N_f/M$

The reason for calling this model a control-switched version of directed percolation can best be explained with regard to Eq. 3.2: instead of varying the percolation probability p and estimating the density of active sites $\rho_a(t = \infty)$, *Broeker and Grassberger* (1999) fix the density of active sites (the new control parameter) and determine the fraction of surviving plants (the new order parameter). The fraction of surviving plants corresponds to the percolation probability as it gives the ratio of the number of sites where activity has been triggered and the number of sites where activity could have been triggered.

They show that, at least in one and two dimensions, the fraction of surviving plants $\tilde{p}(t) = N_f/M(t)$ self-adjusts to

$$\langle \tilde{p} \rangle - p_c \sim \rho_a^{\frac{1}{\beta}} \tag{3.3}$$

in the limit of large domain sizes and small population densities, with $\tilde{p}(t = \infty) \to p_c$ in the case $\rho_a \to 0$.

They claim that this is an instance of self-organized criticality. While critical behavior in directed percolation is only observed close to p_c, critical behavior in the population model is found in the limit of large populations and low densities, i.e. without tuning the population density to a critical point.

3.1.2.4. Cold Pool Model

We now propose a simple model for describing the propagation of convective activity. The model is based on the population model with global control but has an additional inhibition state to account for cold pool recovery.

Comparison of the population model with the picture of cold pool induced spreading of convective activity we reviewed at the beginning of this chapter leads to the following analogy. An active site, i.e. a plant site, corresponds to deep convection and the effect of cold pools triggering convection at their boundary corresponds to the distribution of seeds onto the neighboring grid-cells. The large scale forcing, which determines the amount of convection, corresponds to the farmer and the probability $\tilde{p}$ is a measure of the ability of the cold pool to trigger new convection.

As cold pools spread however, they not only trigger convection at their boundaries but also suppress further convection within. To also account for this effect, we include an inhibition state. In particular, the inhibition state prevents the formation of new active sites at a site which has been active within the last time steps. Note, that we do not expect that the introduction of an inhibition state will affect the universal properties of the model as directed percolation is remarkably robust to changes in the local interaction rules. It has in fact been shown by *de Souza and Tomé* (2010) and *Cruz et al.* (2012) that introducing an inhibition state in the contact process, another model belonging to the directed percolation universality class, does not affect the universal properties.

To include the effect of cold pool recovery we change the rules of the original population model in the following three points:

- Old clouds turn to inhibition sites, not neutral sites
- New convection can only form on neutral sites
- Cold pools turn back to neutral sites with fixed probability $1/\tau_{lt}$ [2]

[2] This corresponds to an exponential distribution of cold pool lifetimes with an expected value of τ_{lf}.

As in the modified version of the model each site is in one of three (inhibited, neutral, active) instead of one of two (neutral, active) possible states, we will refer to the new model as three-state and the original model as two-state model.

We will test whether including an inhibition state improves the model's ability of representing the spreading of convective activity in the RCE simulation by comparison with the two state model.

3.1.3. Outline

The outline of the chapter is as follows. In section 3.2 we introduce two methods to evaluate the spreading of convective activity in an atmospheric model and in the simple model. Applying these methods to the RCE simulation introduced in section 3.1.1 enables us to estimate the necessary parameters and compare the two- and three-state model to the atmospheric model simulation. In section 3.4, we propose a test for the hypothesis of an absorbing state phase transition in convective activity using an atmospheric model simulation.

3.2. Method

In order to determine the parameters necessary for the lattice model and to quantify the spreading of convective activity to compare the RCE simulation with the lattice model we introduce two methods. The first method allows us to determine whether new convection preferentially forms at cold pool boundaries. While the second method does not relate newly triggered convection to cold pools, it is a more objective method for determining the spreading of convective activity.

3.2.1. Cold pool diagnostic

For the lattice model introduced above, we need to estimate the grid length, the model time step and the average lifetime of the inhibition state τ_{lt}. We determine the length of the grid cell from the typical spacing between the position of the old convective cell and the cell triggered in the next generation and the model time step from the respective temporal separation. For τ_{lt}, we estimate the time it takes the cold pool induced perturbations to recover.

To determine how much convection is triggered by the expanding cold pool as a function of time and cold pool size, we now introduce a diagnostic which allows us to determine the amount of updraft close to the cold pool boundary as a function of time. The diagnostic involves two steps:

1. determine the position of the cold pool boundary
2. determine the position of the convection forming in the surrounding of the cold pool center

Comparison allows us to verify that convection is primarily triggered close to the cold pool boundary and to determine when most of the new convection is triggered.

To determine the mean position of the cold pool boundary as a function of time we calculate a radially integrated statistic of a set of cold pools. To this end we determine the cold pool center by eye, calculate the mean radial dependence of the temperature perturbation field and then average over all cold pools. The position of the cold pool boundary is then defined as the position of sign change in the temperature perturbation. Note that we need to take care that the initial extent of the chosen cold pools is comparable.

Having determined the position of the cold pool boundary as a function of time, we then determine the amount of convection triggered in the surrounding of the cold pool center as a function of time and distance and relate it to the position of the cold pool boundary. As before, we use a binary field to indicate the presence of convection, with updraft vertical velocities in 2.4 km height larger or equal than $1\,\mathrm{m\,s^{-1}}$ corresponding to convecting sites and below to non-convecting sites. Assuming that the cold pool spreads isotropically from the cold pool center, we calculate the radially averaged amount of convection for each time-step. We thus obtain the amount of convection as a function of time after the cold pool is detected and the distance to the cold pool center. Comparison with the position of the cold pool boundary allows us to assess on what time and spatial scales new convection is triggered by the propagating boundary.

3.2.2. Cross-Correlation Function

In addition to the method based on manually chosen cold pools introduced above we will also use a more objective method to investigate how convective activity propagates within the domain using normalized cross-correlation functions. If the reader is familiar with cross-correlation functions, this section can be skipped.

Cross-correlation functions indicate the similarity between two fields as a function of the relative displacement of the two fields. The two fields we use here are two subsequent scalar fields $f(t;\vec{x})$ and $f(t+\Delta t;\vec{x})$, separated by a time difference Δt. The corresponding two dimensional cross-correlation function is defined as follows:

$$C_{t+\Delta t,t}(\vec{x}) = \int \mathrm{d}\vec{x}' \frac{(f(t+\Delta t;\vec{x}') - \langle f(t+\Delta t)\rangle)(f(t;\vec{x}'+\vec{x}) - \langle f(t)\rangle)}{\sigma(f(t+\Delta t))\sigma(f(t))} \tag{3.4}$$

where $\langle\cdot\rangle$ is the domain mean and $\sigma(\cdot)$ the standard deviation.

Assuming again that there is no preferred direction in which convection is triggered, we focus our attention on the radially averaged cross correlation function:

$$C_{t+\Delta t,t}(r) = \frac{\int_\Gamma C \mathrm{d}l}{2\pi r} \tag{3.5}$$

where Γ corresponds to a circular path with radius r and center at the origin and dl is the corresponding line element.

To illustrate how this method applies to a field of clouds, i.e. isolated features, we compute the cross-correlation function for an artificial setup. The "convection" field at time t has a single cloud at the origin of the domain, modeled by a narrow Gaussian distribution. Each time-step Δt, the cloud moves five grid-cells in x-direction, see Fig. 3.5a). In addition to the position of the cloud centers, Fig. 3.5 shows the corresponding cross-correlation functions of the initial field with the field at each of the three subsequent time-steps. In particular, Fig. 3.5b) shows the cross-correlation function calculated only in x-direction. It shows that there is a perfect correlation of the initial field and the propagated field at the relative distance by which the cloud center was shifted. The x values corresponding to the maxima indicate the distance the field has moved in this direction. This is still true after radial integration, though the signal weakens with increasing distance to the cloud center. As we average a single cloud over a region which increases proportionally to r, we find a decrease in the correlation function by r^{-1}. Performing the same test with a field containing many clouds

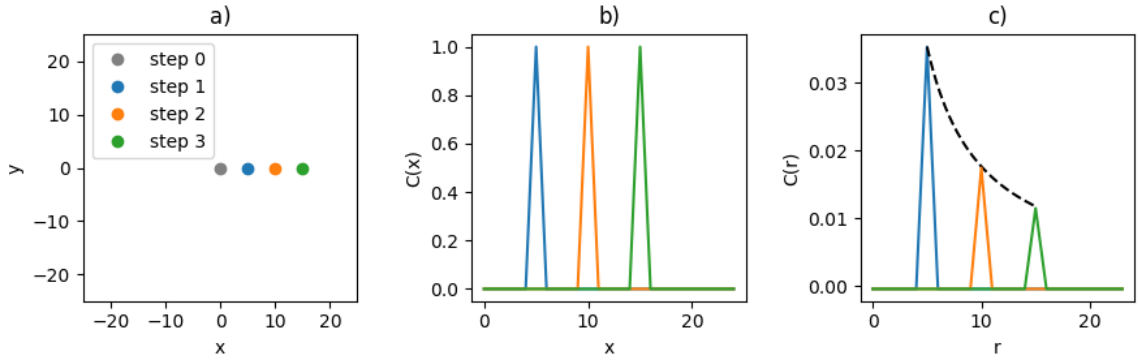

Fig. 3.5.: Position of the cloud center at the different time-steps (a) and the Cross-Correlation function of the following fields with the initial field along x-axis (b) and radially integrated (c). The radially integrated Cross-Correlation functions show in addition a r^{-1} decrease (dashed line).

shows that the maximum correlation is still at the distance by which the field was shifted though correlations with other clouds in the domain make the dependency more noisy (not shown). This shows that we can extract the displacement of features per time-step from the cross-correlation function.

To determine the spreading of convective activity, we calculate the cross-correlation function of cloud fields, again defined by vertical velocities larger or equal than $1\,\mathrm{m\,s^{-1}}$. Note that we use the velocity rather than e.g. humidity field due its smaller persistence in time.

3.3. Results

3.3.1. Cold pool diagnostic applied to RCE Simulation

We now apply the cold pool diagnostic introduced in 3.2.1 to ten visually chosen cold pools in the RCE simulation performed by *Scheufele* (2014).

The mean, radially integrated temperature perturbation, from which we determine the cold pool boundary as a function of time, is shown in Fig. 3.6, where t_d denotes the time at which the cold pool was first detected. The initial negative temperature perturbation systematically extends in space and weakens with time.

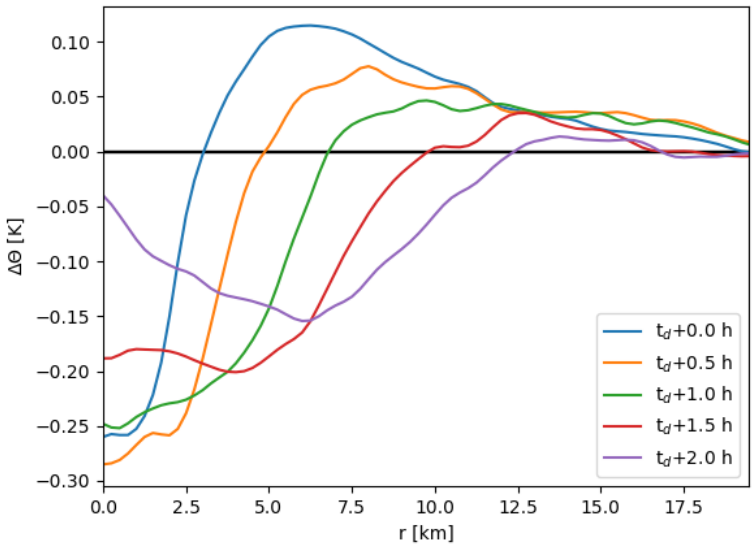

Fig. 3.6.: Mean radial dependence of potential temperature in cold pools with different colors corresponding to different times after detection.

The position of the cold pool boundary, determined from the position of sign change in the temperature perturbation, is given in the following table as a function of time.

$t - t_d$ [h]	0.0	0.5	1.0	1.5	2.0
r_{cp} [km]	2.75	4.75	6.5	9.75	12.25

A corresponding linear fit (not shown) gives a mean cold pool size at t_d of 2.4 km and a propagation speed of $4.8 \pm 0.3\ \mathrm{km\,h^{-1}}$. Extrapolation suggests that we detect the cold pools approximately half an hour after their formation. We note that the thus determined propagation speed is comparable though slightly faster than the $4\ \mathrm{km\,h^{-1}}$ which can be estimated from Fig. 9 in *Tompkins* (2001b), where the cold pool radius expands approximately linearly from 2 km to 10 km in two hours.

We can now compare the position of the cold pool boundary to the amount and position of newly triggered convection. Figure 3.7 shows the radially averaged amount of convection as a function of the distance to the cold pool center (abscissa) for subsequent time steps (ordinate). To determine whether the newly forming updrafts are related to the expanding cold pool boundaries, we use the mean velocity and radius of the cold pool boundary at t_d, determined above, to indicate the position of the cold pool boundary as a function of time. While the initial updraft persists for about half an hour close to the cold pool center we see clear indications that the cold pool boundary is at the leading edge of the majority of the newly forming updrafts. In particular, the position of the cold pool boundary marks the edge of the region of increased probability for updrafts within the following time-steps. The probability of new updrafts is particularly increased up to a distance of about 10 km from the cold pool center and within the first two hours after cold pool detection. While there is a local maximum after about one hour and at a distance of about 5 km, its significance is doubtful due to the small sample size.

In addition to the region of increased updraft probability, we also note that once the initial updraft dissolves, convection is suppressed for about four hours. This suggests that in the here investigated RCE simulation, cold pools influence the triggering of new convection in two ways:

- the probability of triggering new convection is increased at the cold pool boundary
- the probability of triggering new convection is decreased within the cold pool

which agrees well with previous studies and our assumptions for the simple model.

Apart from the increased likelihood of new convection along the cold pool boundary within the first two hours, there is an additional region of increased probability close to the cold pool boundary after about two or three hours. This signal might indicate a second generation of clouds triggered by the first generation.

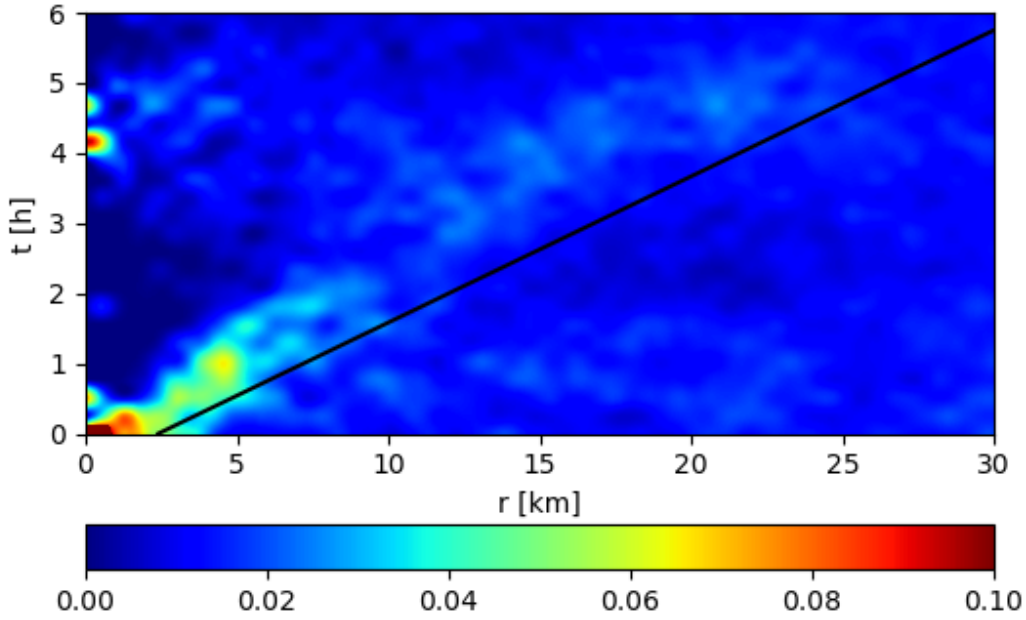

Fig. 3.7.: Radially averaged amount of convection (see text for more details) in 2.4 km height as a function of distance to the cold pool center and time passed after the detection of the cold pool (colors) and the position of the cold pool boundary (line).

3.3.2. Cross-correlation diagnostic applied to RCE simulation

In the following we determine the cross-correlation functions of the cloud fields calculated in the RCE simulation by *Scheufele* (2014). Figure 3.8 shows the cross-correlation function averaged over all possible starting times at day ten of the simulation. While Fig. 3.8(a) shows the cross-correlation function for different time lags allowing to easily identify the position of the maxima, Fig. 3.8(b) shows a filled contour plot of the cross-correlation function as a function of distance and time lag to ease comparison with Fig. 3.7. As the cross-correlation function is always equal to one at the origin but quickly drops to significantly smaller values we truncate the colorbar.

We find that initially the cross-correlation function rapidly decreases at the origin before it starts to recover, while the position of the maximum is shifted to increasingly large distances.

Taking the distance between two subsequent maxima in Fig. 3.8(a), gives an estimate of how far convection has spread within one time-step. We use this to calculate a propagation speed of convective activity:

time [h]	0.5	1.0	1.5	2.0	2.5
position of maximum [km]	1.00	4.75	7.25	9.50	11.75

Using a linear fit gives an average propagation speed of $5.3 \pm 0.3\ \mathrm{km\,h^{-1}}$. This compares well with the cold pool propagation speed we estimated above.

In accordance with triggering of new clouds at an expanding cold pool boundary, the maximum in the cross-correlation function propagates away from the origin with a speed similar to the one estimated for the propagation of the cold pool boundary. Though the local maximum observed in Fig. 3.7 is no longer discernible, suggesting it to be noise resulting from our small set of cold pools, we again find that the probability for the formation of new convection is increased at the cold pool boundary within the first two hours and up to a distance of about 10 km. In addition, the anti-correlation close to the origin again indicates a local suppression of new convection inside the cold pools for about four hours.

We use these results together with the results from the cold pool diagnostic to determine the necessary parameters for the simple model. In particular, we set the characteristic time and length scale at which convection triggers new convection, corresponding to time step and length of grid cell in the simple model, to half the time and distance at which the signal of increased probability disappears, i.e. $\mathrm{d}x = 5$ km and $\mathrm{d}t = 1$ h. The average life-time of the inhibition state is given by the average time new convection is suppressed inside the cold pool and therefore $\tau_{lf} = 4\,\mathrm{h}$.

We find, as in Fig. 3.7 but more pronounced, a second region of increased probability at about 15 km and 3 h potentially indicating a second generation of triggered clouds.

Repeating the analysis above for different setups we find similar behavior to what has been shown. In particular, *Scheufele* (2014) performed a number of RCE simulations with different horizontal resolutions, ranging from 250 m up to 2 km, and different forcing, ranging from $-2\,\mathrm{K\,d^{-1}}$ up to $-12\,\mathrm{K\,d^{-1}}$. The dependence of the propagation velocity on time, resolution and forcing is shown in Fig. 3.9. Note that we can show only the hourly average of the propagation speed as we have no higher temporal output for some of the simulation setups.

As long as the horizontal resolution is high enough to represent the relevant processes, a change in resolution should not affect the spreading of convective activity. While Fig. 3.9(a) shows little difference between resolutions of 0.25 km, 0.5 km and 1 km, which consistently give values of about $5\,\mathrm{km\,h^{-1}}$, the 2 km simulation shows, at least initially, much higher propagation speeds. It is interesting to note that *Scheufele* (2014) also found a distinctly different spatial distribution of convective updrafts for the 2 km simulation in comparison with the higher resolution simulations. This indicates that the 2 km resolution simulation cannot resolve the relevant cold pool processes correctly, at least during the early stages of the cold pool lifetime.

In accordance with *Craig and Cohen* (2006) and *Cohen and Craig* (2006), *Scheufele* (2014)

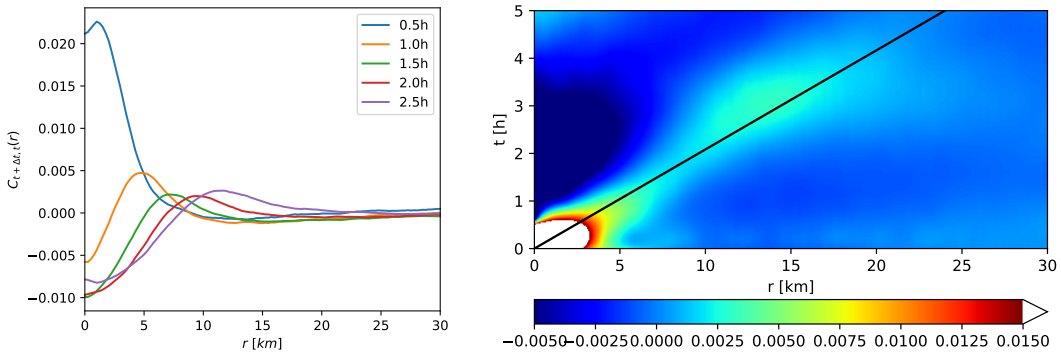

(a) (b)

Fig. 3.8.: (a) Radially averaged cross-correlation function of cloud fields for different time lags (colors). (b) Radially averaged cross-Correlation function of cloud fields as a function of distance (x-axis) and time lag (y-axis) (colors). The position of the cold pool boundary at each time is indicated by the black line.

showed that the forcing mainly affects the density not the intensity of the individual convective clouds. We therefore expect that the ability of the individual clouds to trigger new clouds remains the same. This agrees with Fig. 3.9(b) which shows that there is no clear dependence of the propagation velocity on the forcing. Note that we have excluded the results of the simulation with 2 km resolution as they take, at least initially, very distinct values from the other resolutions.

3.3.3. Minimal model

Applying the parameters determined above, we will now compare the properties of the two- and the three-state model to the observed spreading of activity in the RCE simulation. In particular, we set the length of the grid-cells to 5 km, the time-step to $1\,\mathrm{h}$ and, in case of the three state model, the cold pool life time to $4\,\mathrm{h}$. Thus, if convection in the middle of one grid-cell triggers convection in the middle of the neighboring grid-cell, their centers are separated by 5 km, which corresponds to the characteristic distance determined above, and the formation of new convection is suppressed within the area covered by the cold pool for the four following time steps.

3.3.3.1. Snapshots

Randomly chosen snapshots of the two- and three-state models are shown in Fig. 3.10. For better comparison with the RCE simulation, the snapshots show, in addition to the cold pools

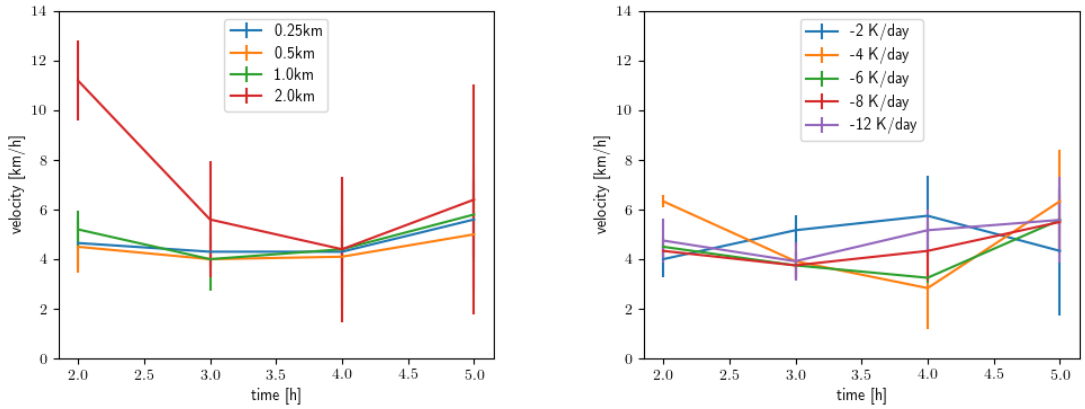

(a) (b)

Fig. 3.9.: Average velocity and corresponding standard deviation depending on time, where (a) shows the dependence on the horizontal resolution while averaging over the different forcings and (b) explicitly shows the dependence on the forcing while averaging over the resolution (excluding the 2 km resolution results).

represented by the grid cells, regions of updrafts within the cold pools. Note that the updrafts themselves do not influence the time-evolution of the models and are merely used to facilitate the comparison with the diagnostics used for the updraft regions above. From the correlation length of the initial updraft, as seen for example in Fig. 3.7 for t =0.5 h, we approximate the size of the updraft as about one third of the length of a grid-cell. As we find in Fig. 3.1 that the updrafts are not always in the center of the downdraft, we divide each cold pool grid cell into three by three sub cells and randomly place an updraft site at one of them. The coverage fraction is chosen such that 1% of the domain is covered by updrafts, which corresponds to the mean coverage fraction found in the RCE simulation above.

As in the RCE simulations we find clustering of convection, though with significantly smaller number of updrafts. This, however, is not surprising as our model is intended to represent conglomerations of updrafts rather than individual updrafts.

3.3.3.2. Cross-correlation diagnostic

We now compare the spatial evolution of the convection field in the RCE simulation to the two and three state population model. In particular, we assess whether the lattice models can reproduce the spreading of convection as seen in the cross-correlation functions above, Fig. 3.8. The cross-correlation functions of the two- and the three-state population model are shown in Fig. 3.11 and in Fig. 3.12 respectively.

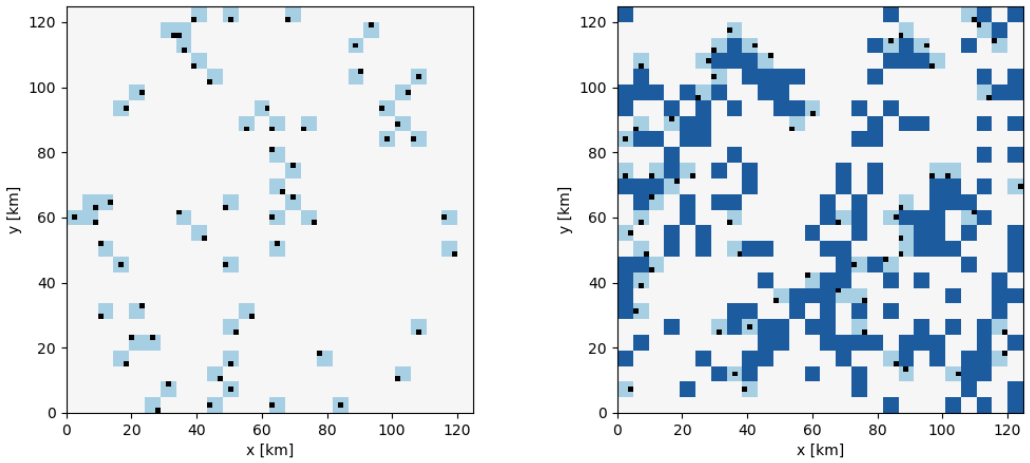

(a) (b)

Fig. 3.10.: Snapshots of the two-state model (a) and three-state model (b). The active cold pool sites shown in light blue, the non-active sites in white and the updrafts as black. The inhibition state in the three-state model is shown in dark blue colors.

Comparison with the RCE results highlights the importance of the third inhibition state for reproducing the observed spreading. While the three state model is able to approximately reproduce the spreading properties observed in section 3.3.1, the two state model shows a strong back and forth oscillation of convective activity. The oscillatory behavior of the two state model can be seen very clearly in Fig. 3.11(b), where the propagation towards successively larger distances is almost imperceptible compared to the back and forth oscillation between the cold pool center and convection at a distance of one grid-length. In contrast, convection moves away from the initial convection with a velocity of approximately one grid cell per time step, i.e. $5\,\mathrm{km\,h^{-1}}$, in the three state model, see Fig. 3.12, with suppression of new convection close to the updraft center which starts relaxing towards the uncorrelated state after about 5 h. Different to the results above however, the new maxima are not very distinct and the quantization of the lattice is clearly visible in the sharp peaks.

These findings show that the minimal model can qualitatively reproduce the spreading of convective activity observed in RCE simulations. In view of the previously introduced lattice models by *Majda and Khouider* (2002), *Khouider et al.* (2010), *Bengtsson et al.* (2011) and *Dorrestijn et al.* (2013), it is interesting to note that we need a set of at least three states to represent the spatial spreading convection.

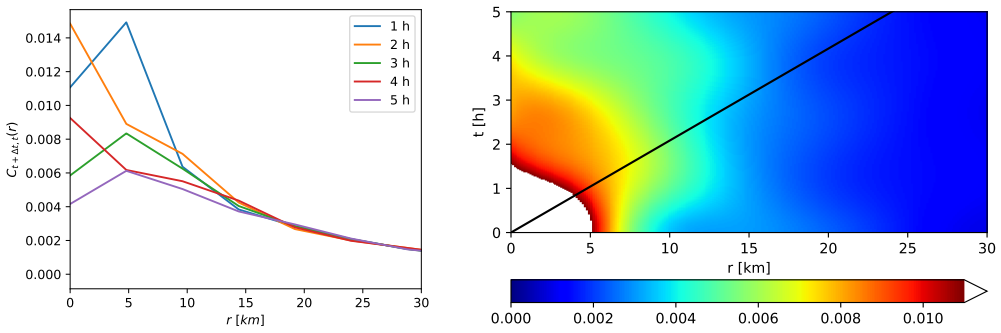

(a) (b)

Fig. 3.11.: As in Fig. 3.8 but calculated for the updraft sites in the two state population model.

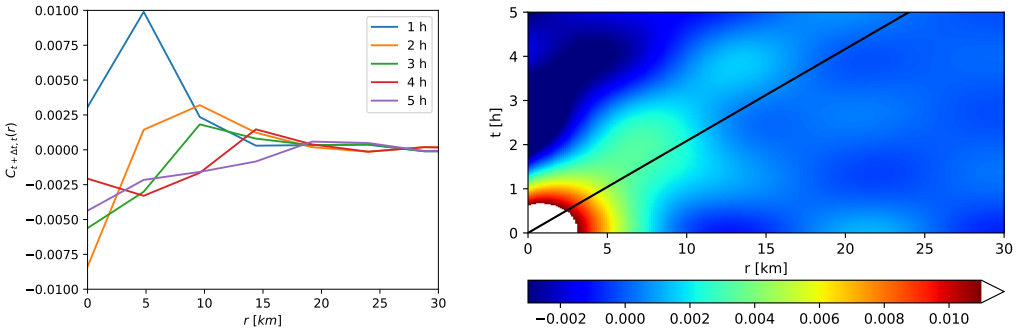

(a) (b)

Fig. 3.12.: As in Fig. 3.8 but calculated for the updraft sites in the three state population model.

3.4. Discussion

In this chapter we have suggested a relation between the spreading of convective activity via cold pools and the continuous phase transition of deep convection, observed by *Peters and Neelin* (2006). We first introduced a 2D lattice model which, based on cold pool triggering of convection, has an underlying continuous phase transition and leads to self-organized criticality as observed by *Peters and Neelin* (2006). In the lattice model, the ability of convection to trigger new convection at the boundary of the expanding cold pools is represented by active sites which, during each time step, can cause nearest neighboring sites to become active likewise. After triggering activity at neighboring sites, the initially active sites turn, for a number of time-steps, into inhibition sites to represent the local suppression of the formation of new convection within a region covered by cold pools. To also account for the quasi-equilibrium state of the atmosphere, where the amount of convection is determined by the large scale forcing, the total number of active sites is fixed. Without the global constraint on the number of active sites, the model would, at a critical triggering probability, exhibit a continuous phase-transition, belonging to the directed percolation universality class. Including the global constraint, the model shows, in the low density limit, self-organized criticality (*Broeker and Grassberger*, 1999).

Our hypothesis is therefore that the underlying phase transition is caused by cold pool triggering while self-organized criticality results from the atmosphere being driven to the critical point by the large scale forcing and compensating subsidence. As a first test for our hypothesis, we have compared the spreading of activity in the lattice model with spreading of convection in an atmospheric model. To this end, we have used a cloud-resolving model simulation performed by *Scheufele* (2014) to quantify the spreading of convection and also to estimate the relevant model parameters. Setting the parameters of the idealized model to the thus determined values, we find that the model can approximately reproduce the observed spreading of convective activity.

We will now discuss how, using an atmospheric model, one could investigate the underlying phase transition in convective activity explicitly though its realization is beyond the scope of this thesis. It is in fact the driving towards the critical point, caused by the coupling of convective activity and the atmospheric state, which hinders us from directly accessing the phase transition. We therefore propose to decouple the atmosphere from the mechanisms which, supposedly, drive it to the critical point by turning off the driving and the dissipating mechanisms (h and ϵ in Fig. 3.3). Starting from a state which already contains convection, by first using a standard RCE setup and running it into equilibrium, further destabilizing of the system can be removed by turning off radiative cooling. Removing the stabilizing effect of convection is more difficult as we need to be careful not to affect the formation and spreading of convection itself. The principle mechanism by which convection stabilizes the atmosphere is latent heat release spread via gravity waves which induce subsidence warming. Following the key idea of the weak-temperature gradient simulation, this feedback on the atmosphere is

replaced by a relaxation to the mean temperature sounding, obtained by the initial radiative-convective equilibrium simulation. The choice of the relaxation time scale is important as it will have to be long compared to the timescale of triggering new convection but faster than the stabilizing effect.

Before we can probe convective activity for the phase transition, we still need to define a control parameter. While *Peters and Neelin* (2006) used column integrated humidity, the vertical profile of humidity is known to play an important role. In particular, we expect cold pools to be mostly affected by low tropospheric humidity, which affects the available potential energy and thus the strength of the updrafts and also the amount of reevaporation and thus the strength of the resulting downdrafts.

Once the control parameter is defined and dissipation and driving is turned off, convective activity can be determined as a function of the control parameter. For a continuous phase transition we expect that convection eventually dies out below a critical value of the control parameter and shows a power-law increase of the order parameter above the critical value.

While the simple model above was introduced to explain the continuous phase transition observed by *Peters and Neelin* (2006), we note that the resulting model is in itself an important result as it may be useful for improving convection parameterizations. In particular, most current convection parameterizations do not account for the effect of temporal and spatial interactions on the variability of convective mass flux. While, as reviewed in the introduction of this thesis, lattice models have already been introduced by *Majda and Khouider* (2002), *Bengtsson et al.* (2011), and *Dorrestijn et al.* (2013) to remedy the lack of local interactions and memory their interaction rules were either defined in an ad hoc manner (*Majda and Khouider*, 2002; *Bengtsson et al.*, 2011) or determined numerically (*Dorrestijn et al.*, 2013). In contrast, we have here introduced a model with physically motivated transition rules, derived the necessary properties from a RCE simulation and shown its ability to reproduce the observed temporal and spatial correlations. We will give a more detailed outline of how one could include the model introduced above into a parameterization scheme in chapter 5.

4. Spatial Evolution of self-aggregation

4.1. Introduction

So far we have considered spatial and temporal correlations resulting from cold pool induced boundary layer perturbations. Now, we turn to self-aggregation (SA) of convection and its relation to the convectively induced humidity perturbations (see section 1.4.3). While we have seen in the previous chapter that cold pools induce correlations between individual clouds on length scales of a few kilometers and time scales of a few hours, the humidity perturbations associated with self-aggregation grow upscale on time scales much longer than the individual cloud or cold pool life time. In particular, most cloud resolving radiative equilibrium simulations take weeks before an approximately steady state with a single moist region (diameter on the order of 100 km) is reached.

Even though the relevant feedback mechanism, whose determination has been the key goal of most related studies, has been shown to depend on the chosen model, the chosen setup and the stage of self-aggregation, the spatial evolution of self-aggregation is always described by an upscale growth of moist and dry regions. In this chapter, we will focus on this universality in the spatial evolution of self-aggregation which has been largely overlooked so far. In particular, we here suggest that self-aggregation is described by a pattern-formation mechanism called coarsening, which is insensitive to the details of the feedback mechanism as long as they lead to an intensification of local humidity perturbations.

4.1.1. Spatial evolution of self-aggregation in RCE simulations

Even though humidity perturbations in self-aggregation are invariably described by an upscale growth, the shape of the emerging moist and dry regions has been found to depend on the shape of the domain. In particular, self-aggregation in small or channel-like domains leads to the formation of moist and dry bands, spanning, in the channel-like domains, the shorter horizontal direction while the characteristic appearance of self-aggregation in larger square domains, is the formation of a circular shaped moist region.

The formation of a moist band was first observed by *Tompkins and Craig* (1998). In order to correctly resolve three dimensional effects, they were the first to perform a three dimensional RCE simulation though computational constraints limited them to a small square domain with a horizontal size of $100\,\mathrm{km} \times 100\,\mathrm{km}$. After about four days, a slowly propagating moist band develops which spans the domain with an angle of about 45%. All convective activity is limited to this domain of high water vapor content.

Tompkins (2001b) was the first to use a channel-like domain, which extended $1024\,\mathrm{km}$ in the one but only $64\,\mathrm{km}$ in the other horizontal direction. Within five days, the domain again self-organized into stripes of convectively active moist and subsiding dry bands. Owing to increased computational possibilities, *Posselt et al.* (2012) could increase the length of the domain size of *Tompkins* (2001b) by almost one order of magnitude. As before, convection organized itself within few days into stripes which merged and intensified with time. Using a comparable though even more elongated domain setup, *Wing and Cronin* (2016) find self-aggregation very similar to *Posselt et al.* (2012).

Self-aggregation leading to the formation of a single, circular shaped moist region, was first described by *Bretherton et al.* (2005), who performed a RCE simulation on a domain with a horizontal area of $576\,\mathrm{km} \times 576\,\mathrm{km}$. After an initial period of randomly distributed convection, the domain separated into dry, subsiding regions and moist, precipitating regions which grew in time until, by day 50, only one moist region remained. The self-aggregation of the column integrated water vapor path (WVP) can be seen in Fig. 4.1 with the corresponding precipitation fields shown in Fig. 1.4. This simulation has become the benchmark study for SA in three dimensional cloud-resolving RCE simulations.

Using setups similar to the one described by *Bretherton et al.* (2005), self-aggregation into a single circular convecting region has been found in the studies conducted by *Khairoutdinov and Emanuel* (2010), *Muller and Held* (2012), *Wing and Emanuel* (2014), *Muller and Bony* (2015), *Holloway and Woolnough* (2016) and *Hohenegger and Stevens* (2016).

Some deviations to the spatial evolution described above have however been noted by *Wing and Emanuel* (2014) and *Holloway and Woolnough* (2016). *Wing and Emanuel* (2014) found that the shape of the moist region varied between simulations with different sea-surface temperature but otherwise identical setup. Despite a large square domain, they observed that for some sea-surface temperatures self-aggregation led to the formation of persistent moist bands rather than circular regions. The moist regions observed by *Holloway and Woolnough* (2016) were, while not band-like, less circular than in previous studies.

The formation of large dry subsiding and moist convectively active regions has also been observed in studies with general circulation models in a RCE setup but with parameterized convection (*Popke et al.*, 2013; *Coppin and Bony*, 2015). With the domain size given by the earth's surface, multiple moist regions form, some of which reach the size of continents. While the moist regions in the study conducted by *Popke et al.* (2013) are more or less circular, *Coppin and Bony* (2015) note that their moist regions have long filaments extending into

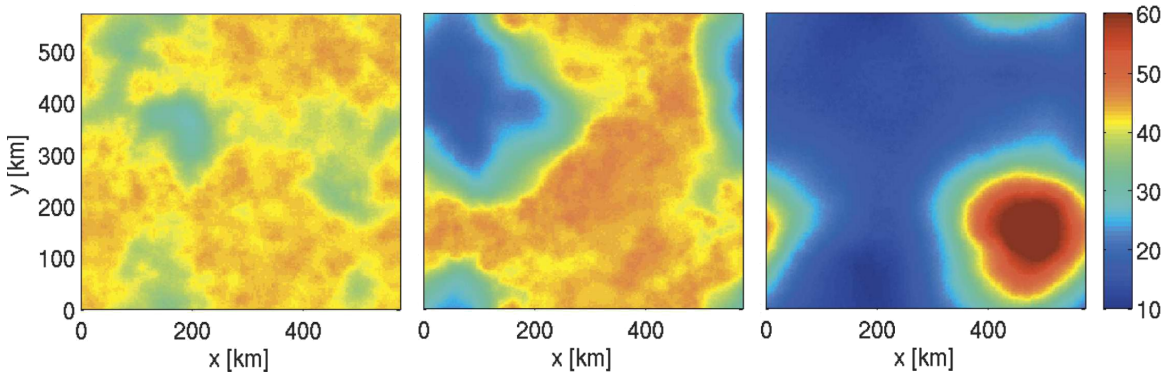

Fig. 4.1.: Daily mean water vapor path [mm] in a cloud resolving model at day 10, day 20 and day 50 (left to right) (*Bretherton et al.*, 2005).

the dry regions. This appearance of moist filaments is somewhat comparable to the moist region in *Holloway and Woolnough* (2016), mentioned above. It is interesting to speculate whether these filaments are caused by the formation of significant circulations within the domain. As we will discuss in more detail below, low level circulations have been found to lead to upgradient horizontal transport during later stages of self-aggregation. This process may perhaps lead to the formation of elongated moist regions, which indicate the convergence zone of lateral humidity transport.

While the spatial appearance of self-aggregation has thus been found to depend on the shape of the domain, with band-like moist regions for channel-like simulations and circular moist regions in square or global domains, self-aggregation has in addition been shown to only occur in large domains. Apart from the early study by *Tompkins and Craig* (1998), all subsequent studies find self-aggregation is limited to domains which are larger than 200 or 300 km in at least one horizontal direction. In particular, *Bretherton et al.* (2005) tested a small set of (square) domain sizes and found that self-aggregation occurred for 384 km (or above) but not for 288 km (or below). Repeating this sensitivity study with a larger set of domain sizes, *Muller and Held* (2012) found that self-aggregation only occurred for domains larger than about 200 km. Again testing different domain sizes for their tendency of self-aggregation, *Jeevanjee and Romps* (2013) find self-aggregation only above approximately 300 km.

4.1.2. Proposed mechanisms causing self-aggregation

Many studies have explored the potential feedback mechanisms leading to self-aggregation. The arising picture is complicated and it has been shown that in most cases multiple feedbacks act at the same time. Note that while the feedbacks are usually described by their

effect on humidity, rather than convection, humidity perturbations and convective aggregation occur together as convection is limited to moist regions.

Three physical mechanisms causing a feedback have been identified: surface fluxes, radiation and convection itself. Each of these feedbacks can be either positive, i.e. leading to an increase of humidity in already moist regions, or negative and thus remove perturbations in the humidity field. Self-aggregation thus depends on the sum of positive feedbacks being larger then the sum of negative feedbacks. In the following we shortly describe how the processes listed above affect the local humidity distribution. For a more detailed review see *Wing et al.* (2017).

Surface fluxes

It has been suggested that surface fluxes can be a positive or a negative feedback. On the one hand, the positive feedback is due to the increased surface winds, and therefore increased surface fluxes, in convectively active regions. Surface winds are affected by the presence of convection as the onset of convection is connected with low-level convergence while the decay of convection is associated with cold pools and thus low-level divergence. On the other hand, the negative feedback is due to the decrease in the latent heat flux if the boundary layer is anomalously moist.

While earlier studies suggest that a positive surface flux feedback is necessary for self-aggregation (*Tompkins and Craig*, 1998; *Bretherton et al.*, 2005), more recent studies find that surface fluxes act as a positive but not necessary feedback (*Muller and Held*, 2012; *Holloway and Woolnough*, 2016).

Radiation

As we have discussed in section 1.1.1, radiation can interact with convection and humidity perturbations in a number of ways. As shortwave and longwave radiative interactions with clouds and humidity are quite distinct, we describe them separately.

The relevant question for the longwave radiative feedback is whether dry columns emit more or less longwave radiation than moist columns. In particular, if longwave emission is increased this leads to radiative cooling, which by virtue of the weak temperature gradient approximation will induce subsidence drying. Longwave radiation therefore leads to a positive feedback if emission is increased in dry while decreased in moist regions. This feedback has been found to be very sensitive as the amount of emitted longwave radiation is strongly influenced not only by the amount of humidity in an air column but by the vertical profile of the humidity distribution and the presence of clouds. Analysis of the budget equation of the variability of the moist static energy, a diagnostic introduced by *Wing and Emanuel*

(2014) to assess the contribution of the different mechanisms to self-aggregation, suggests that longwave radiation feedbacks are important positive feedbacks at least during the early stages of self-aggregation (*Wing and Emanuel*, 2014; *Holloway and Woolnough*, 2016).

For shortwave radiation, the relevant question is how much of the incoming shortwave radiation is absorbed in the respective columns. If absorption is reduced, this again leads to cooling and thus subsidence drying. As for surface fluxes, the feedback has been found to be either positive or negative. On the one hand, dry regions are optically thinner then other regions which leads to reduced absorption and thus cooling. On the other hand, much of the incoming shortwave radiation in the moist regions can be reflected at cloud tops thus also inducing a cooling. While this latter effect has been shown to be important in particular in the aggregated state, comparison with the longwave feedback suggests that shortwave feedbacks are positive throughout but generally weaker then the longwave feedbacks (*Wing and Emanuel*, 2014; *Holloway and Woolnough*, 2016).

Convective entrainment and detrainment

Up to now, the introduced feedbacks discuss the effect on humidity rather than convection, with the idea that increased humidity will lead to increased convection. The entrainment-detrainment feedback however argues that not only does humidity increase the amount of convection but that in turn the convection induced humidity perturbations lead to a significant increases in humidity. As discussed in more detail in the introduction (section 1.4), convection transports humidity out of the boundary layer into the free troposphere, while some of it falls out as precipitation, the rest remains in the free troposphere. As surface fluxes quickly remoisten the boundary layer, this leads to a net increase in column humidity. While the increase in humidity due to convection is thus caused by detrainment, the dependence of convection is due to entrainment, as entraining of dry air will reduce the buoyancy and thus suppress the formation of deep convection.

Models for local humidity feedback

Three studies have introduced simplified models to describe a single or a combination of these feedbacks on the local humidity content: *Bretherton et al.* (2005), *Craig and Mack* (2013) and *Emanuel et al.* (2014). Despite describing different feedback mechanisms, they all suggest that the local humidity content is unstable: dry perturbations want to dry while moist perturbations want to moisten. While we will discuss these models in detail in section 4.2, we will argue in section 4.4 that the spatial structure of self-aggregation is independent of the model details.

4.1.3. Spatial interaction

Besides the feedbacks reviewed above, which act locally and thus contain no information about how humidity is exchanged within the domain, the formation of connected moist and dry regions from an initially randomly disturbed field shows that such an exchange takes place. To understand the spatial evolution of self-aggregation one therefore needs to assess how humidity is exchanged between different model columns.

Bretherton et al. (2005) were the first to suggest that horizontal humidity exchange is due to an upgradient transport of humidity, caused by a shallow circulation. *Muller and Held* (2012) showed that this circulation is mainly driven by longwave cooling at low level cloud tops in the dry region. The strong cooling induces strong subsidence which induces divergence at the surface and convergence at the cloud top height. It has been shown that this circulation leads to a net humidity export out of dry regions, thus strengthening anomalies in the humidity distribution. Analysis of the budget equation of the variability of the moist static energy (*Wing and Emanuel*, 2014; *Coppin and Bony*, 2015; *Holloway and Woolnough*, 2016) suggests however that the upgradient transport of humidity is not important during the initial phase of self-aggregation.

To describe the spatial evolution during the onset of self-aggregation we therefore need to introduce a spatial interaction term which accounts for moisture exchange with neighboring grid cells. In this study we propose that the spatial interaction, at least during the early stages of self-aggregation, is diffusive. A diffusive interaction term models random advection and leads to a downgradient moisture transport. We will show in this chapter that it approximately represents the effect of moisture increase due to stochastically triggered convection. This choice is in agreement with the initially negative contribution of the convergence term found by *Wing and Emanuel* (2014) and *Coppin and Bony* (2015) but not with with the neutral or even positive convergence term observed by *Holloway and Woolnough* (2016).

4.1.4. Coarsening

Assuming that the atmosphere is in a bistable state, i.e. depending on initial humidity content each grid cell wants to become either moist or dry, what time evolution do we expect in a spatially extended system? In case of diffusive spatial interaction, the time evolution equation belongs to a specific type of Reaction-Diffusion Equation: the Time-Dependent Ginzburg-Landau Equation (TDGL), sometimes also called Allen-Cahn Equation. Starting from a slightly perturbed homogeneous field in the unstable state, the TDGL equation describes the time evolution of a phase separation by a process called *coarsening*. A short summary of this process, based on the respective chapters in *Sethna* (2006), *Henkel and Pleimling* (2010) and *Krapivsky et al.* (2010), is given in the following.

The general form of a Reaction-Diffusion equations of a scalar field q is given by

$$\frac{\partial q}{\partial t} = R(q) + D\nabla^2 q \tag{4.1}$$

where $R(q)$ accounts for all local interactions which affect q and D is the diffusion coefficient. In TDGL equations, the local interactions can be represented as the functional derivative of a double-well potential $V(q)$

$$\frac{\partial q}{\partial t} = -\frac{\delta V}{\delta q} + D\nabla^2 q. \tag{4.2}$$

The double-well potential accounts for the bistability of the system with respect to q as without the diffusive term, i.e. without spatial interaction, every site of the domain would relax into one of the two potential minima, depending on its initial value of q. The two potential minima thus correspond to the two stable states.

Starting from a field in the unstable state (the maximum of the potential) with added random noise, will first lead to the formation of small, coherent regions of the two stable phases, followed by an upscale growth. An example of which is shown in Fig. 4.2 for the Ising model, first introduced to describe ferromagnetism and the classic example of a model showing coarsening.

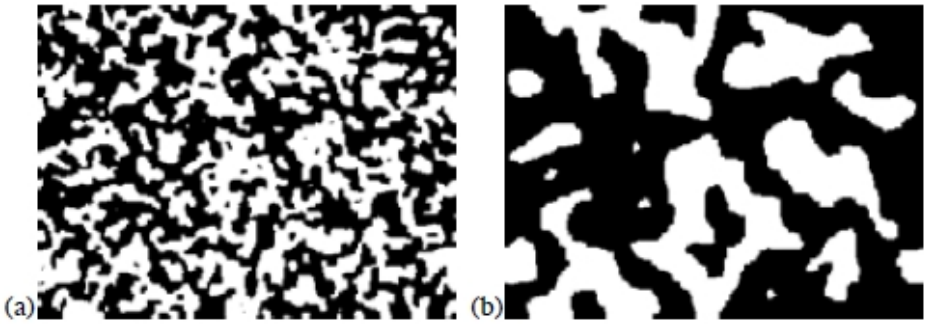

Fig. 4.2.: Spin configuration of an Ising-model at zero temperature after a) 20 time steps and b) 200 time steps (*Sethna*, 2006, p. 247).

The key property of TDGL equations is the self-similarity of the upscale growth of the stable regions. This means that the morphology is (statistically) time-independent, apart from a rescaling of all length scales according to

$$L(t) \sim t^{1/2}. \tag{4.3}$$

The dynamical exponent of $1/2$ is universal for all non-conserved scalar order parameters. In particular, it is independent of details of the potential and, unlike the critical exponents

discussed in the context of continuous phase transitions, of the considered dimension d if $d \geq 2$.

The time evolution described by the TDGL is purely dissipative, minimizing the Landau Free Energy

$$F[q(\vec{x})] = \int [\frac{1}{2}(\nabla q(\vec{x}))^2 + V(q(\vec{x}))] d\vec{x}. \tag{4.4}$$

In order to minimize Eq. 4.4, the domain will eventually contain only three distinct regions: regions in the two stable phases (black and white) and domain walls between them. While the functional dependence of the barrier width depends on the details of the considered potential, some properties which apply to all potentials are summarized in the following.

Starting with the one-dimensional case and a potential with two degenerate minima at q_1 and q_2, it has been shown (e.g. *Krapivsky et al.*, 2010) that the domain wall evolves towards a functional dependence given by

$$x = \sqrt{\frac{D}{2}} \int_{q(-\infty)}^{q(x)} \frac{dq}{\sqrt{V(q)}}. \tag{4.5}$$

Solving Eq. 4.5 for $q(x)$, given the potential $V(q)$, gives the humidity profile of a single barrier between a dry ($q(-\infty) = q_1$) and a moist region ($q(\infty) = q_2$). As the distance between two given humidity values, according to Eq. 4.5, scales with the square root of the diffusion coefficient, this implies in that the barrier width, defined as the distance over which $q_1 + \Delta q$ increases to $q_2 - \Delta q$ with Δq small, is proportional to $\sqrt{D}$. See the Appendix A for further details.

Extending their argument to a potential with two non-degenerate minima, say $V(q_1) < V(q_2)$, we argue in part A of the Appendix that this relation for the barrier width still holds but that now the stable region (q_1) will in addition propagate into the metastable region (q_2).

4.2. Three Local Feedback Models

In this chapter we suggest that the type of pattern formation observed during self-aggregation of convection is independent of the details of the positive feedback, as long as this feedback acts locally. In order to illustrate this we start by comparing the three theoretical models introduced by *Bretherton et al.* (2005), *Craig and Mack* (2013) and *Emanuel et al.* (2014). Each model describes the time evolution of a local humidity perturbation, resulting from a single or a combination of feedback mechanisms and thus corresponds to $R(q)$ in a Reaction-Diffusion model, see Eq. 4.1.

4.2.1. Model introduced by *Bretherton et al.* (2005)

Bretherton et al. (2005) use a RCE simulation to derive a semi-empirical model for the time evolution of the column relative humidity r^{hum}. They start by deriving an approximate budget equation for the column relative humidity from the budget equation of the vertically integrated frozen moist static energy, using the weak-temperature gradient approximation. They find that the time evolution depends on radiation, surface fluxes and moisture convergence. To determine these component forcings, they fit the dependence of each of the forcing terms on precipitation rate P. They motivate using precipitation rather than column relative humidity by stating that, on physical grounds, they anticipate it to be the amount of convection which alters the forcing terms.

They find that the radiation as well as the surface flux forcing increase linearly with precipitation rate, suggesting that in regions of increased convection the relative humidity will increase due to both radiation and surface fluxes. The dependence of the convergence term on precipitation is more difficult but shows that convergence will transport humidity out of regions with little convection.

To obtain a closed equation for the time evolution of a humidity perturbation (their Eq. 9)

$$\partial_t r^{hum} = [c_s + c_r - \alpha_h(r^{hum} - r_h^{hum})][P(r^{hum}) - P_{RCE}]/W_* \tag{4.6}$$

they also use the dependence of the precipitation rate on humidity (their Eq. 2)

$$P(r^{hum}) = P_{RCE}(\exp(a_m(r^{hum} - r_{RCE}^{hum})) - 1), \tag{4.7}$$

where c_s, c_r, α_h, r_h^{hum} and a_m are fit parameters for the forcing terms, P_{RCE} is the horizontal mean radiative-convective equilibrium rain rate, r_{RCE}^{hum} the corresponding column relative humidity and W_* is the saturation water-vapor-path. .

All parameters were estimated by *Bretherton et al.* (2005) using their RCE simulation:

	c_s	c_r	α_h	r_h^{hum}	P_{RCE}	W_*	r_{RCE}^{hum}	a_m
Value	0.12	0.17	1.8	0.62	3.5	57	0.72	16.6
Unit	1	1	1	1	mm day^{-1}	mm	1	1

Combining Eq. 4.6 with Eq. 4.7 and replacing $r^{hum} - r_{RCE}^{hum}$ by $r^{hum'}$ yields the following interaction term:

$$R_B(r^{hum'}) = (c_s + c_r - \alpha_h(r^{hum'} - r_h^{hum} + r_{RCE}^{hum}))P_{RCE}(\exp(a_m r^{hum'}) - 1)/W_* \tag{4.8}$$

Note that while R in Eq. 4.1 only represents local interactions, Eq. 4.8 includes the non-local effect of the horizontal convergence term. As the diagnostic they use to derive this

convergence term is based on a diagnostic in "humidity space" rather than physical space its interpretation in form of a spatially extended circulation is not possible. We here include this term but note that strong spatial circulations would modify the spatial evolution equation.

4.2.2. Model introduced by *Craig and Mack* (2013)

The model introduced by *Craig and Mack* (2013) is based on a positive feedback between convection and the humidity content of the free troposphere. On the one hand, convection will increase the humidity in the free troposphere by transporting humidity out of the boundary layer into the free troposphere. While on the other hand, deep convection is more likely to occur in moist regions then in dry regions, as the entrainment of dry air reduces the buoyancy. They formalized this local feedback on the humidity content as:

$$R_C(I_v/I_v^*) = -\alpha I_v/I_v^* + \frac{\lambda}{I_v^*}(e^{b_m I_v/I_v^*} - 1)\left(\frac{I_v^*}{\beta_p I_v} - 1\right) \tag{4.9}$$

where I_v is vertically integrated free tropospheric moisture content and I_v^* is the corresponding saturation value. The first term on the right hand side of Eq. 4.9, represents the *subsidence drying term* which accounts for the loss of humidity due to subsidence, with subsidence rate α. The second term is the *convective moistening term* and represents the increase in humidity due to convection, where $\lambda(\exp(bI_v/I_v^*) - 1)$ gives the amount of precipitation for a given value of (I_v/I_v^*), see Eq. 4.7, and $(1/(\beta_p I_v/I_v^*) - 1)$ is the complement of the precipitation efficiency and gives the amount of humidity that does not drop out as precipitation. The parameters λ, b_m and β_p are fit parameters.

These parameters are estimated from RCE simulations, described in *Kempf* (2014), by fitting the subsidence drying and the convective moistening term (see *Kempf* (2014) for details on how these terms were extracted) for a sea surface temperature (SST) of 300 K at day 60, see Fig. 4.3. Note that we use the results from *Bretherton et al.* (2005) as first guess values for fitting the convective moistening part. In addition to the fit, which gives only a value for the fraction of λ/I_v^*, we extract the mean saturation water vapor content $I_v^* = 29.6\,\mathrm{kg\,m^{-2}}$ from the simulation, which allows us to estimate λ separately. Finally, we estimate the homogeneous humidity content in the RCE state, I_v^{RCE}, using $R_C(I_v^{RCE}/I_v^*) = 0$ which yields $I_v^{RCE} = 12.6\,\mathrm{kg\,m^{-2}}$

For comparability with the other models we ignore the global constraint, introduced in *Craig and Mack* (2013) to ensure that the domain can neither become completely dry nor completely moist, as is the case for an RCE simulation. Dropping this constraint corresponds to simulating only a small sub-region of an area in RCE, which allows a uniform dry or moist state, as observed for weak-temperature gradient simulations (e.g. *Sessions et al.*, 2010).

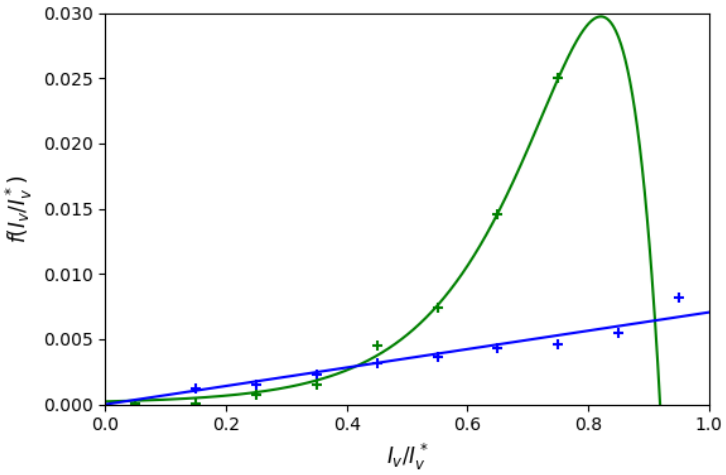

Fig. 4.3.: Absolute values of the subsidence drying (blue) and convective moistening (green) terms as a function of vertically integrated free tropospheric humidity content determined by *Kempf* (2014) (markers) with corresponding fit (solid lines).

	α	β_p	λ	b_m	I_v^*	I_v^{RCE}
Value	$2.0 \cdot 10^{-6}$	1.1	$1.7 \cdot 10^{-7}$	11.4	29.6	12.6
Unit	s^{-1}	1	$\mathrm{kg\,m^{-2}\,s^{-1}}$	1	$\mathrm{kg\,m^{-2}}$	$\mathrm{kg\,m^{-2}}$

4.2.3. Model introduced by *Emanuel et al.* (2014)

Emanuel et al. (2014) derive a time-evolution equation for humidity perturbations by linearizing the budget equation of moist static energy around the radiative-convective equilibrium state. Changes in the moist static energy are caused by radiative heating, convective transport and advection. By determining how each of these processes depends on the humidity content and then linearizing it, *Emanuel et al.* (2014) show that, at least for high SST, the combined effect of these processes leads to a positive feedback on small humidity perturbations. As radiative heating, which was found to be the most relevant process in the accompanying simulations (*Wing and Emanuel*, 2014), depends not only on the vertically integrated moisture content but also on the moisture profile, they introduce a two-layer model for the moisture perturbations:

$$L_v \begin{pmatrix} \partial_t q_1' \\ \partial_t q_2' \end{pmatrix} = \begin{pmatrix} c_{11} & c_{12} \\ c_{21} & c_{22} \end{pmatrix} \begin{pmatrix} q_1' \\ q_2' \end{pmatrix}, \tag{4.10}$$

where L_v is the latent heat of vaporization, q_i' is the deviation from the mean RCE specific

humidity in the lower ($i = 1$) and upper layer ($i = 2$) and c_{ij} are the four linearization coefficients, derived from the dependence of radiative heating, convective transport and vertical advection on humidity.

Evaluating which of these three processes leads to a positive feedback for humidity perturbations, *Emanuel et al.* (2014) find, in contrast to *Craig and Mack* (2013) but in agreement with their simulations, that it is the feedback between longwave radiation and humidity rather than the increase in humidity due to convection. While the vertical advection term is important for the positive feedback it is in fact determined by the two other processes through the weak-temperature gradient approximation, which removes the radiative heating perturbations, and mass conservation, which balances the convective mass-flux.

While we do not go into details of the derivation or the discussion of the individual terms, the proposed feedback mechanism can be summarized as follows. In case of a moist lower troposphere, negative (positive) moisture perturbations lead to stronger (weaker) radiative cooling inducing mean descent (ascent) as horizontal temperature differences are removed by the compensating vertical motion in WTG. This leads to a reinforcing of the original perturbation. As a moist lower troposphere, which is necessary for this feedback to work, is expected only for high sea-surface temperatures, *Emanuel et al.* (2014) argue that this dependence can explain why self-aggregation has been found to only occur for large sea-surface temperatures (e.g. *Khairoutdinov and Emanuel*, 2010).

As we here focus on the spatial evolution of SA, rather than its SST dependence we consider the model in the limit of high SST, and thus a moist lower troposphere, where humidity perturbations are unstable. We find that in this limit, the two layer model can be represented in terms of only one layer as shown in the following. In the case of a very moist lower layer (the condition required for self-aggregation) the lower layer has a high emissivity with weak sensitivity to changes in humidity.

Applying this limit by setting $\epsilon_1 \to 1$ (high emissivity) and $\frac{\partial \epsilon_1}{\partial q_1} \to 0$ (weak humidity dependence) in the equations for c_{ij} given in *Emanuel et al.* (2014), we find that $c_{11} \to 0$ and $c_{21} \to 0$ and thus the perturbation humidity content of the second layer (q_2') decouples from the first layer. Its time evolution and therefore the local interaction term R_E for the model introduced by *Emanuel et al.* (2014) can be expressed as:

$$R_E(q_2') = \frac{1}{L_v} c_{22} q_2' \tag{4.11}$$

where c_{22} is the relevant linearization coefficient, given in *Emanuel et al.* (2014) as

$$c_{22} = \frac{\partial \epsilon_2}{\partial q_2} \sigma T_2^4 \frac{1}{H} \left(\frac{\epsilon_p}{\rho_1} \frac{S_2}{S_1} + \frac{1}{\rho_2} \left(\left(\frac{T_1}{T_2} \right)^4 - 2 \right) (1 - \epsilon_p) \right), \tag{4.12}$$

with σ the Stefan-Boltzmann constant, H the height of one layer, ρ_i, T_i and S_i the density, temperature and dry static stability of layer i. As $\partial \epsilon_2 / \partial q_2$ denotes the dependence of the

emissivity of the second layer on humidity, the first three terms describe the change in radiative cooling of the upper troposphere due to a change in humidity. We do not go into detail on the meaning of the remaining terms, but note that ϵ_p is the ratio of the updraft mass-flux to the total mass-flux, i.e. the mass-flux also including convective downdrafts, introduced in the context of determining the amount of subsidence necessary for compensating the updraft convective mass-flux.

We estimate the parameters in part B of the Appendix and here only summarize the corresponding values:

	H	T_1/T_2	ρ_1/ρ_2	S_1/S_2	$\partial_{q_2}\epsilon_2$	ϵ_p
Value	6000	264.7 / 220.4	0.647 / 0.333	3.9 / 2.3	750	0.8
Unit	m	K	$\mathrm{kg\,m^{-3}}$	$\mathrm{J\,K^{-1}\,m^{-1}}$	1	1

4.2.4. Model Comparison

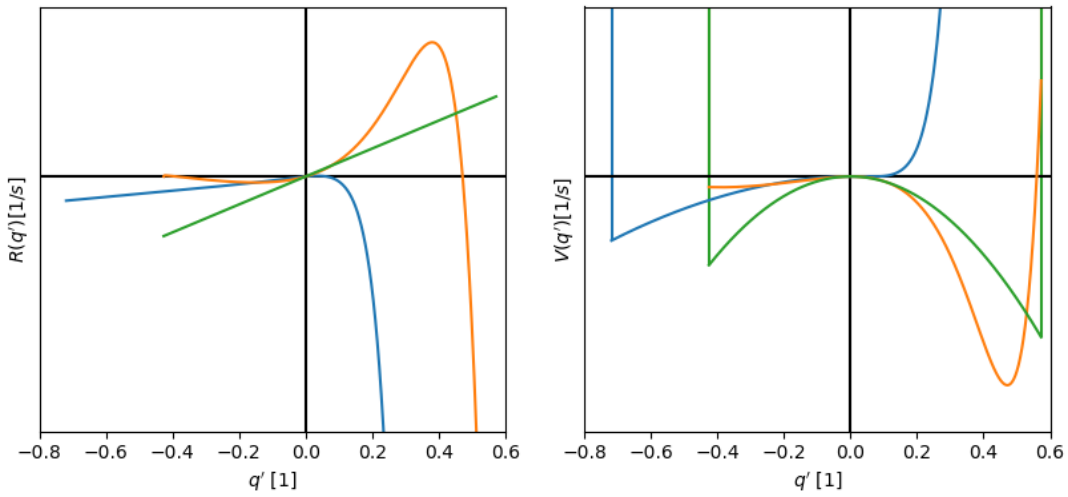

(a) (b)

Fig. 4.4.: Stability analysis of the three models introduced by *Bretherton et al.* (2005) (blue), *Craig and Mack* (2013) (orange) and *Emanuel et al.* (2014) (green). The local evolution equation of humidity as a function of humidity (a) and the corresponding potential (b).

Each model introduced above describes how a small perturbation in humidity content will evolve in time. While they are based on different mechanisms, are derived in different ways

and even account for the humidity content of different layers, they have one important common property: humidity perturbations grow in time. This can readily be seen in Fig. 4.4(a), where we show the local interaction terms (R) for each model, using the parameters introduced above. While the models use different measures of column humidity we replace them by a generic relative humidity parameter q as this is sufficient for our discussion here. Deviations of q from the corresponding horizontal mean radiative-convective equilibrium humidity content q_{RCE} are denoted as q'. Note that q_{RCE} in *Bretherton et al.* (2005) is different from q_{RCE} in *Craig and Mack* (2013) (which we also use for *Emanuel et al.*, 2014), which means that while q always extends from zero to one, q' extends over different intervals, $[-q_{RCE}, 1 - q_{RCE}]$. While $R(q' = 0) = 0$ shows that $q' = 0$ is a time-independent solution in each model, $\partial_q R(q' = 0) > 0$ shows that in all three models any small perturbation will grow in time, i.e. moist perturbations will become increasingly moist while dry perturbations become increasingly dry.

In order to characterize the behavior of the different feedbacks and to relate them to coarsening, we represent each local interaction model also in terms of the potential $V(q)$, see Eq. 4.2. The, numerically integrated, potentials are shown in Fig. 4.4(b). The physical limits on humidity, given by complete dryness ($q = 0$) and saturation ($q = 1$), show up in the potentials as infinite walls at these humidity values. In agreement with coarsening, the potentials represent double-well potentials. We can now visualize the time evolution of any humidity perturbation by "rolling down" into one of the potential minima. In particular, any initial humidity content smaller (larger) than q_{RCE}, the maximum of the potential, will tend to the stable dry (moist) minimum with the drying/moistening rates given by the steepness of the potential.

Comparing the three models suggests that the dry perturbations always tend to an entirely dry state, while *Bretherton et al.* (2005) and *Craig and Mack* (2013) suggest that the moist equilibrium is below saturation, note that the moist minimum in *Bretherton et al.* (2005) is so close to $q' = 0$ that it is hardly visible in Fig. 4.4. In addition to the humidity value of the stable moist and dry state, the differences in the potentials suggest that the time evolution will be different. Since the model introduced by *Emanuel et al.* (2014) has been linearized with respect to q_{RCE}, the corresponding potential is symmetric with respect to q_{RCE} and thus moistening and drying progress at the same speed. For the model based on *Craig and Mack* (2013), moistening is faster than drying, in contrast to the model based on *Bretherton et al.* (2005) where drying is much faster than moistening.

Regarding the time evolution equations given by Eq. 4.8, Eq. 4.9 and Eq. 4.11 as double well potentials compares well with results obtained by weak-temperature gradient studies which examine multiple-equilibria solutions (*Sobel et al.*, 2007; *Sessions et al.*, 2010, 2015, 2016; *Emanuel et al.*, 2014). These studies suggest that, under certain conditions, the final state of a model in WTG depends on the initial humidity content, with dry initial conditions evolving towards a unique dry equilibrium state while moist initial conditions develop towards a unique moist equilibrium state, hence the name "multiple equilibria". Comparison with the

potentials introduced above suggests that the multiple equilibria correspond to the moist and dry potential minima and that the performed experiments are a good framework to explore the properties of the potential.

4.3. Spatial Interaction

The formation of coherent moist and dry regions during self-aggregation suggests, however, that the humidity content within an atmospheric model column is not only affected by a strictly local feedback mechanism but also exchanged between neighboring columns. While the feedback mechanisms in the three models introduced above differ, the cause of the local increase in humidity is convection. *Bretherton et al.* (2005), for example, formulate the forcing terms of their humidity equation in terms of precipitation because they argue that, on physical grounds, the forcing terms should depend on the amount of convection. The increase of humidity by convection is a central component of the model introduced by *Craig and Mack* (2013) and though in the model introduced by *Emanuel et al.* (2014), convection is not the reason for the feedback mechanism, it is again a source of increased humidity.

In the following we show that the humidity content of neighboring columns is coupled if we assume that the convectively-induced increase in humidity is not strictly local but spread within a finite region around the center of the convective updrafts. In addition, we find that we can approximate this coupling by a strictly local increase in humidity combined with a diffusive interaction term.

4.3.1. Stochastic Model

To account for the increase of humidity within a finite region around the convective updraft, we introduce a model where each cloud leaves a humidity footprint of finite size. In particular, the total moisture increase due to one cloud, q_0, is distributed in space according to $\phi(\Delta)$ where Δ is the distance to the cloud center and the spatial distribution function $\phi(\Delta)$ is normalized to one, i.e. $\int_{-\infty}^{\infty} \phi(\Delta) d\Delta = 1$. The increase in humidity at a given location x due to convection depends thus on the rate of clouds n whose centers form close enough to x. This increase in humidity can be expressed by the following integral:

$$\partial_t q(x) = \int_{-\infty}^{\infty} n[q(x+\Delta)] q_0 \phi(\Delta) d\Delta \tag{4.13}$$

where a cloud at $x + \Delta$ increases the humidity at x by $q_0\phi(\Delta)$. The rate at which clouds form within $[x, x + dx]$ is given by $n[q(x, t)]$dx and depends only on the relative humidity $q(x, t)$.

We first consider a linear increase of cloud number with humidity, i.e. $n[q] = n_0 + n_1(q - q_{RCE})$ and note that this also represents a first order Taylor expansion of a more complicated $n[q]$ around q_{RCE}. For the spatial distribution function, we assume for simplicity that each cloud leads to a constant increase in humidity, up to a distance of r_{fp} from the cloud core. To numerically model this equation we need to estimate the following parameters:

- q_{RCE}: the homogeneous humidity content in an RCE simulation
- n_0: the average number of clouds per time and area at q_{RCE}
- n_1: the additional number of clouds per time, area and Δq at $q_{RCE} + \Delta q$
- q_0: the total increase in humidity associated with one cloud
- r_{fp}: the radius of the humidity footprint

To estimate the parameters we start from the dependency of precipitation on humidity, given in Eq. 4.7, found by *Bretherton et al.* (2005). They find $q_{RCE} = 0.72$ and $a_m = 16.6$. Assuming that precipitation is a proxy for the amount of convection, we estimate $n[q] = n_0 \exp(a_m(q - q_{RCE})) \approx n_0 + n_0 a_m(q - q_{RCE})$, i.e. $n_1 = n_0 a_m$. *Scheufele* (2014) found on average about 1000 deep convective clouds within a $128\,\mathrm{km} \times 128\,\mathrm{km}$ domain in an RCE simulation at 125 m resolution with a radiative forcing of $-4\,\mathrm{K\,d^{-1}}$. Assuming an average cloud life-time of one hour allows us to estimate $n_0 = 1.7 \times 10^{-11}\,\mathrm{s^{-1}\,m^{-2}}$ and $n_1 = n_0 a_m = 2.8 \times 10^{-10}\,\mathrm{s^{-1}\,m^{-2}}$. For q_0 we assume that one cloud increases the humidity from q_{RCE} to saturation (i.e. $q = 1$) within a radius of 500 m around the cloud center, which gives $q_0 = (1 - q_{RCE})\pi r^2 =. 2.4 \times 10^5\,\mathrm{m^2}$. Finally we estimate the radius of the humidity footprint as $r_{fp} = 10 \times 10^3\,\mathrm{m}$.

Starting from a humidity field with a step-function profile in x-direction, as can be seen in the top row of Fig. 4.5, a cloud is assigned with probability $n[q(i,j)]$ at every site (i,j). Note that we enforce a lower and an upper limit on the humidity content of $q_{RCE} - 1/a_m \leq q \leq 1$. While the upper limit is a physical limit, the lower limit ensures that the rate of clouds cannot become negative. If a cloud is assigned to site (i,j), its humidity together with the humidity of all cells with a distance less or equal to r_{fp} is increased by $q_0/\pi r_{fp}^2$. Here we choose that, during each time-step, at maximum one cloud can form per grid cell as the chosen horizontal resolution of 1 km and the corresponding time step of 60 min approximately correspond to the size and lifetime of a deep convective cloud. The profile of a sample model output after ten hours is shown in addition to the initial profile in the top row of Fig. 4.5 and the corresponding snapshot in the middle row. The front between the moist and the dry region after ten days has propagated into the dry regions and the gradient has been smoothed.

4.3.2. Deterministic Approximation

In the following we will show that the model described by Eq. 4.13 can be approximated by a Reaction-Diffusion Equation. Using, as above, a first order Taylor expansion of $n[q]$ and

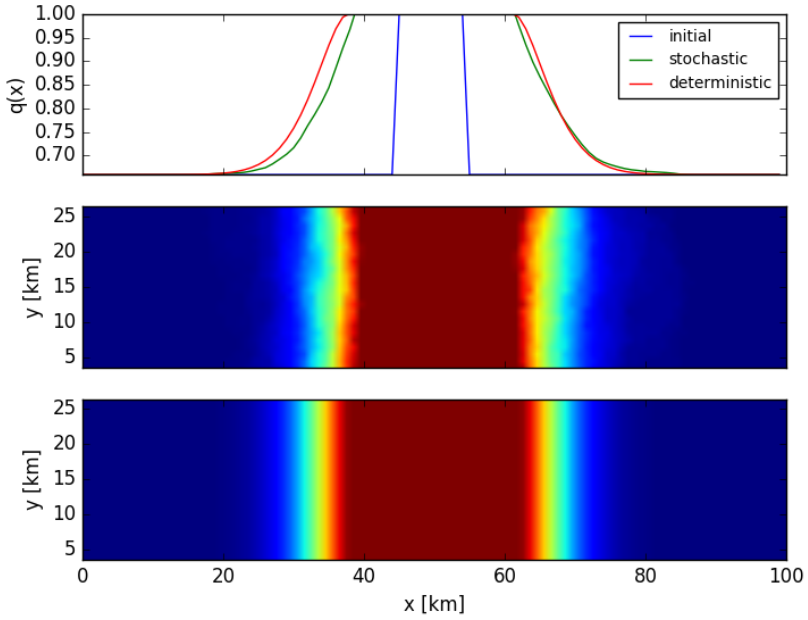

Fig. 4.5.: Top row shows the initial humidity profile (blue) and humidity profiles after ten hours for the stochastic model (green) and the deterministic model (red). The middle and bottom rows show snapshots of the stochastic and deterministic model after ten hours respectively.

in addition a second order Taylor expansion of $q(x+\Delta)$:

$$n[q] \approx n_0 + n_1 q$$
$$q(x+\Delta) \approx q(x) + \Delta \partial_x q|_x + \frac{\Delta^2}{2}\partial_x^2 q|_x$$

Eq. 4.13 can be written as

$$\partial_t q(x) \approx (n_0 + n_1 q(x)) q_0 \underbrace{\int_{-\infty}^{\infty} \phi(\Delta) d\Delta}_{=1} + n_1 q_0 \partial_x q \underbrace{\int_{-\infty}^{\infty} \Delta \phi(\Delta) d\Delta}_{=0} +$$
$$+ \frac{1}{2} n_1 q_0 \partial_x^2 q \underbrace{\int_{-\infty}^{\infty} \Delta^2 \phi(\Delta) d\Delta}_{\text{depends only on choice of } \phi} \tag{4.14}$$
$$= (n_0 + n_1 q(x)) q_0 + D \partial_x^2 q \tag{4.15}$$

where the integral in the first term is one due to the normalization constraint of $\phi(\Delta)$, the integral in the second term vanishes as we integrate an asymmetric function over a symmetric interval while the integral in the last term is determined by the choice of $\phi(\Delta)$.

Eq. 4.15 has the same functional dependence as a Reaction-Diffusion equation, see Eq. 4.1. The reactive part is given by $(n_0 + n_1 q(x))q_0$ and the diffusive part by $D\partial_x^2 q(x,t)$, with the diffusion coefficient

$$D \equiv \frac{1}{2} n_1 q_0 \int_{-\infty}^{\infty} \Delta^2 \phi(\Delta) d\Delta. \tag{4.16}$$

This derivation is similar to Einstein's famous "proof" of the existence of Brownian motion (*Einstein*, 1905). It runs analogously in the two dimensional case.

Assuming $\phi(\Delta)$ is constant up to a distance r_{fp} and zero for distances larger than r_{fp}:

$$\phi(\Delta) = \begin{cases} \frac{1}{\pi r_{fp}^2} & \text{for } \Delta \leq r_{fp} \\ 0 & \text{else} \end{cases}$$

the 2D diffusion coefficient is given by

$$D = \frac{n_1 q_0}{8} r_{fp}^2. \tag{4.17}$$

Using Eq. 4.17 and the parameters estimated above, results in $D = 3.1 \times 10^2 \,\mathrm{m^2\,s^{-1}}$.

Starting from the same initial humidity profile previously used for the stochastic model, a snapshot of the time evolution after ten hours of this deterministic model is shown in the bottom row of Fig. 4.5 with the corresponding humidity profile shown in the top row. It closely resembles the evolution of the stochastic model but is completely symmetric in the y-direction, without any fluctuations in propagation speed and boundary width as in the stochastic model.

Equation 4.15 therefore shows that if convection is more likely to occur in moist regions and we assume that clouds increase the humidity in the free troposphere within a finite region around the cloud center this can be approximated by a strictly local increase of humidity due to the number of clouds at that location and a diffusion term.

4.4. Spatial Evolution

Section 4.3 shows that the moistening of the atmosphere within finite regions around convective updrafts can be approximated by a Reaction-Diffusion Equation. The model described by Eq. 4.15 so far only includes the tendency of the atmosphere to moisten regions of increased convection, but we know from Section 4.2 that there exists a positive feedback where not only moist regions get moister but also dry regions drier. As we have seen that the three local interaction terms R_B (Eq. 4.8), R_C (Eq. 4.9) and R_E (Eq. 4.11) can be described as

derivatives of a double well potential, combining them with a diffusive interaction term leads to three TDGL equations.

Starting from a slightly perturbed homogeneous state of $q = q_{RCE}$ we now examine the time evolution of two dimensional humidity fields resulting from the three models.

4.4.1. Snapshots

As expected from coarsening, snapshots of the three models show the formation and upscale growth of coherent moist and dry regions, see Figs. 4.6-4.8. While all three models show this generic behavior, there are significant differences between them which reflect the differences in the potentials. For example, the humidity values of the dry and the moist regions are clearly different in the three models. These are given by the two minima of the potentials, see Fig 4.4(b), with the humidity content of the dry region given by the potential minimum below q_{RCE} and the humidity content of the moist region by the potential minimum above q_{RCE}. While for all three models the dry minimum is at $q = 0$, the moist minimum has different humidity values, clearly reflected in the different humidity values of the moist regions in Figs. 4.6-4.8. An other difference is the rate of drying and moistening, which for each value of q is given by the gradient of the potential at q. The steeper the gradient, the larger the drying or moistening rate. Note that the snapshots we show for the model based on the results by *Bretherton et al.* (2005) are taken after a longer simulation time than the snapshots for the two other models. This is necessary as the gradient of R_B close to zero is small compared to the other two models. As we do not have a constraint on the global amount of convection, different drying and moistening rates also affect the proportion of moist in comparison to dry regions.

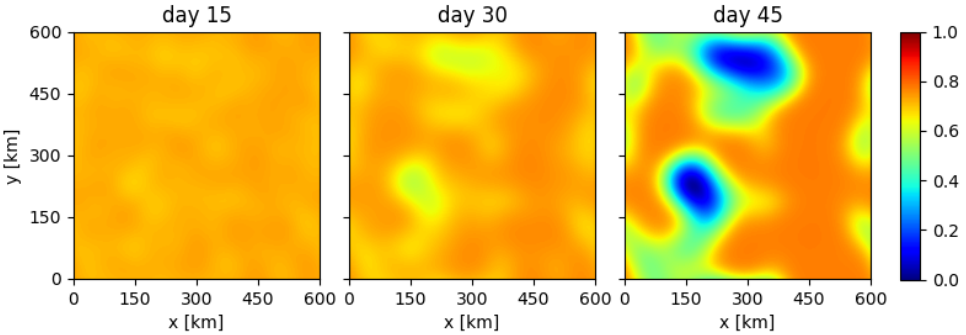

Fig. 4.6.: Snapshots of the humidity perturbations obtained by numerical simulation of the model based on the results from *Bretherton et al.* (2005). Starting from a slightly perturbed homogeneous state, the snapshots show the model domain after 15 days (left), 30 days (middle) and 45 days (right)

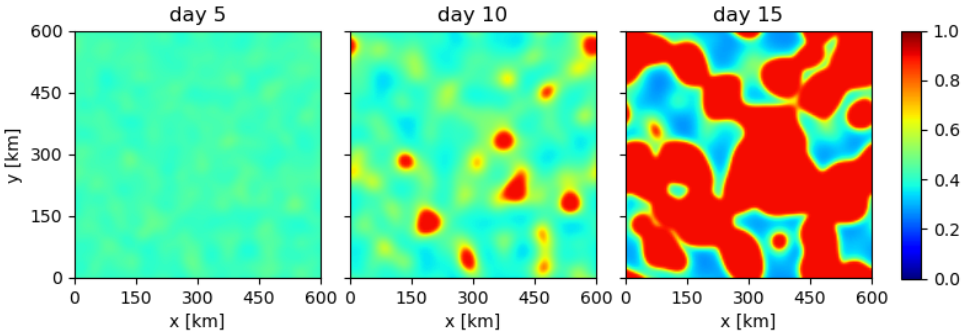

Fig. 4.7.: As in Fig. 4.6 but for the model based on the results from *Craig and Mack* (2013) and days 5 days (left), 10 days (middle) and 15 days (right).

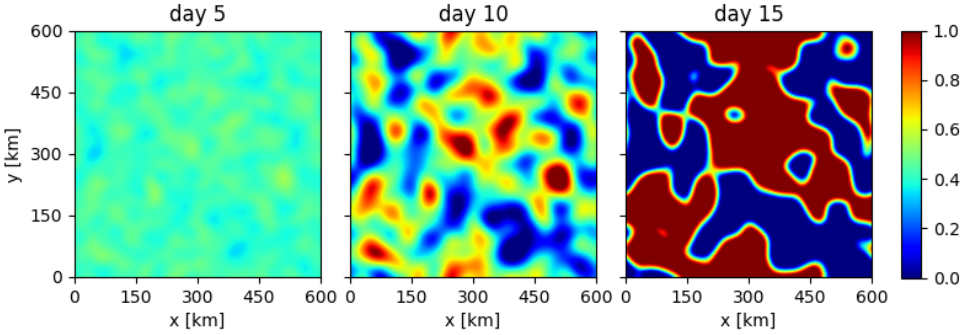

Fig. 4.8.: As in Fig. 4.6 but for the model based on the results from *Emanuel et al.* (2014) and days 5 days (left), 10 days (middle) and 15 days (right).

4.4.2. Scaling

As one of the central properties of coarsening is dynamical self-similarity, we now show the average scaling of the typical length scale with time for the three models and compare them to the expected $t^{1/2}$ scaling, see Eq. 4.3.

In particular, Fig. 4.9 shows the scaling of the auto-correlation length l_{cor} with time for all three models. For each model the average of ten runs is calculated. We show the plot with a double logarithmic scale, as a power-law dependence will then appear as a straight line. In addition to the scaling of the model, Fig. 4.9 shows the scaling we expect from Eq. 4.3. We find that, after an initial transition phase, the time evolution of the auto-correlation length in all three models is well described by Eq. 4.3, during the formation and the upscale growth of moist and dry regions.

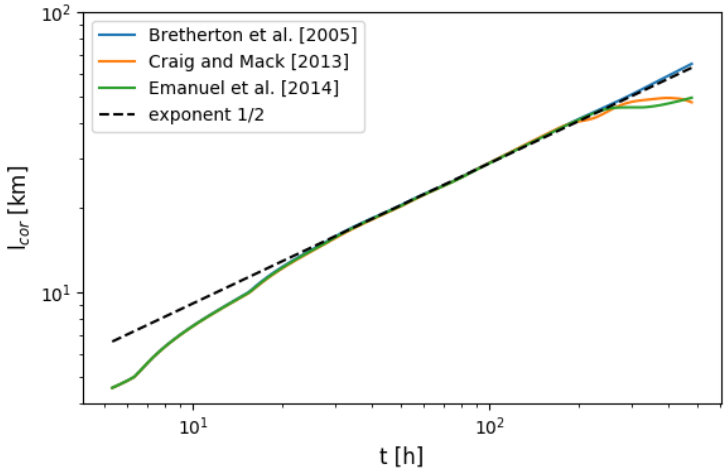

Fig. 4.9.: Scaling of the average auto-correlation with time for the three different models (colored lines) and the theoretically expected dependence (dashed line).

4.4.3. Domain Wall Properties

Finally, we determine the dependence of the boundaries between moist and dry regions on diffusion. As we have seen above, we expect the barrier width between the two stable regions to be proportional to the square root of the diffusion coefficient.

To determine the average width of the barrier between a moist and a dry region we again use simulations initialized with a step-function as shown in Fig. 4.5 but now q in the drier region is set to zero. We simulate the propagating barrier for five days and determine average profiles of the domain barriers for the last three days. Defining the barrier width as the

distance over which q increases from the humidity content of the dry state (plus a small offset $\Delta = 5 \cdot 10^{-3}$) to the humidity content of the moist state (minus Δ), the resulting dependence on the diffusion coefficient D is shown in Fig. 4.10.

We find the expected dependence of the barrier width on D for all three models introduced above. In addition we note that for a given diffusion strength, the barrier width is always smallest for the model based on *Emanuel et al.* (2014) and largest for the model based on *Bretherton et al.* (2005). In particular, we find that for the diffusion strength determined in section 4.3 the resulting barrier widths for the individual models are approximately 47 km for the model based on *Bretherton et al.* (2005), 39 km for the model based on *Craig and Mack* (2013) and 21 km for the model based on *Emanuel et al.* (2014). This difference in barrier width is also clearly visible in Figs. 4.6-4.8.

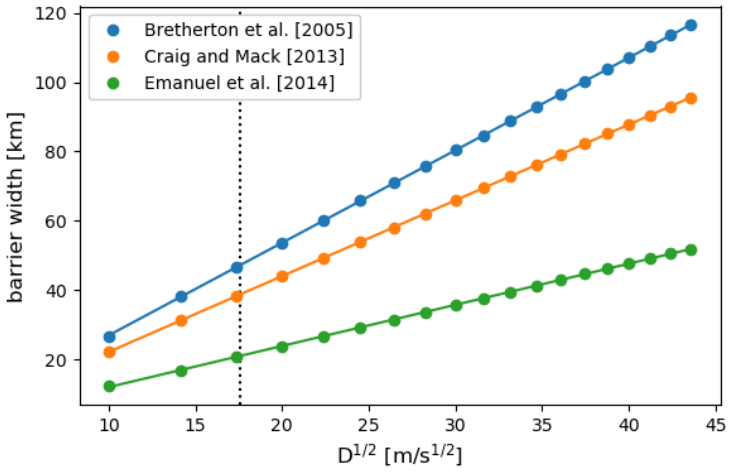

Fig. 4.10.: Test scaling hypothesis for barrier width for three different models (dots) and corresponding fits (line). The black dotted line marks the diffusion coefficient determined in section 4.3.

4.5. Comparison of coarsening and self-aggregation in RCE simulations

The results from the previous section suggests that self-aggregation of convection in RCE simulations might be explained by a process called coarsening. In this section we will compare properties of coarsening with properties observed in RCE simulations.

4.5.1. Upscale Growth

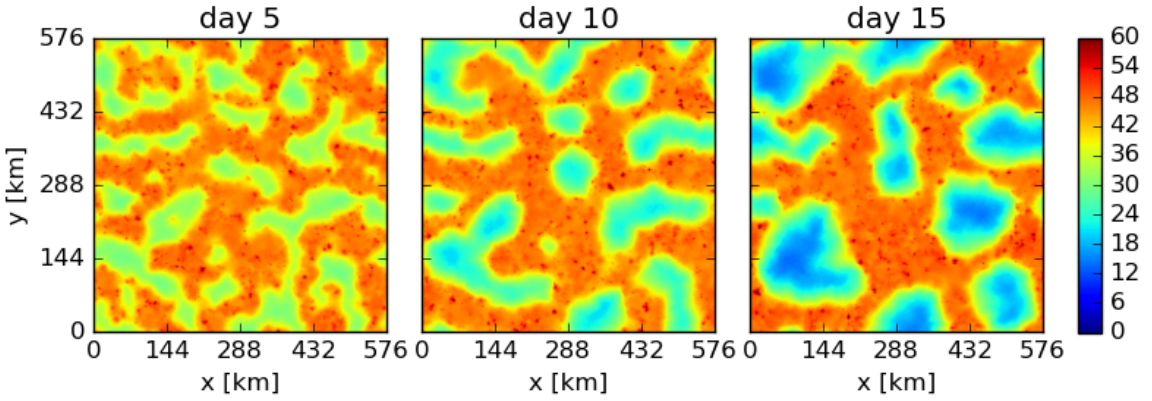

Fig. 4.11.: Snapshots of WVP field in RCE simulation performed by *Hohenegger and Stevens* (2016).

Figure 4.11 shows snapshots of the water-vapor path in the RCE simulation described in *Hohenegger and Stevens* (2016). For this simulation they used the University of California Los Angeles Large-Eddy Simulation model coupled to a slab-ocean with a depth of 500 m, a horizontal domain size of 576 x 576 km and a spatial resolution of 3 km, see *Hohenegger and Stevens* (2016) for more details on the simulation. As expected for coarsening and seen in Figs. 4.6-4.8, by day 5 coherent moist and dry regions have formed, which show a clear upscale growth in the following. The barrier width between moist and dry regions in Fig. 4.11 at day 15 is approximately 50 km, which is larger though comparable with the barrier widths we found for the simple models in the previous section. *Hohenegger and Stevens* (2016) noted that drying is faster then moistening, resembling the evolution in the model based on *Bretherton et al.* (2005). It is interesting to note that also numerical simulations differ with respect to whether drying or moistening happens faster. While some studies find drying to be significantly faster than moistening (*Wing and Emanuel*, 2014; *Hohenegger and Stevens*, 2016), other studies find a simultaneous drying and moistening (*Holloway and Woolnough*, 2016).

4.5.2. Scaling in RCE simulations

We now determine whether the observed upscale growth in moist and dry regions agrees with the scaling expected for coarsening, see Eq. 4.3. After an initial phase of rapid growth in the correlation length, associated with the initial separation into dry and moist regions also seen in Fig. 4.9, scaling follows the expected scaling for days 3 to 10, after which it grows more rapidly, with small deviations up to day 23 and strong deviations afterward.

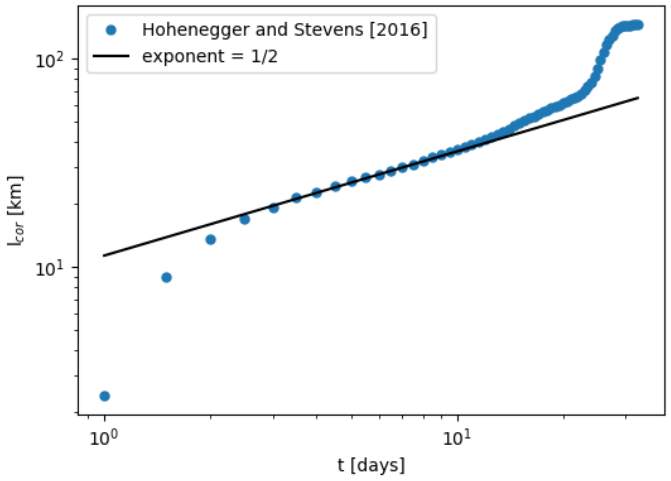

Fig. 4.12.: Scaling of the auto-correlation length with time for the WVP in *Hohenegger and Stevens* (2016) (blue dots) and the expected scaling (black line).

This suggests that coarsening may be important during the early stages of self-aggregation but becomes less important during later stages. Perhaps this departure denotes the transition to a circulation dominated phase of self-aggregation, as discussed in the introduction of this chapter. Note that one must be cautious about drawing conclusions from a single realization on a very limited domain as scaling is usually averaged over many runs in large domains.

In an other RCE simulation, performed by *Wing and Cronin* (2016), they find scaling of the autocorrelation length with time but with an exponent of approximately one. We note, however, that they used a very elongated, channel-like, domain which led to the formation of persistent moist and dry stripes, and thus a quasi-one-dimensional humidity field, while power-law scaling with an exponent of $1/2$ is only expected for dimensions $d \geq 2$. The observed dependence of self-aggregation on domain shape is discussed in the next section.

4.5.3. Domain Shape Dependence

The appearance of SA is strongly influenced by the shape of the domain, in particular the final shape of the moist region is found to be either circular or band-like. Which of these two is realized seems to depend on whether the domain is square, resulting in circular moist regions (e.g. *Bretherton et al.*, 2005; *Muller and Held*, 2012; *Kempf*, 2013; *Jeevanjee and Romps*, 2013; *Hohenegger and Stevens*, 2016), or channel-like, resulting in moist bands (e.g. *Tompkins*, 2001a; *Posselt et al.*, 2012; *Wing and Cronin*, 2016). One exception to this rule is the RCE simulation performed by *Tompkins and Craig* (1998), who found a band-like moist region despite using a square domain. Note however that this simulation was performed on a

very small domain, the extent of which being on the order of or even smaller than the smaller extent in the channel-like geometries.

Holloway and Woolnough (2016) have pointed out that this dependence on the shape of the domain is explained if SA tends to minimize the length of the boundary. Assuming a moist region of area A^{moist}, they showed that for a domain with the shortest domain side of length L, there exists a critical area $A_c^{moist} = L^2/\pi$ above which the minimal boundary length is given by a moist band rather than a moist circle. A minimization of the boundary length is exactly what we expect from coarsening, where the stable solution must minimize the free energy given in Eq. 4.4. If the final solution contains a moist and a dry region, corresponding to the humidity values of the two potential minima, energy minimization necessarily means that the boundary between these two regions will be minimized, as any humidity values between q_1 and q_2, the respective humidity values of the dry and the moist minimum, will necessarily have higher $V(q) > V_{min}$, i.e. higher free energy.

As explained above, our models are supposed to represent a small subdomain of a larger domain and we therefore have no constraint on e.g. latent heat release (as is the case in RCE) so our domains are allowed to become completely moist or completely dry. Nevertheless, the tendency of coarsening to favor banded versus circular moist regions can already be seen during the evolution, as shown in Fig. 4.13. Figure 4.13 shows snapshots of two simulations, both using the model based on *Craig and Mack* (2013), after 12 days. The two simulations are identical apart from the domain size. The domain in Fig. 4.13(a) is channel-like, with a domain size of $60\,\mathrm{km} \times 600\,\mathrm{km}$, and square in Fig. 4.13(b), with a domain size of $600\,\mathrm{km} \times 600\,\mathrm{km}$. In the channel-like domain, multiple moist bands have formed while in the square domain circular moist regions have formed, in agreement of boundary length minimization.

4.5.4. Domain Size Dependence in RCE Simulations

We have seen in Section 4.1.4 that the barrier width is completely determined by the potential and the diffusion coefficient and should thus be independent of the domain size. This can explain the sensitivity of self-aggregation to domain size which was found by *Bretherton et al.* (2005), *Muller and Held* (2012) and *Jeevanjee and Romps* (2013), who show that self-aggregation only occurs for domains greater then 200-300 km.

If, in a domain with periodic boundary conditions, the domain size is of the order of the barrier width or smaller, diffusion is too strong and the two stable regions can no longer occur within the same, periodic, region. As in RCE the domain can neither become completely dry nor completely moist, diffusion will tend to a homogeneous humidity content within the domain.

An example for this is shown in Fig. 4.14, where we initialize two simulations by the humidity distribution shown in the top row. To set the front propagation speed to zero, we

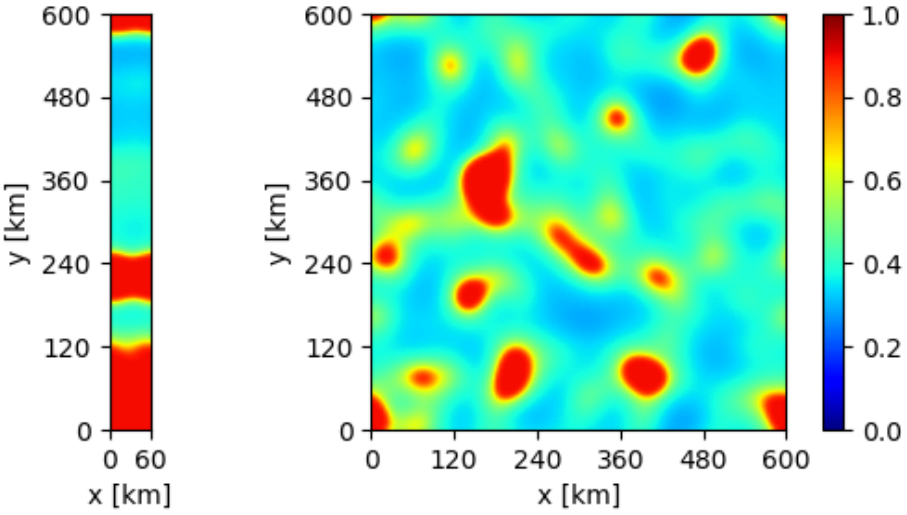

(a) (b)

Fig. 4.13.: Snapshot of simulation based on *Craig and Mack* (2013) after 12 days in channel-like domain (a) and square domain (b).

here consider a symmetric version of the model with the local interaction term described in Eq. 4.11 by setting q_{RCE} to 0.5. The only difference between the two simulations is the domain size, which is $10\,\mathrm{km} \times 20\,\mathrm{km}$ in the left figure and $100\,\mathrm{km} \times 200\,\mathrm{km}$ in the right figure. We find that after 50 days, the large domain has reached a steady state with a single moist and a single dry region, now separated by a smooth domain wall, while the smaller domain has evolved to a completely homogeneous state of $q = q_{RCE}$.

4.6. Conclusion

In this chapter we have shown that the upscale growth of moist and dry regions during self-aggregation of convection can be described by a process called coarsening if the relevant feedback acts locally and the spatial coupling is diffusive.

To derive spatial evolution equations for self-aggregation, we combined three positive feedback mechanisms introduced in previous studies (*Bretherton et al.*, 2005; *Craig and Mack*, 2013; *Emanuel et al.*, 2014) with a spatial interaction term. We chose a diffusive interaction which, as we have shown, approximates a humidity increase due to convection within a finite region around convective cores if the amount of convection depends only on humidity content. The upscale growth of moist and dry regions in the three resulting spatial evolution equations is described by coarsening.

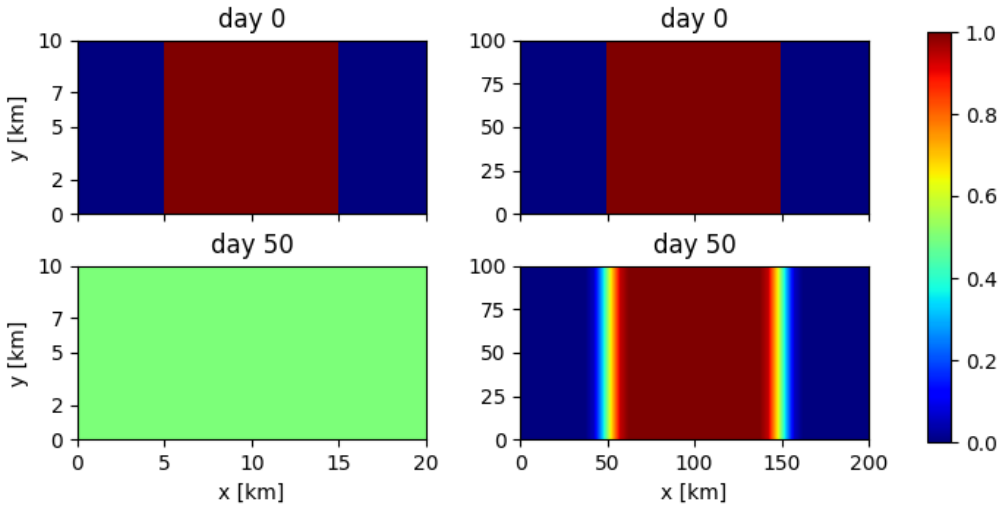

Fig. 4.14.: Domain size dependence of humidity fields. Numerical simulations, identical apart from domain size, are started from the initial humidity distributions given in the top row and the corresponding humidity field after 50 days is given in the bottom row.

Comparing properties of coarsening with properties of self-aggregation observed in atmospheric model simulations we find that we can explain why the shape of the final moist region changes with domain shape (channel vs. square) and why self-aggregation depends on domain size. Comparison of the upscale growth of the moist and dry regions in an RCE simulation with the predictions from coarsening are however ambiguous, suggesting that coarsening is relevant mainly during the onset of self-aggregation, potentially followed by a moisture advection dominated phase.

These findings emphasize two important points. First, the similarity in the appearance of self-aggregation in different numerical simulations does not mean that there is a unique feedback mechanism but rather that they have the same underlying pattern formation mechanism. Second, to understand which pattern formation mechanism is relevant we need to better understand how humidity is exchanged horizontally.

5. Conclusion

5.1. Summary

In this thesis we have established three simple models to determine the consequences of convective organization. Focusing on organization which results from convection itself, we have investigated how cold pool induced boundary layer perturbations and free tropospheric humidity perturbations lead to spatial and temporal correlations in the convective field. In chapters 2 and 3 we have examined how the cold pool induced clustering of updrafts and the cold pool induced propagation of convective activity can explain the observed power-law scaling in convective size and event-size distributions, respectively. Finally, we have shown in chapter 4 how a positive local feedback on humidity can lead to upscale growth of convectively active and inactive regions, commonly observed in numerical simulations and known as self-aggregation of convection. In each chapter, we have introduced a simple model and related it to a model known from statistical physics, which has enabled us to profit from the extensive research that has gone into them. Before summarizing the individual models, we shortly describe the idealized picture of convection which motivates them.

While the amount of convection is determined by the large scale forcing, the spatial distribution of convection depends on cold pools and humidity perturbations. As cold pools spread, updrafts form along their boundaries. In snapshots of the spatial distribution of individual updrafts this shows up as a clustering of updrafts along the cold pool boundaries. In addition to this clustering, cold pools induce correlations between different generations of convective cells. While the cloud, which initially caused the cold pool, dies and locally suppresses convection until it has recovered, some of the updrafts formed along the boundary grow large enough to, in their turn, produce precipitation and induces a new cold pool. While the individual updrafts have length scales of the order of 100 m, the cold pools extend, on the time scale of hours, to several kilometers. The two models we have introduced in chapters 2 and 3 represent these two aspects of cold pool induced correlations.

Despite homogeneous forcing and boundary conditions, a large number of radiative-convective equilibrium simulations show self-aggregation of convection, i.e. a spontaneous partitioning of an initially homogeneous domain into moist convecting and dry non-convecting regions. Convection is known to contribute to the intensification of the humidity perturbations by preferentially occurring in moist regions where they lead to a local increase in free tropo-

spheric humidity. Compared to cold pool perturbations, self-aggregation acts on timescales of the order of days and leads to humidity perturbations with length scales of 100 km. We have introduced a model to describe the spatial evolution of self-aggregation in chapter 4.

Size distributions of shallow cumulus clouds

In chapter 2, we have shown that the clustering of updrafts is important to understand the observed size distributions of shallow cumulus clouds. In particular, we have introduced a model based on percolation but modified it to account for cold pool induced clustering.

Standard percolation describes the properties of clusters which form from overlapping of randomly distributed objects. At a critical coverage fraction, spatial correlation diverges and, in the limit of an infinite domain size, an infinite cluster forms. Using a large satellite data set in section 2.2 we have sorted the satellite scenes according to cloud fraction and thus determined the cloud size distributions as a function of coverage fraction. We have found that the size distributions follow the same functional dependence and show the same sensitivity to coverage fraction as clusters in percolation below the critical coverage fraction.

Without clustering however, the merging of randomly distributed objects at low coverage fractions is not frequent enough to explain the observed power-law scaling. Only by including a simple representation of clustering and an underlying exponential distribution of convective cell size in the percolation model in section 2.3 did we obtain accurate quantitative prediction of the power law slope and position of the scale break. As we could not determine the clustering and cell size distribution directly, we used the satellite data to extract approximations for the mean cell size and the necessary clustering parameters.

Propagation of convective activity

The question we have addressed in chapter 3 is whether convection triggering new convection via cold pools can explain the continuous phase transition in convective activity, observed by *Peters and Neelin* (2006). Before we introduced a model to explain how the dependence of convective activity on cold pool triggering can lead to a phase transition at the end of section 3.1, we reviewed the results of *Peters and Neelin* (2006) and discuss their relation to known properties of non-equilibrium phase transitions. From this we have argued that the phase transition should result from a process which is independent of radiative forcing and compensating subsidence. Assuming that, in the absence of large scale forcing, convection depends on being triggered by cold pools generated by previous convection, we have proposed that this can explain the origin of the observed phase transition and also that this places the phase transition in the universality class of directed percolation.

As a first step of testing this hypothesis, we have represented the subsequent triggering of clouds via cold pools using a population model with global control. In the 2D lattice model,

activity can spread from active sites to neighboring sites, as long as they are not in the inhibition state, while the total number of active sites is fixed. Based on the picture of convection introduced above, active sites correspond to convective sites, spreading of activity and local inhibition is caused by cold pools and the global control on number corresponds to the amount of convection fixed by the large scale forcing. The model is based on directed percolation and shows not only an underlying phase transition with respect to the trigger probability but also critical behavior in the low density limit. Note that, apart from the inhibition state which we included to represent the time it takes the cold pool perturbations to recover, it corresponds to the population model originally introduced by *Broeker and Grassberger* (1999). In section 3.2 we introduced two complementary methods to determine the necessary model parameters and to quantify the spreading of convective activity using an atmospheric model simulation. After applying these methods to a radiative-convective equilibrium simulation performed by *Scheufele* (2014) and using the respective parameters to set up the lattice model, we found in 3.3 that the simple model can approximately reproduce the spreading of convective activity observed in the atmospheric model.

While this is promising, in particular as the simple model in itself may prove useful in the development of a future convection parameterization, this can really only be seen as a first step in verifying our hypothesis. We therefore concluded the chapter by discussing in section 3.4 how, as a next step, one could decouple convection from the mean state in an atmospheric model to investigate the underlying phase transition in convective activity more explicitly.

Spatial evolution of self-aggregation

In chapter 4 we have addressed the question whether self-aggregation, the upscale growth of precipitating moist regions and dry regions without deep convection, corresponds to a phase separation of moist and dry air by a process called coarsening. Coarsening relies on two basic ingredients: local bistability and diffusive spatial interaction.

Reviewing the literature in 4.1, we concluded that weak-temperature gradient simulations show direct evidence for local bistability of the atmosphere to perturbations in the humidity content. Starting from a range of different humidity values, the humidity content evolves either to a stable moist or to a stable dry state (e.g. *Sessions et al.*, 2010). Despite varying feedback mechanisms we have argued in section 4.2 that local bistability is also the key property of all theoretical models attempting to explain self-aggregation (*Bretherton et al.*, 2005; *Craig and Mack*, 2013; *Emanuel et al.*, 2014).

While a diffusive spatial interaction has already been suggested by *Craig and Mack* (2013) it lacked physical motivation. We have shown, in section 4.3, that diffusion correctly approximates the humidity increase due to stochastically triggered convection, if the interaction of convection and humidity is based on two assumptions. First, the probability of convection

depends only on the humidity content and second, the increase in humidity due to convection is distributed within a finite region. Based on these assumptions we have shown that this can, in the limit of infinitely many clouds, where each leads to an infinitely small increase in humidity, be expressed in terms of a strictly local increase in humidity and a diffusive, down gradient transport of humidity. This result prompted us to combine the positive feedbacks proposed by *Bretherton et al.* (2005), *Craig and Mack* (2013) and *Emanuel et al.* (2014) with a diffusive interaction term in section 4.4 and to discuss which properties of the resulting spatial evolution depend on the feedback details and which are the same for all three feedback models because they are a universal property of coarsening.

Finally, in section 4.5, we have compared properties of coarsening with properties observed in radiative-convective equilibrium simulations. We started by showing that the upscale growth of moist and dry regions in a radiative convective equilibrium simulation follows, at least initially, the scaling law predicted by coarsening. In addition we found that regarding self-aggregation as a coarsening process we were able to explain two properties frequently observed in numerical simulations. First, as the upscale growth of moist and dry regions in coarsening models is driven by the minimization of the boundary length between the two stable regions, coarsening can explain why channel like domains lead to the formation of moist and dry bands while large square domains lead to the formation of circular moist regions. Second, we have argued that the dependence of the width of the boundary on diffusion explains the observed dependence of self-aggregation on domain size. If the domain size gets too small to support a moist and a dry region separated by a boundary of a given width we have shown that this can, despite bistability, result in a homogeneous humidity distribution.

What unites these models?

Comparing the three introduced models and in particular their underlying theoretical models: isotropic percolation, directed percolation and coarsening, we find that universal scaling laws are an important property of each. Universality, as mentioned in section 2, has first been introduced in the context of continuous phase transitions and describes the insensitivity of, for example, the critical exponents to model details.

Both types of percolation, isotropic and directed, show a continuous phase transition when the coverage fraction or the triggering probability, respectively, crosses a critical value.

While, for the size distribution model, we have argued that we are actually below the critical point, *Ding et al.* (2014) suggest that, for a range of different lattice types, the cluster size distribution approaches the critical distribution in a quantitatively similar way. In particular they find that all size distributions are described by power-law scaling with exponential drop-off, with a pure power-law scaling recovered at the critical point, and suggest scaling, at least for the cut-off parameter.

For deep convection, the concepts of universality applies more directly as the atmosphere has

been suggested to be in a self-organized critical state. If the atmosphere self-tunes towards its critical point, knowledge of the universality class should give the correct exponents for the observed scaling of size distributions and the power-law pick up in the order parameter. We have here suggested that the underlying phase transition falls in the universality class of directed percolation.

The behavior of coarsening is not determined by the critical point of a continuous phase transition but a number of properties are nevertheless found to be independent of feedback details, i.e. details in the shape of the underlying double well potential. Above all, the dynamical exponent in the upscale growth of the stable regions has been described as being even "more universal" (*Sethna*, 2006, p. 250) than critical exponents as it is not only independent of feedback details but also independent of dimension.

The importance of universality for the introduced simple models and thus potentially the atmosphere is a key result of this thesis and something that we did not envisage at the beginning.

5.2. Future Work

Studying convective organization using models from statistical physics is a novel approach. As such, it is perhaps not surprising that there remain a number of tasks for future research. We divide these tasks into three groups:

- how can we assess the limitations of our models?
- how can we include the effects of convective organization in parametrizations?
- how can we further increase our understanding of convection?

5.2.1. Limitations

Rather than attempting to give a complete list of limitations or possible verification methods, we will now discuss what we believe to be the most relevant test for each of the models introduced above.

Size distributions of shallow cumulus clouds

The key assumption we have made in explaining the size distribution of shallow cumulus clouds using a percolation model in chapter 2 is that power-law scaling results from clouds being clusters of cloud cells. This hypothesis could be tested explicitly if the clouds were separated into cloud cells.

A possible method for dividing clouds into cloud cells using infrared satellite images has been introduced by *Kuo et al.* (1993). While most studies have determined size distributions from reflectance fields, using visible or near-infrared channels, *Kuo et al.* (1993) used brightness temperature fields determined from a $11.5\,\mu\mathrm{m}$ infrared channel. As cloud top temperatures, and thus also cloud top heights, are approximately given by the brightness temperature, they investigated, in addition to the cloud areas, also the height profiles of the clouds to determine cloud cells. In particular, after applying an initial temperature threshold to each satellite image to separate the clouds from the background, this threshold is successively decreased, i.e. the height threshold is increased. If the cloud splits up into more than one cell candidate and, if these candidates fulfill some further requirements on size and depth, they are considered cloud cells.

Similarly, *Scheufele* (2014) introduced a method for dividing convective clouds in an atmospheric model into cloud cells. Motivated by the cloud tracking algorithms of *Dawe and Austin* (2012) and *Heus and Seifert* (2013), cloud cores are identified as local maxima in the vertical velocity field at a height of 2.4 km with non-zero cloud water content. Following *Heus and Seifert* (2013), a region growing process divides the cloudy grid points to cloud cells by assigning them to cloud cores depending on their distance to and the strength of the cloud cores.

After having separated the clouds into cloud cells, one can determine the cell size distribution and compare it to the cloud size distribution. For a direct test of the model, one could supply the cell size distribution and the clustering properties to the introduced modified percolation model and test whether it can, within the limit of random variations, reproduce the observed size distribution.

Determining the cloud cells directly would, in addition, allow testing of our assumptions regarding the underlying cloud cell size distribution. In particular, the cell size distribution should be independent of coverage fraction and follow an exponential distribution.

Propagation of convective activity

As we have already noted at the end of chapter 3, additional research is necessary to determine whether spreading of convective activity via cold pools leads to a phase transition of tropical convection first proposed by *Peters and Neelin* (2006). In fact, additional work is necessary to prove the existence of the phase transition. *Muller et al.* (2009) and *Stechmann and Neelin* (2014), for example, have proposed alternative explanations for the power-law increase in precipitation. We have therefore outlined a test to directly assess the sensitivity of convective activity on the mean atmospheric state in section 3.4. In particular, we propose to turn off radiative cooling and compensating subsidence in an atmospheric model, the mechanisms which have been suggested to drive the atmosphere to the critical point of the phase transition and which prevent us from accessing different parts of the phase transition.

Starting from a state which initially contains convective activity, its dependence on the atmospheric mean state could then be probed by systematically changing a, yet to be defined, control parameter. Note that, for a quantitative comparison with directed percolation, not only the choice of control parameter but also the chosen measure of convective activity, i.e. the order parameter, is important.

If the observed phase transition can be thus reproduced, it still remains to determine whether it is caused by cold pool triggering. This could for example be done by determining how the amount of newly triggered convection depends on the control parameter and tracking whether it originates at cold pool boundaries.

Spatial evolution of self-aggregation

As we have shown in chapter 4, self-aggregation is a coarsening process of moist and dry regions if the positive humidity feedback fulfills two conditions. First, the atmosphere is locally bistable to humidity perturbations and second, the spatial exchange of humidity can be approximated by a diffusive process. While the bistability of the atmosphere with respect to humidity perturbations has been been explicitly shown in simulations (e.g. *Sessions et al.*, 2010), similar evidence for the diffusive interaction term is missing. In fact, studies assessing the contribution of the convergence term show different results. While we expect downgradient transport of humidity from diffusion, and therefore a negative contribution from the convergence term, this only agrees with some studies (*Wing and Emanuel*, 2014; *Coppin and Bony*, 2015). Other studies suggest that the convergence term is, even during the onset of self-aggregation, positive (*Holloway and Woolnough*, 2016).

We propose therefore to test the role of the upgradient moisture transport for self-aggregation. One possibility to assess the importance of lateral humidity transport would be to enforce a diffusive interaction. In particular, one could compensate the moisture advection tendencies by introducing moisture tendencies of equal strength but opposite sign. While this would effectively prevent any horizontal humidity exchange with neighboring cells one could add synthetic moisture tendencies, determined assuming diffusion of a given strength. In case self-aggregation is driven by upscale transport of humidity, this setup should prevent self-aggregation. If self-aggregation is however driven by local processes, this change should not hinder self-aggregation, in fact one could even test whether the width of domain boundaries increases as a function of diffusion strength. A potential problem with this setup, however, is that it might affect not only the developing circulation but also the formation of convection. It thus requires a careful choice of the space and time scales on which the moisture tendencies are canceled.

5.2.2. Convective organization in parametrization schemes

One of the primary aims of this work is to contribute to an improved representation of convection and, in particular, convective organization in climate models If the additional tests described above confirm the applicability of the simple models introduced in this thesis, an important next step will be to include these results into parametrization schemes. While predictions of the modified percolation model for shallow cumulus clouds will mainly affect the radiation parametrization scheme, the discussed properties of deep convection will primarily affect the convection parametrization scheme.

Radiation Parametrization

To include the effect of clustering of shallow cumulus clouds into radiation parametrization schemes one could use the modified percolation model to supply synthetic cloud fields. The model so far only accounts for horizontal distribution though the thickness of the clouds is important for radiative transfer. An important addition to the two-dimensional model introduced in chapter 2 would therefore be to also account for the thickness of the individual cloud cells. Cloud thickness has been found, at least for small clouds, to rapidly increase with cloud size (e.g. *Benner and Curry*, 1998). Assigning cell heights depending on cell size could therefore give a more realistic vertical structure of clouds.

For a full 3D solution of the radiative transfer equation, the horizontal distribution itself is important as, for example, large high clouds could cast shadows which could completely cover neighoring small clouds. For the commonly used 1D radiation schemes the horizontal distribution is, however, only important for the overlap with unconnected higher level clouds. For remnants of high level cloud, for example, the spatial distribution of the low level clouds will affect the overlap and thus the total albedo. While in most radiation parametrization schemes the assumptions about cloud structure and the methods for solving the radiative transfer equation are entwined (*Pincus et al.*, 2003), new schemes are being developed which decouple these two processes and can handle complicated cloud fields and account for overlap with higher level clouds (f.e. *Barker et al.*, 2015).

Convection Parametrization

The results of chapter 3 could have important implications for future convection parametrization, in particular for the sub-grid variability of the convective mass flux. While variability resulting from an exponential cloud cell size distribution has already been included into a convection parametrization scheme (*Plant and Craig*, 2008), the population model suggests that the fluctuations of the total convective mass flux within the grid-cell of a general circulation model are different from fluctuations arising from purely random variability (*Craig and Cohen*, 2006).

The effect of spatial and temporal correlations could be implemented into a convection parametrization by embedding a sub-grid cellular automata model into each model cell as previously shown for example by *Dorrestijn et al.* (2013). In contrast to the cellular automata model introduced in section 3.1.2.4, the probability for the spreading of activity should be determined from the large scale conditions. In particular, having identified the control and order parameter of the underlying continuous phase transition, the probability of triggering new convection in the surrounding of old convective cells should depend on the control parameter and the initial density of activity should be determined from the order parameter. The time evolution of the model could then provide the number of active sites, i.e. the intensity of convection, for the large scale model. Note that as the number of active sites depends on the previous time step and has a stochastic component, two sites under the same large scale conditions could result in very different amounts of convection. The number of active sites should than feed back on the atmospheric mean state, and thus the control parameter, via moisture and temperature tendencies. This is of course only a schematic representation of a new convection parametrization and leaves a number of important questions, like the random seeding of additional convection or the communication between lattices corresponding to different cells of the climate model, unanswered.

5.2.3. Understanding Convection

Apart from improving the representation of convection by including the findings of this thesis into parametrization schemes, how can we proceed to advance our physical understanding of convection? While self-aggregation of convection has been hypothesized to play an important role in determining the properties of the Intertropical Convergence Zone (ITCZ), direct evidence and, in particular, understanding of the contributing mechanisms is still limited.

The convection in the ITCZ has at the same time important similarities and differences to convection observed in the self-aggregated simulations. On the one hand, convection in the ITCZ is also confined to moist regions and surrounded by dry regions, while on the other hand the boundary conditions in the ITCZ are not homogeneous and convection is collocated with highest sea-surface temperatures. While self-aggregation therefore is not the mechanism which organizes convection, the arising question is whether it is important in determining properties like the width and intensity of the highly precipitating regions. To address this question, i.e. to add the effect of spatial inhomogeneity, we can now use a coarsening model, as proposed in chapter 4, and include the inhomogeneity in the boundary conditions as an additional component. In particular, one could combine the model with a model which accounts for the effect of the sea-surface temperature gradient (e.g. *Neggers et al.*, 2007). As self-aggregation has been found to be very sensitive to an increase in sea-surface temperature, understanding its role in determining the properties of the ITCZ might help to understand how the updraft region of one of the most important global circulations will change in a warming climate.

Even more influential, but also more speculative, is the role self-organized criticality could play for our understanding of convection. If convective activity does indeed undergo a continuous phase transition and if the atmosphere is driven to this critical point, long range spatial and temporal correlations emerge from short range interactions. In this thesis we have suggested that the underlying phase transition is in the universality class of directed percolation. As directed percolation has been found to be remarkably robust to details in microscopic dynamics (e.g. *Hinrichsen*, 2006), including, even a rough representation, of these interactions may lead to a significantly more realistic representation of convection.

A. Domain Wall Calculations

The here presented discussion of the domain walls in coarsening is, up to the non-degenerate potential, a short summary of the argument outlined in *Krapivsky et al.* (2010). Assuming that there exists a stationary solution of the one dimensional Time-Dependent Ginzburg-Landau Equation, which consists of the two stable regions q_1 and q_2, separated by a domain wall, Eq. 4.2 reduces to

$$0 = -\frac{\delta V}{\delta q} + D\partial_x^2 q. \tag{A.1}$$

Replacing space (x) with the time (t) and humidity (q) with space (x) in Eq. A.1, leads to an interesting analogy with a virtual particle of mass D moving in a potential $-V$:

$$D\partial_t^2 x = \frac{\delta V}{\delta x}. \tag{A.2}$$

There are now two cases, as shown in Fig. A.1, we must distinguish:

- Degenerate case: depths of both wells in $V(q)$ are identical (left hand side of Fig. A.1)
- Non-degenerate case: Depths of the two wells are different (right hand side of Fig. A.1)

For the first case, a particle of mass D, after having received an infinitely small push, travels from one potential maximum of $-V(x)$, across the potential well, to the other potential maximum, where it comes to rest. In other words, there exists a stationary solution with a domain wall connecting the two stable regions and the shape of this domain wall is given by D and the potential $V(q)$. This has been described in more detail in *Krapivsky et al.* (2010), where they show that the corresponding profile is determined by Eq. 4.5. The width of the barrier width is defined as the "time" it takes to move from $x_2 - \Delta x$ to $x_1 + \Delta x$, where x_2 and x_1 correspond to the right and the left potential maxima in Fig. A.1, respectively and Δx is a small offset. Applying this definition to Eq. 4.5 shows that, at least in the degenerate case, the barrier width is proportional to $\sqrt{D}$.

We will now discuss the non-degenerate case. It is obvious that, if energy is conserved, there is no solution to Eq. A.2 where a particle, initially at rest at either of the maxima of $-V(x)$, comes to rest at the other maxima. This means there is no stationary solution to Eq. A.2

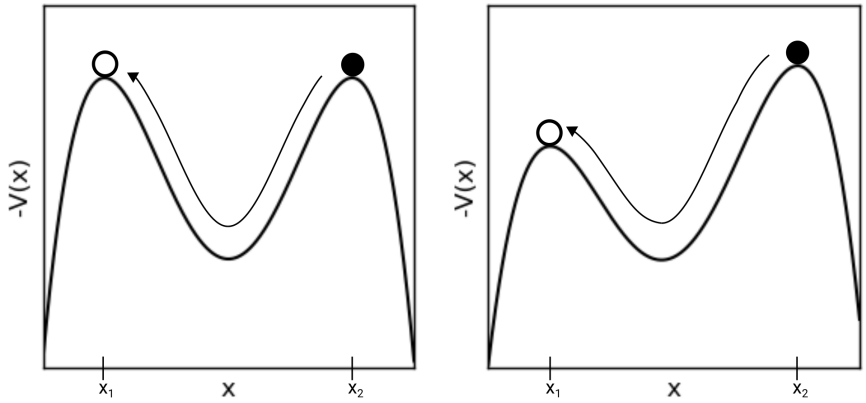

Fig. A.1.: Schematic of the analogy for determining the barrier profile as a function of diffusion strength D. A virtual particle of mass D travels from one potential minima to the other potential minima in a potential with two degenerate minima (left) and non-degenerate minima (right).

in this case. If, however, there is a loss of energy due to friction there is a solution to this problem. Including a friction term into Eq. A.2 leads to

$$D\partial_t^2 x = \frac{\delta V}{\delta x} - k\partial_t x. \tag{A.3}$$

Note that this is the same equation we would get if, instead of assuming a stationary solution, we would assume a solution that does not change its shape but travels at a constant speed k, i.e. $q(x,t) = q(x-kt)$. We thus suggest that, while there is no stationary solution for the second case, there is a solution where the stable solution (the deeper well) invades the metastable solution with constant speed and constant domain wall profile.

While the details of the solution again depend on the potential, can we state how the solution changes with changing diffusion coefficient D? Assuming that, for a given diffusion coefficient D_1, we have a solution, $x_1(t)$, to Eq. A.3, i.e.

$$D_1\partial_t^2 x_1(t) = \frac{\delta V}{\delta x_1} - k_1\partial_t x_1(t). \tag{A.4}$$

where the friction coefficient k_1 is such that the fictive particle comes to rest at the second potential maxima. If we now change D_1 to D_2, without changing the potential, how is the corresponding solution $x_2(t)$ related to $x_1(t)$? Note that, as we are still looking for a solution where the fictive particle travels to the second potential maxima, we expect that the friction coefficient will also change. The solution $x_2(t)$ again fulfills Eq. A.3:

$$D_2\partial_t^2 x_2(t) = \frac{\delta V}{\delta x_2} - k_2\partial_t x_2(t). \tag{A.5}$$

Rescaling time by a factor $\sqrt{D_1/D_2}$, i.e. $\tilde{t} = \sqrt{D_1/D_2}t$, Eq. A.5 can be written as

$$D_1\partial_{\tilde{t}}^2 x_2(\tilde{t}/\sqrt{D_1/D_2}) = \frac{\delta V}{\delta x_2} - \sqrt{D_1/D_2}k_2\partial_{\tilde{t}}x_2(\tilde{t}/\sqrt{D_1/D_2}) \tag{A.6}$$

and renaming $\tilde{t}$ as t yields

$$D_1\partial_t^2 x_2(t/\sqrt{D_1/D_2}) = \frac{\delta V}{\delta x_2} - \sqrt{D_1/D_2}k_2\partial_t x_2(t/\sqrt{D_1/D_2}). \tag{A.7}$$

Comparison with Eq. A.4 shows that $x_2(t/\sqrt{D_1/D_2}) = x_1(t)$ is a solution to Eq. A.7 with $k_2 = k_1/\sqrt{D_1/D_2}$.

We thus find that a change in diffusion coefficient leads to a rescaling of the original solution and a change in friction coefficient. The rescaling will affect the barrier width and the propagation speed (friction coefficient). In particular, if the barrier width in x_1 is given by Δt_1, remember that we have exchanged x and t for our analogy, the barrier width in x_2 is given by $\Delta t_2 = \Delta t_1/\sqrt{D_1/D_2}$, i.e. $\Delta t \sim \sqrt{D}$, and the ratio of the propagation speeds is $k_1/k_2 = \sqrt{D_1/D_2}$, i.e. $k \sim \sqrt{D}$. To summarize, we find that the barrier width is still proportional to $\sqrt{D}$, as in the degenerate case, but that now there is a propagation into the metastable state at a speed k, also proportional to $\sqrt{D}$. While the scaling of the barrier width is tested for the three models in the main part of the thesis, see Fig. 4.10, the corresponding scaling of the propagation speed is shown in Fig. A.2.

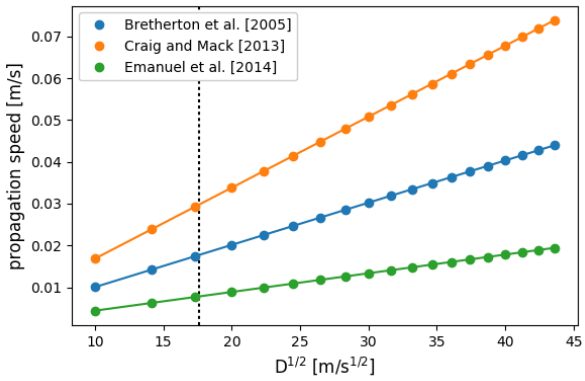

Fig. A.2.: Test scaling hypothesis for propagation speed for three different models (dots) and corresponding fits (line). The black dotted line marks the diffusion coefficient determined in section 4.3.

B. Parameter estimation for *Emanuel et al.* (2014)

We use the mean annual West Indies sounding data for isobaric surfaces obtained by *Jordan* (1958) to estimate the necessary parameters for the model based on *Emanuel et al.* (2014). Choosing the heights of the two layers as $H_1 = 6$ km and $H_2 = 12$ km, the first layer is located within the lower troposphere, while the second layer is in the upper troposphere, as sketched in Fig. (1) in *Emanuel et al.* (2014). Evaluating the temperature and density soundings, shown in Fig. B.1, at $z = 6$ km and $z = 12$ km, gives the values $T_1 = 264.7$ K, $T_2 = 220.4$ K, $\rho_1 = 0.647\,\mathrm{kg\,m^{-3}}$ and $\rho_2 = 0.333\,\mathrm{kg\,m^{-3}}$.

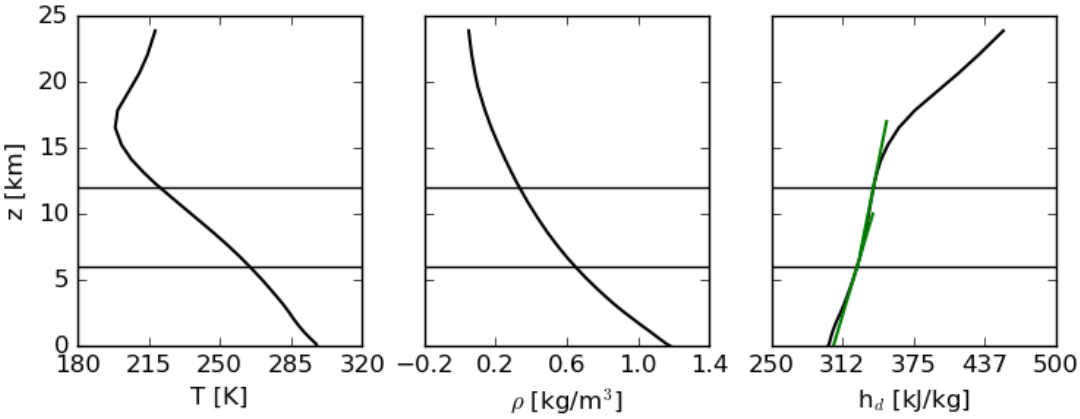

Fig. B.1.: Mean annual West Indies sounding of temperature (left), density (middle) and dry static energy (right) determined from *Jordan* (1958).

To estimate the dry static stability we first need to calculate the dry static energy as a function of height z. The dry static energy is given by

$$h_d(z) = c_p T(z) + gz \tag{B.1}$$

where c_p is the specific heat capacity of air at constant pressure and g is the gravitational acceleration. Using the temperature profile used above, the calculated profile of $h_d(z)$ is also

shown in Fig. B.1. Determining the gradient at the two height levels, gives the following estimates for the dry static stability: $S_1 = 3.5\,\mathrm{J\,K^{-1}\,m^{-1}}$ and $S_2 = 2.3\,\mathrm{J\,K^{-1}\,m^{-1}}$.

In addition we need to estimate how the emissivity in the upper model layer depends on the humidity within this layer ($\partial_{q_2}\epsilon_2$). To this end we use Eq. 28 from *Emanuel et al.* (2014):

$$\frac{\partial \dot{Q}_2}{\partial q_2} = \frac{\bar{\dot{Q}}_2}{\epsilon_2}\frac{\partial \epsilon_2}{\partial q_2} \tag{B.2}$$

and solve it for $\partial_{q_2}\epsilon_2$ and approximate each term separately:

$$\frac{\partial \epsilon_2}{\partial q_2} = \frac{\partial \dot{Q}_2}{\partial q_2}\frac{\epsilon_2}{\bar{\dot{Q}}_2} \tag{B.3}$$

$$\approx \left(\frac{\Delta \dot{Q}_2}{\dot{Q}_2}\right)\left(\frac{q_2}{\Delta q_2}\right)\frac{\epsilon_2}{q_2} \tag{B.4}$$

$$\tag{B.5}$$

We estimate the first two terms on the right from Fig. 5 in *Emanuel et al.* (2014), where a reduction of the humidity (initially close to saturation) by 20% ($q_2/\Delta q_2 \approx 1.0/0.2$), leads to a radiative cooling perturbation ($\Delta\dot{Q}_2$) of approximately $0.1\,\mathrm{K\,d^{-1}}$. Assuming standard values for the mean radiative cooling over tropical oceans of $\dot{Q}_2 \approx 2\,\mathrm{K\,d^{-1}}$ (e.g. *Tompkins and Craig*, 1998), the mean emissivity of the upper troposphere of $\epsilon_2 \approx 0.3$ (*Pierrehumbert*, 2010) and the specific humidity of approximately $q_2 \approx 1 \times 10^{-4}\,\mathrm{kg\,kg^{-1}}$ (*Jordan*, 1958). The resulting estimate for $\partial_{q_2}\epsilon_2$ is 750.

Finally we estimate ϵ_p which, as noted by *Emanuel et al.* (2014), is related to a bulk precipitation efficiency. Assuming $\epsilon_p = 1.1 \cdot q_{RCE}$, the relationship between precipitation efficiency and relative humidity proposed by *Craig and Mack* (2013), and setting $q_{RCE} = 0.72$ (*Bretherton et al.*, 2005) yields $\epsilon_p \approx 0.8$.

Nomenclature

Acronyms

AS	Absorbing state
CA	Cellular automaton
CAPE	Convective available potential energy
CIN	Convective inhibition
GOES	Geostationary Operational Environmental Satellite
ITCZ	Intertropical Convergence Zone
LFC	Level of free convection
LNB	Level of neutral buoyancy
MCS	Mesoscale Convective System
PDF	Probability density function
RCE	Radiative-convective equilibrium
RDF	Radial distribution function
SA	Self-aggregation
SST	Sea surface temperature
TDGL	Time-Dependent Ginzburg-Landau Equation
WTG	Weak-temperature gradient
WVP	Column integrated water vapor path

Greek Symbols

α	Subsidence rate

α_h	Fit parameter for moisture convergence term (*Bretherton et al.*, 2005)
β	Critical exponent
β_p	Fit parameter for precipitation efficiency term (*Craig and Mack*, 2013)
ϵ	Dissipation rate
ϵ_1, ϵ_2	Lower and upper level longwave emissivity (*Emanuel et al.*, 2014)
ϵ_p	Ratio of updraft to total mass-flux
Γ	Circular integration path
λ	Fit parameter for convective moistening term (*Craig and Mack*, 2013)
ϕ	Spatial distribution function of humidity increase
ρ_1, ρ_2	Lower and upper level density (*Emanuel et al.*, 2014)
ρ_a	Density of active sites
σ	Standard deviation
τ	Critical exponent
τ_{lt}	Cold pool life time
Θ_v	Virtual potential temperature
ζ	Particle density

Roman Symbols

A	Total area covered by clouds
a, b, c	Fit parameter according to *Ding et al.* (2014)
A^{moist}	Area of moist region in self-aggregation
A_c^{moist}	Critical area of the moist region A^{moist}
a_m	Scaling parameter for precipitation-humidity dependence (*Bretherton et al.*, 2005)
b_m	Scaling parameter for precipitation-humidity dependence (*Craig and Mack*, 2013)

C	Cross-correlation function
c_s, c_r	Constants of proportionality for increase of surface flux and radiative forcing (*Bretherton et al.*, 2005)
c_{11}, c_{12}, c_{21}, c_{22}	Linearization coefficients introduced by *Emanuel et al.* (2014)
cs	Clustering strength
cw	Clustering width
D	Diffusion coefficient
d	Dimension
F	Landau Free Energy
f^{PDF}	Two-dimensional probability density function
h	External driving rate
H_1, H_2	Lower and upper model level (*Emanuel et al.*, 2014)
I_v	Vertically integrated free tropospheric moisture content
I_v^*, I_v^{RCE}	Saturation value of I_v, RCE value of I_v
L	Domain length
L_v	Latent heat of vaporization
l_{cor}	Auto-correlation length
M	Number of potential sites for new clouds (or new plants)
N	Number of cloud disks
n	Average number of clouds per time and area
n_0	Average number of clouds per time and area at q_{RCE}
n_1	Additional number of clouds per time, area and Δq at $q_{RCE} + \Delta q$
N_f	Fixed number clouds (or plants)
n_s	Cluster size distribution
P	Precipitation strength

p, p_c	Probability for a site to be occupied (isotropic percolation) or open (directed percolation), Critical probability
$\tilde{p}$	Fraction of triggered clouds (or surviving plants in the weed population model)
P_s	Strength of the percolating cluster
P_{RCE}	Horizontal mean radiative-convective equilibrium rain rate
q	Generic scalar (humidity) field
q'	Deviation of q from q_{RCE}
q_0	Total humidity increase due to one cloud
q_1, q_2	Respective values of q at the two potential minima of V
q_1', q_2'	Deviation of q_1 and q_2 from q_1^{RCE} and q_2^{RCE}
q_1^{RCE}, q_2^{RCE}	Radiative-convective equilibrium values of q_1 and q_2
q_{RCE}	Radiative-convective equilibrium value of q
R	Local interaction term of Reaction-Diffusion Equation
r	Radial distance
r^d, r_m^d	Disk radius, mean disk radius
r^{hum}, r_{RCE}^{hum}	Column relative humidity, Column relative humidity of RCE state
r_h^{hum}	Fit parameter for moisture convergence term (*Bretherton et al.*, 2005)
R_B, R_C, R_E	R for model based on *Bretherton et al.* (2005), *Craig and Mack* (2013), *Emanuel et al.* (2014)
r_{cp}	Cold pool radius
r_{fp}	Radius of humidity footprint
s	Cluster size
s^d, s_m^d	Disk area, mean area of disks
S_1, S_2	Lower and upper level dry static stability (*Emanuel et al.*, 2014)
T_1, T_2	Lower and upper level temperature (*Emanuel et al.*, 2014)

t_d	Time at which cold pool is first detected
V	Double well potential
w, w_c	Column integrated water vapor, Critical column integrated water vapor
W_*	Saturation water-vapor-path
x, y	Horizontal coordinates
z	Height

Bibliography

Andrade, R. F. S., H. J. Schellnhuber, and M. Claussen (1998), Analysis of rainfall records: possible relation to self-organized criticality, *Physica A*, *254*, 557–568, doi:10.1016/S0378-4371(98)00057-0.

Arakawa, A., and W. H. Schubert (1974), Interaction of a cumulus cloud ensemble with the large-scale environment, Part I, *J. Atmos. Sci.*, *31*, 674–701, doi:10.1175/1520-0469(1974)031<0674:IOACCE>2.0.CO;2.

Barker, H. W., J. N. S. Cole, and J. Li (2015), Application of a Monte Carlo solar radiative transfer model in the McICA framework, *Q. J. R. Meteorol. Soc.*, *141*, 3130–3139, doi:10.1002/qj.2597.

Bengtsson, L., H. Körnich, E. Källén, and G. Svensson (2011), Large-Scale Dynamical Response to Subgrid-Scale Organization Provided by Cellular Automata, *J. Atmos. Sci.*, *68*, 3132–3144, doi:10.1175/JAS-D-10-05028.1.

Benner, T. C., and J. A. Curry (1998), Characteristics of small tropical cumulus clouds and their impact on the environment, *J. Geophys. Res.*, *103*, 28,753–28,767, doi:10.1029/98JD02579.

Böing, S. (2016), An object-based model for convective cold pool dynamics, *Math. Clim. Weather Forecast.*, *2*, 43–60, doi:10.1515/mcwf-2016-0003.

Bony, S., B. Stevens, D. M. W. Frierson, C. Jakob, M. Kageyama, R. Pincus, T. G. Shepherd, S. C. Sherwood, A. P. Siebesma, A. H. Sobel, M. Watanabe, and M. J. Webb (2015), Clouds, circulation and climate sensitivity, *Nat. Geosci.*, *8*, 261–268, doi:10.1038/ngeo2398.

Bretherton, C. S., and P. K. Smolarkiewicz (1989), Gravity Waves, Compensating Subsidence and Detrainment around Cumulus Clouds, *J. Atmos. Sci.*, *46*, 740–759, doi:10.1175/1520-0469(1989)046<0740:GWCSAD>2.0.CO;2.

Bretherton, C. S., M. E. Peters, and L. E. Back (2004), Relationships between water vapor path and precipitation over the tropical oceans, *J. Clim.*, *17*, 1517–1528, doi:10.1175/1520-0442(2004)017<1517:RBWVPA>2.0.CO;2.

Bretherton, C. S., P. N. Blossey, and M. Khairoutdinov (2005), An Energy-Balance Analysis of Deep Convective Self-Aggregation above Uniform SST, *J. Atmos. Sci.*, *62*, 4273–4292, doi:10.1175/JAS3614.1.

Broeker, H. M., and P. Grassberger (1999), SOC in a population model with global control, *Phys. A Stat. Mech. its Appl.*, *267*, 453–470, doi:10.1016/S0378-4371(99)00042-4.

Byers, H. R., and R. R. Braham (1949), The Thunderstorm: Report of the Thunderstorm Project (a joint project of four U.S. Government Agencies : Air Force, Navy, National Advisory Committee for Aeronautics, and Weather Bureau), *Tech. rep.*, Washington, D.C., doi:10.1002/qj.49707733225.

Cahalan, R. F., and J. H. Joseph (1989), Fractal Statistics of Cloud Fields, *Mon. Weather Rev.*, *117*, 261–272, doi:10.1175/1520-0493(1989)117<0261:FSOCF>2.0.CO;2.

Cahalan, R. F., W. Ridgway, W. J. Wiscombe, T. L. Bell, and J. B. Snider (1994), The Albedo of Fractal Stratocumulus Clouds, *J. Atmos. Sci.*, *51*, 2434–2455, doi:10.1175/1520-0469(1994)051<2434:TAOFSC>2.0.CO;2.

Chandrasekhar, S. (1943), Stochastic problems in physics and astronomy, *Rev. Mod. Phys.*, *15*, 1–89, doi:10.1103/RevModPhys.15.1.

Chen, S. S., R. A. Houze, B. E. Mapes, S. S. Chen, R. A. H. Jr., and B. E. Mapes (1996), Multiscale Variability of Deep Convection In Realation to Large-Scale Circulation in TOGA COARE, *J. Atmos. Sci.*, *53*, 1380–1409, doi:10.1175/1520-0469(1996)053<1380:MVODCI>2.0.CO;2.

Chopard, B., and M. Droz (1998), *Cellular Automata Modeling of Physical Systems*, Cambridge University Press, Cambridge, doi:10.1017/CBO9780511549755.

Cohen, B. G., and G. C. Craig (2004), The response time of a convective cloud ensemble to a change in forcing, *Q. J. R. Meteorol. Soc.*, *130*, 933–944, doi:10.1256/qj.02.218.

Cohen, B. G., and G. C. Craig (2006), Fluctuations in an Equilibrium Convective Ensemble. Part II: Numerical Experiments, *J. Atmos. Sci.*, *63*, 2005–2015, doi:10.1175/JAS3710.1.

Cooper, N., A. Tedder, D. M. Heyes, and J. R. Melrose (1989), Percolation cluster statistics of 2D Lennard-Jones phases, *J. Phys. Condens. Matter*, *1*, 6217–6230, doi:10.1088/0953-8984/1/35/020.

Coppin, D., and S. Bony (2015), Physical mechanisms controlling the initiation of convective self-aggregation in a General Circulation Model, *J. Adv. Model. Earth Syst.*, *7*, 2060–2078, doi:10.1002/2015MS000571.

Craig, G. C., and B. G. Cohen (2006), Fluctuations in an Equilibrium Convective Ensemble. Part I: Theoretical Formulation, *J. Atmos. Sci.*, *63*, 1996–2004, doi:10.1175/JAS3709.1.

Craig, G. C., and J. M. Mack (2013), A coarsening model for self-organization of tropical convection, *J. Geophys. Res. Atmos.*, *118*, 8761–8769, doi:10.1002/jgrd.50674.

Cruz, C. P. T., M. L. Lyra, U. L. Fulco, and G. Corso (2012), Critical behavior of the absorbing state transition in the contact process with relaxing immunization, *Phys. A Stat. Mech. its Appl.*, *391*, 5349–5354, doi:10.1016/j.physa.2012.05.066.

Dawe, J. T., and P. H. Austin (2012), Statistical analysis of an LES shallow cumulus cloud ensemble using a cloud tracking algorithm, *Atmos. Chem. Phys.*, *12*, 1101–1119, doi:10.5194/acp-12-1101-2012.

de Souza, D. R., and T. Tomé (2010), Stochastic lattice gas model describing the dynamics of the SIRS epidemic process, *Phys. A Stat. Mech. its Appl.*, *389*(5), 1142–1150, doi:10.1016/j.physa.2009.10.039.

Derbyshire, S., I. Beau, P. Bechtold, J.-Y. Grandpeix, J.-M. Piriou, J.-L. Redelsperger, and P. Soares (2004), Sensitivity of moist convection to environmental humidity, *Q. J. R. Meteorol. Soc.*, *130*, 3055–3079, doi:10.1256/qj.03.130.

Dickman, R., M. A. Muñoz, A. Vespignani, and S. Zapperi (2000), Paths to self-organized criticality, *Brazilian J. Phys.*, *30*, 27–41, doi:10.1590/S0103-97332000000100004.

Ding, B., C. Li, M. Zhang, G. Lu, and F. Ji (2014), Numerical analysis of percolation cluster size distribution in two-dimensional and three-dimensional lattices, *Eur. Phys. J. B*, *87*, 1–8, doi:10.1140/epjb/e2014-40996-4.

Dorrestijn, J., D. T. Crommelin, J. A. Biello, and S. J. Böing (2013), A data-driven multi-cloud model for stochastic parametrization of deep convection, *Philos. Trans. A. Math. Phys. Eng. Sci.*, *371*, 1–19, doi:10.1098/rsta.2012.0374.

Duckers, L., and R. Ross (1974), Percolation with non-random site occupation, *Phys. Lett. A*, *49*, 361–362, doi:10.1016/0375-9601(74)90270-9.

Einstein, A. (1905), Über die von der molekularkinetischen Theorie der Wärme geforderte Bewegung von in ruhenden Flüssigkeiten suspendierten Teilchen, *Ann. Phys.*, *322*, 549–560, doi:10.1002/andp.19053220806.

Emanuel, K., A. A. Wing, and E. M. Vincent (2014), Radiative-convective instability, *J. Adv. Model. Earth Syst.*, *6*, 75–90, doi:10.1002/2013MS000270.

Emanuel, K. A., J. D. Neelin, and C. S. Bretherton (1994), On large-scale circulations in convecting atmospheres, *Q. J. R. Meteorol. Soc.*, *120*, 1111–1143, doi:10.1002/qj.49712051902.

Gould, H., J. Tobochnik, and C. Wolfgang (2005), Percolation, in *An Introd. to Comput. Simul. Methods Appl. to Phys. Syst.*, 3. ed., pp. 445–483, Addison-Wesley Longman Publishing Co., Inc., Boston, MA, USA.

Held, I. M., R. S. Hemler, and V. Ramaswamy (1993), Radiative-Convective Equilibrium with Explicit Two-Dimensional Moist Convection, *J. Atmos. Sci.*, *50*, 3909–3927, doi:10.1175/1520-0469(1993)050<3909:RCEWET>2.0.CO;2.

Henkel, M., and M. Pleimling (2010), *Non-Equilibrium Phase Transitions Volume 2: Ageing and Dynamical Scaling Far from Equilibrium*, Theoretical and Mathematical Physics, Springer Netherlands, Dordrecht, doi:10.1007/978-90-481-2869-3.

Heus, T., and A. Seifert (2013), Automated tracking of shallow cumulus clouds in large domain, long duration large eddy simulations, *Geosci. Model Dev.*, *6*, 1261–1273, doi:10.5194/gmd-6-1261-2013.

Hinrichsen, H. (2006), Non-equilibrium phase transitions, *Phys. A Stat. Mech. its Appl.*, *369*, 1–28, doi:10.1016/j.physa.2006.04.007.

Hohenegger, C., and B. Stevens (2016), Coupled radiative convective equilibrium simulations with explicit and parameterized convection, *J. Adv. Model. Earth Syst.*, *8*, 1468–1482, doi:10.1002/2016MS000666.

Holloway, C. E., and J. D. Neelin (2009), Moisture vertical structure, column water vapor, and tropical deep convection, *J. Atmos. Sci.*, *66*, 1665–1683, doi:10.1175/2008JAS2806.1.

Holloway, C. E., and S. J. Woolnough (2016), The sensitivity of convective aggregation to diabatic processes in idealized radiative-convective equilibrium simulations, *J. Adv. Model. Earth Syst.*, *8*, 166–195, doi:10.1002/2015MS000511.

Hoshen, J., D. Stauffer, G. H. Bishop, R. J. Harrison, and G. D. Quinn (1979), Monte Carlo experiments on cluster size distribution in percolation, *J. Phys. A. Math. Gen.*, *12*, 1285–1307, doi:10.1088/0305-4470/12/8/022.

Houze Jr, R. A. (1993), *Cloud Dynamics*, 1. ed., 573 pp., Academic Press Inc., San Diego, doi:10.1016/S0074-6142(08)62859-4.

Houze Jr, R. A. (2004), Mesoscale Convective Systems, *Rev. Geophys.*, *42*, 1–43, doi:10.1029/2004RG000150.

Hozumi, K., T. Harimaya, and C. Magono (1982), The Size Distribution of Cumulus Clouds as a Function of Cloud Amount, *J. Meteorol. Soc. Japan. Ser. II*, *60*, 691–699, doi:10.2151/jmsj1965.60.2_691.

Jeevanjee, N., and D. M. Romps (2013), Convective self-aggregation, cold pools, and domain size, *Geophys. Res. Lett.*, *40*, 994–998, doi:10.1002/grl.50204.

Jordan, C. L. (1958), Mean Soundings for the West Indies Area, *J. Meteorol.*, *15*, 91–97, doi:10.1175/1520-0469(1958)015<0091:MSFTWI>2.0.CO;2.

Kempf, A. (2013), Investigation of Self-Aggregation of Tropical Convection, Master thesis, Ludwig-Maximilians Universität München.

Kempf, A. (2014), Testing a Phase Transition Theory for Convective Organisation, Master thesis, Ludwig-Maximilians Universität München.

Khairoutdinov, M., and K. Emanuel (2010), Aggregated Convection and the Regulation of Tropical Climate, in *29th Conf. Hurricanes Trop. Meteorol.*, American Meteorological Society, Tucson.

Khouider, B., J. Biello, and A. J. Majda (2010), A stochastic multicloud model for tropical convection, *Commun. Math. Sci.*, *8*, 187–216, doi:10.4310/CMS.2010.v8.n1.a10.

Krapivsky, P. L., S. Redner, and E. Ben-Naim (2010), *A Kinetic View of Statistical Physics*, 488 pp., Cambridge University Press, Cambridge, doi:10.1017/CBO9780511780516.

Kuo, K.-S., R. M. Welch, R. C. Weger, M. A. Engelstad, and S. K. Sengupta (1993), The three-dimensional structure of cumulus clouds over the ocean: 1. Structural analysis, *J. Geophys. Res.*, *98*, 20,685–20,711, doi:10.1029/93JD02331.

LeMone, M. A., and E. J. Zipser (1980), Cumulonimbus Vertical Velocity Events in GATE. Part I: Diameter, Intensity and Mass Flux, *J. Atmos. Sci.*, *37*, 2444–2457, doi:10.1175/1520-0469(1980)037<2444:CVVEIG>2.0.CO;2.

López, R. E. (1977), The Lognormal Distribution and Cumulus Cloud Populations, *Mon. Weather Rev.*, *105*, 865–872, doi:10.1175/1520-0493(1977)105<0865:TLDACC>2.0.CO;2.

Machado, L. A. T., and W. B. Rossow (1993), Structural Characteristics and Radiative Properties of Tropical Cloud Clusters, doi:10.1175/1520-0493(1993)121<3234:SCARPO>2.0.CO;2.

Majda, A. J., and B. Khouider (2002), Stochastic and mesoscopic models for tropical convection., *Proc. Natl. Acad. Sci. U. S. A.*, *99*, 1123–1128, doi:10.1073/pnas.032663199.

Mapes, B., and R. Neale (2011), Parameterizing Convective Organization to Escape the Entrainment Dilemma, *J. Adv. Model. Earth Syst.*, *3*, M06,004, doi:10.1029/2011MS000042.

Mapes, B. E. (1993), Gregarious Tropical Convection, *J. Atmos. Sci.*, *50*, 2026–2037, doi:10.1175/1520-0469(1993)050<2026:GTC>2.0.CO;2.

Martin, H. O., E. V. Albano, and A. L. Maltz (1987), Percolation with diffusion of particles with attractive interactions, *J. Phys. A. Math. Gen.*, *20*, 1531–1542, doi:10.1088/0305-4470/20/6/035.

Mertens, S., and C. Moore (2012), Continuum percolation thresholds in two dimensions, *Phys. Rev. E - Stat. Nonlinear, Soft Matter Phys.*, *86*, 061,109, doi:10.1103/PhysRevE.86.061109.

Muller, C., and S. Bony (2015), What favors convective aggregation and why?, *Geophys. Res. Lett.*, *42*, 5626–5634, doi:10.1002/2015GL064260.

Muller, C. J., and I. M. Held (2012), Detailed Investigation of the Self-Aggregation of Convection in Cloud-Resolving Simulations, *J. Atmos. Sci.*, *69*, 2551–2565, doi:10.1175/JAS-D-11-0257.1.

Muller, C. J., L. E. Back, P. A. O'Gorman, and K. A. Emanuel (2009), A model for the relationship between tropical precipitation and column water vapor, *Geophys. Res. Lett.*, *36*, L16,804, doi:10.1029/2009GL039667.

Nair, U. S., R. C. Weger, K. S. Kuo, and R. M. Welch (1998), Clustering, randomness, and regularity in cloud fields: 5. The nature of regular cumulus cloud fields, *J. Geophys. Res.*, *103*, 11,363–11,380, doi:10.1029/98JD00088.

Neggers, R. A. J., H. J. J. Jonker, and A. P. Siebesma (2003), Size Statistics of Cumulus Cloud Populations in Large-Eddy Simulations, *J. Atmos. Sci.*, *60*, 1060–1074, doi:10.1175/1520-0469(2003)60<1060:SSOCCP>2.0.CO;2.

Neggers, R. A. J., J. D. Neelin, and B. Stevens (2007), Impact mechanisms of shallow cumulus convection on tropical climate dynamics, *J. Clim.*, *20*, 2623–2642, doi:10.1175/JCLI4079.1.

Parsons, D. B., K. Yoneyama, and J.-L. Redelsperger (2000), The evolution of the tropical western Pacific atmosphere-ocean system following the arrival of a dry intrusion, *Q. J. R. Meteorol. Soc.*, *126*, 517–548, doi:10.1002/qj.49712656307.

Peters, O., and J. D. Neelin (2006), Critical phenomena in atmospheric precipitation, *Nat. Phys.*, *2*, 393–396, doi:10.1038/nphys314.

Peters, O., C. Hertlein, and K. Christensen (2001), A Complexity View of Rainfall, *Phys. Rev. Lett.*, *88*, 018,701, doi:10.1103/PhysRevLett.88.018701.

Peters, O., J. D. Neelin, and S. W. Nesbitt (2009), Mesoscale Convective Systems and Critical Clusters, *J. Atmos. Sci.*, *66*, 2913–2924, doi:10.1175/2008JAS2761.1.

Peters, O., A. Deluca, A. Corral, J. D. Neelin, and C. E. Holloway (2010), Universality of rain event size distributions, *J. Stat. Mech. Theory Exp.*, *2010*, P11,030, doi:10.1088/1742-5468/2010/11/P11030.

Pierrehumbert, R. T. (2010), *Principles of Planetary Climate*, 652 pp., Cambridge University Press, Cambridge, doi:10.1017/CBO9780511780783.

Pincus, R., H. W. Barker, and J.-J. Morcrette (2003), A fast, flexible, approximate technique for computing radiative transfer in inhomogeneous cloud fields, *J. Geophys. Res. Atmos.*, *108(D13)*, 4376, doi:10.1029/2002JD003322,.

Plank, V. G. (1969), The Size Distribution of Cumulus Clouds in Representative Florida Populations, *J. Appl. Meteorol.*, *8*, 46–67, doi:10.1175/1520-0450(1969)008<0046:TSDOCC>2.0.CO;2.

Plant, R. S., and G. C. Craig (2008), A Stochastic Parameterization for Deep Convection Based on Equilibrium Statistics, *J. Atmos. Sci.*, *65*, 87–105, doi:10.1175/2007JAS2263.1.

Popke, D., B. Stevens, and A. Voigt (2013), Climate and climate change in a radiative-convective equilibrium version of ECHAM6, *J. Adv. Model. Earth Syst.*, *5*(1), 1–14, doi:10.1029/2012MS000191.

Posselt, D. J., S. van den Heever, G. Stephens, and M. R. Igel (2012), Changes in the Interaction between Tropical Convection, Radiation, and the Large-Scale Circulation in a Warming Environment, *J. Clim.*, *25*, 557–571, doi:10.1175/2011JCLI4167.1.

Pruessner, G. (2012), *Self-Organised Criticality: Theory, Models and Characterisation*, 494 pp., Cambridge University Press, Cambridge, doi:10.1017/CBO9780511977671.

Purdom, J. F. W. (1976), Some Uses of High-Resolution GOES Imagery in the Mesoscale Forecasting of Convection and Its Behavior, *Mon. Weather Rev.*, *104*, 1474–1483, doi:10.1175/1520-0493(1976)104<1474:SUOHRG>2.0.CO;2.

Quaas, J. (2012), Evaluating the "critical relative humidity" as a measure of subgrid-scale variability of humidity in general circulation model cloud cover parameterizations using satellite data, *J. Geophys. Res. Atmos.*, *117*, D09,208, doi:10.1029/2012JD017495.

Rauber, R. M., H. T. Ochs, L. Di Girolamo, S. Göke, E. Snodgrass, B. Stevens, C. Knight, J. B. Jensen, D. H. Lenschow, R. A. Rilling, D. Rogers, J. L. Stith, B. A. Albrecht, P. Zuidema, A. M. Blyth, C. W. Fairall, W. A. Brewer, S. Tucker, S. G. Lasher-Trapp, O. L. Mayol-Bracero, G. Vali, B. Geerts, J. R. Anderson, B. A. Baker, R. P. Lawson, A. R. Bandy, D. C. Thornton, E. Burnet, J. Brenguier, L. Gomes, P. R. Brown, P. Chuang, W. R. Cotton, H. Gerber, B. G. Heikes, J. G. Hudson, P. Kollias, S. K. Krueger, L. Nuijens, D. W. O'Sullivan, A. P. Siebesma, and C. H. Twohy (2007), Rain in shallow cumulus over the ocean: The RICO campaign, *Bull. Am. Meteorol. Soc.*, *88*, 1912–1928, doi:10.1175/BAMS-88-12-1912.

Redelsperger, J.-L., D. B. Parsons, and F. Guichard (2002), Recovery Processes and Factors Limiting Cloud-Top Height following the Arrival of a Dry Intrusion Observed during TOGA COARE, *J. Atmos. Sci.*, *59*, 2438–2457, doi:10.1175/1520-0469(2002)059<2438:RPAFLC>2.0.CO;2.

Sasidevan, V. (2013), Continuum percolation of overlapping disks with a distribution of radii having a power-law tail, *Phys. Rev. E - Stat. Nonlinear, Soft Matter Phys.*, *88*, 022,140, doi:10.1103/PhysRevE.88.022140.

Scheufele, K. (2014), Resolution dependence of cumulus statistics in radiative-convective equilibrium, Phd thesis, Ludwig-Maximilians Universität München.

Schlemmer, L., and C. Hohenegger (2014), The Formation of Wider and Deeper Clouds as a Result of Cold-Pool Dynamics, *J. Atmos. Sci.*, *71*, 2842–2858, doi:10.1175/JAS-D-13-0170.1.

Seifert, A., and T. Heus (2013), Large-eddy simulation of organized precipitating trade wind cumulus clouds, *Atmos. Chem. Phys.*, *13*, 5631–5645, doi:10.5194/acp-13-5631-2013.

Sengupta, S. K., R. M. Welch, M. S. Navar, T. A. Berendes, and D. W. Chen (1990), Cumulus Cloud Field Morphology and Spatial Patterns Derived from High Spatial Resolution Landsat Imagery, *J. Appl. Meteorol.*, *29*, 1245–1267, doi:10.1175/1520-0450(1990)029<1245:CCFMAS>2.0.CO;2.

Sessions, S. L., S. Sugaya, D. J. Raymond, and A. H. Sobel (2010), Multiple equilibria in a cloud-resolving model using the weak temperature gradient approximation, *J. Geophys. Res.*, *115*, D12,110, doi:10.1029/2009JD013376.

Sessions, S. L., M. J. Herman, and S. Sentić (2015), Convective response to changes in the thermodynamic environment in idealized weak temperature gradient simulations, *J. Adv. Model. Earth Syst.*, *7*, 712–738, doi:10.1002/2015MS000446.

Sessions, S. L., S. Sentić, and M. J. Herman (2016), The role of radiation in organizing convection in weak temperature gradient simulations, *J. Adv. Model. Earth Syst.*, *8*, 244–271, doi:10.1002/2015MS000587.

Sethna, J. P. (2006), *Statistical Mechanics: Entropy, Order Parameters and Complexity*, 376 pp., Oxford University Press, Oxford.

Shante, V. K., and S. Kirkpatrick (1971), An introduction to percolation theory, *Adv. Phys.*, *20*, 325–357, doi:10.1080/00018737100101261.

Slingo, A., and J. M. Slingo (1988), The response of a general circulation model to cloud longwave radiative forcing. I: Introduction and initial experiments, *Q. J. R. Meteorol. Soc.*, *114*, 1027–1062, doi:10.1002/qj.49711448209.

Sobel, A. H., G. Bellon, and J. Bacmeister (2007), Multiple equilibria in a single-column model of the tropical atmosphere, *Geophys. Res. Lett.*, *34*, L22,804, doi:10.1029/2007GL031320.

Stauffer, D., and A. Aharony (1994), *Introduction to Percolation Theory*, 2. ed., 192 pp., CRC Press, Boca Raton.

Stechmann, S. N., and J. D. Neelin (2014), First-Passage-Time Prototypes for Precipitation Statistics, *J. Atmos. Sci.*, *71*, 3269–3291, doi:10.1175/JAS-D-13-0268.1.

Stephan, C. C., M. J. Alexander, M. Hedlin, C. D. de Groot-Hedlin, and L. Hoffmann (2016), A Case Study on the Far-Field Properties of Propagating Tropospheric Gravity Waves, *Mon. Weather Rev.*, *144*, 2947–2961, doi:10.1175/MWR-D-16-0054.1.

Stevens, B. (2005), Atmospheric Moist Convection, *Annu. Rev. Earth Planet. Sci.*, *33*, 605–643, doi:10.1146/annurev.earth.33.092203.122658.

Tobin, I., S. Bony, and R. Roca (2012), Observational evidence for relationships between the degree of aggregation of deep convection, water vapor, surface fluxes, and radiation, *J. Clim.*, *25*, 6885–6904, doi:10.1175/JCLI-D-11-00258.1.

Tobin, I., S. Bony, C. E. Holloway, J.-Y. Grandpeix, G. Sèze, D. Coppin, S. J. Woolnough, and R. Roca (2013), Does convective aggregation need to be represented in cumulus parameterizations?, *J. Adv. Model. Earth Syst.*, *5*, 692–703, doi:10.1002/jame.20047.

Tompkins, A. M. (2001a), Organization of Tropical Convection in Low Vertical Wind Shears: The Role of Water Vapor, *J. Atmos. Sci.*, *58*, 529–545, doi:10.1175/1520-0469(2001)058<0529:OOTCIL>2.0.CO;2.

Tompkins, A. M. (2001b), Organization of Tropical Convection in Low Vertical Wind Shears: The Role of Cold Pools, *J. Atmos. Sci.*, *58*, 1650–1672, doi:10.1175/1520-0469(2001)058<1650:OOTCIL>2.0.CO;2.

Tompkins, A. M., and G. C. Craig (1998), Radiative-convective equilibrium in a three-dimensional cloud-ensemble model, *Q. J. R. Meteorol. Soc.*, *124*, 2073–2097, doi:10.1002/qj.49712455013.

Torri, G., Z. Kuang, and Y. Tian (2015), Mechanisms for convection triggering by cold pools, *Geophys. Res. Lett.*, *42*, 1943–1950, doi:10.1002/2015GL063227.

Wallace, J. M., and P. V. Hobbs (2006), *Atmospheric Science : an Introductory Survey*, 2. ed., 504 pp., Academic Press, Cambridge, Massachusetts.

Wallinga, J. (1995), The role of space in plant population dynamics: annual weeds as an example, *Oikos*, *74*, 377–383, doi:10.2307/3545982.

Wielicki, B. A., and R. M. Welch (1986), Cumulus Cloud Properties Derived Using Landsat Satellite Data, *J. Clim. Appl. Meteorol.*, *25*, 261–276, doi:1520-0450(1986)025<0261:CCPDUL>2.0.CO;2.

Wing, A. A., and T. W. Cronin (2016), Self-aggregation of convection in long channel geometry, *Q. J. R. Meteorol. Soc.*, *142*, 1–15, doi:10.1002/qj.2628.

Wing, A. A., and K. A. Emanuel (2014), Physical mechanisms controlling self-aggregation of convection in idealized numerical modeling simulations, *J. Adv. Model. Earth Syst.*, *6*, 59–74, doi:10.1002/2013MS000269.

Wing, A. A., K. Emanuel, C. E. Holloway, and C. Muller (2017), Convective Self-Aggregation in Numerical Simulations: A Review, *Surv. Geophys.*, pp. 1–25, doi:10.1007/s10712-017-9408-4.

Zhao, G., and L. Di Girolamo (2007), Statistics on the macrophysical properties of trade wind cumuli over the tropical western Atlantic, *J. Geophys. Res.*, *112*, D10,204, doi:10.1029/2006JD007371.